Theses and Dissertations

December 2014

Design and Implementation of a Near-field Scanning Optical Module for Inverted Microscopes

Taher Ababneh
University of Wisconsin-Milwaukee

DESIGN AND IMPLEMENTATION OF A NEAR-FIELD SCANNING OPTICAL MODULE FOR INVERTED MICROSCOPES

by

Taher S. Ababneh

A Dissertation Submitted in

Partial Fulfillment of the

Requirements for the Degree of

Doctor of Philosophy

in Chemistry

at

The University of Wisconsin-Milwaukee

December, 2014

ABSTRACT

DESIGN AND IMPLEMENTATION OF A NEAR-FIELD SCANNING OPTICAL MODULE FOR INVERTED MICROSCOPES

by

Taher S. Ababneh

The University of Wisconsin-Milwaukee, 2014
Under the Supervision of Professor Jörg C. Woehl

This dissertation describes the design and implementation of a home-built near-field scanning optical microscope (NSOM) module for inverted microscopes. In this design, the NSOM module is built atop an inverted fluorescence microscope. This is particularly well suited for applications in which the normal imaging modes of the inverted microscope are still required to locate and study the sample before performing NSOM experiments. This module is used as a near-field instrument for nanostructure investigation of various samples including plane-ruled reflection gratings, AFM calibration standards, nanospheres and gold nanoparticles. In addition, we will demonstrate the ability to achieve nanometer-scale surface modification of specific polymer films using this technique.

TABLE OF CONTENTS

LIST OF FIGURES

viii

ACKNOWLEDGMENTS

Chapter 1

Introduction

1.1 Microscopy

The word "microscope" is derived from the Greek words mikrós meaning "small" and skopeîn meaning "to see". In technical terms, a microscope is an instrument used for viewing small objects, generally too small to be seen by the naked eye, by producing a magnified visual image of the specimen. The study, design and manufacture of microscopes and their use in viewing such small objects is referred to as microscopy.

Based on the method of interaction with the specimen to generate the magnified image, microscopes can be divided into three main types: optical, electron and scanning probe microscopes. An optical microscope uses light to interact with the sample, whereas electron microscope (EM), both the transmission electron microscope (TEM) and the scanning electron microscope (SEM), uses an electron beam. A scanning probe microscope (SPM) such as the atomic force microscope (AFM), scanning tunneling microscope (STM) and our technique of interest; the near-field scanning optical microscope (NSOM), utilizes a physical probe that scans the specimen. While STM measures electric current at the probe-sample interface, both AFM and NSOM measure forces caused by the interaction between the probe and sample. What separates NSOM from other scanning probe microscopy techniques, however, is the ability to couple light into

the scanning probe, which is typically a tapered optical fiber. This makes for an intriguing technique since light is a widely used excitation source in many natural systems as well as scientific fields such as absorption spectroscopy, fluorescence spectroscopy and photolithography. The versatility of NSOM emanates from its capability of simultaneous measurements of force (topography) and optical signal (fluorescence), providing direct correlation between surface features and the optical properties of the specimen.

In the present work, the design and fabrication of a home-built NSOM module for conventional microscopes is described. In this design, the NSOM is built atop an inverted fluorescence microscope. This is particularly well suited for applications in which the normal imaging modes of the inverted microscope are still required to locate and study the sample before performing NSOM experiments. This module is used as a near-field instrument for nanostructure investigation of various samples including gratings, AFM calibration grids, nanospheres and gold nanoparticles. We will also demonstrate the ability to achieve nanometer-scale surface modification of specific polymer films using this technique.

This Chapter is organized as follows: Following this short introduction, we review the classical diffraction limit and its consequences, and discuss the basic ideas behind near-field optical microscopy, then review NSOM probes and their fabrication methods. Afterwards, we address the evanescent fields, followed by NSOM modes of operation, and conclude with the shear-force feedback mechanism.

1.2 Diffraction Limit

Since the discovery of microorganisms by Hooke and van Leeuwenhoek in 1675, conventional light microscopes have played a major role in developing biological and physical sciences and contributed to numerous achievements that lead to many advances in life sciences and technology.

The advantages of the optical microscope have led to its success. Some of these benefits are: the ability to image a broad range of samples in a variety of environments; the noninvasive nature as the radiation does not alter the structure of the object; the ability to quickly survey the sample with large field of view; its low cost; convenience and user-friendliness. It is not surprising that optical microscopy is to this day the most common form of microscopy found in laboratories of advanced research institutes as well as general education schools.

The basic makeup of a conventional microscope involves a focusing element such as a convex lens to focus the light. The sample is placed at a relatively large distance from the light source. Hence, the name "far-field" is generally used to describe classical microscopy (Figure 1.1).
Under this standard configuration, the basic rules of light interference and diffraction create a fundamental limitation that restricts the maximum resolution to about half the wavelength of the light. As scientific investigations called for higher resolutions, the boundary imposed by the very physical nature of light, assimilated in the far-field diffraction, pushed the optical microscope to its fundamental limit.

This limitation is usually referred to as the "Abbe barrier", after Ernst Abbe, for his contribution in describing the resolution limit of an optical microscope in 1873[1]. In an optical system, the smallest resolvable spacing Δx is approximated from Abbe's theory as: $\Delta x = \lambda/(2n\sin\theta)$, where λ is the wavelength of light, and n is the refractive index of the imaging medium (with n=1.00 for air and 1.33 for water) and θ is the half-angle of the maximum cone of light subtended by the lens (Figure 1.3a).

a)

F (Focal point)

∞

f
(Focal length)

b)

Object Objective
lens

Magnified   Eye-   Eye
real image   piece

∞
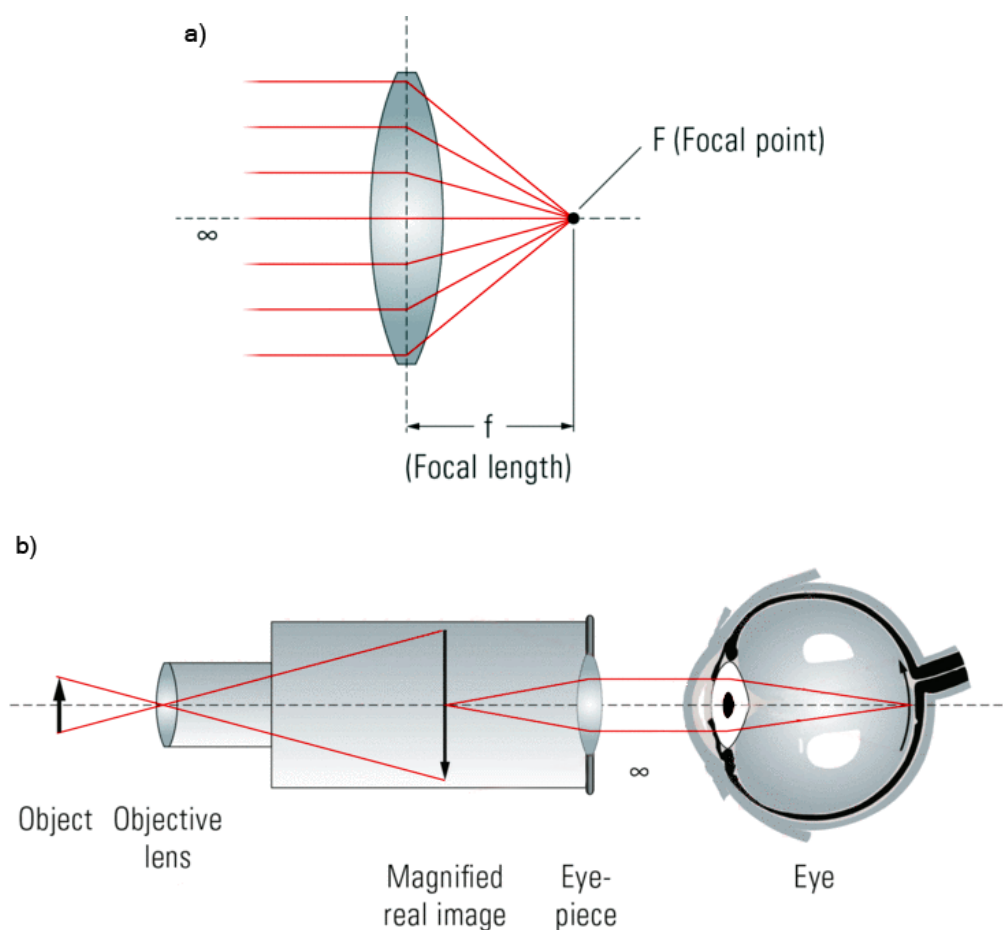
Figure 1.1 - (a) *Optical microscopes use optical elements such as converging lenses to focus the light.*
(b) Schematic diagram of the compound light microscope.

The denominator ($n\sin\theta$) is also known as the numerical aperture (NA) for the objective. It is a dimensionless number that stems from the range of angles over which the system can gather or emit light. Therefore, the resolution can be written as: $\Delta x = \lambda/(2NA)$. With high-quality objective lenses, numerical aperture NA in air can reach 0.95 ($\theta=70°$). Therefore, the Abbe limit can be written as: $\Delta x = \lambda/1.9$. For instance, if the transmitted light is green with wavelength of 500 nm, the maximum obtainable resolution of the microscope is about 263 nm, which is relatively large in comparison to many cellular and engineered nano objects. The limited spatial resolution, which is the main disadvantage of the optical microscope, has pushed the search for a better resolution and consequently led to the concept of near-field scanning optical microscopy, which is considered to be the first successful technique to extend the resolution of optical microscopes beyond the diffraction limit.

1.3 Near-Field Scanning Optical Microscopy (NSOM)

1.3.1 Early Vision and Practical Realization

In a visionary idea, E. H. Synge described in 1928 the modern near field instruments with remarkable accuracy[2]. He suggested the fabrication of an aperture with dimensions much smaller than the optical wavelength in an opaque screen. By illuminating the backside of the opaque screen, the light passing through the aperture provides a confined light source with a volume smaller than the wavelength of the light (Figure 1.2).
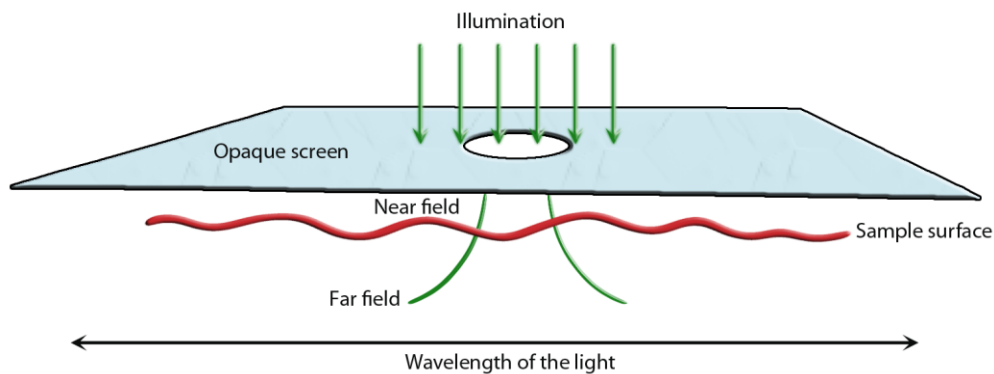
Figure 1.2 - *Schematic representation of the idea of near-field optical microscopy proposed by Synge.*

By placing the screen at a very close proximity from the sample (at a distance much smaller than the wavelength of the light), the light emerging from the aperture is forced to interact with the sample in order to image the specimen before it has time to diffract out and degrade the resolution[3]. This region is the "near-field", hence the name of the technique. By raster scanning this confined source over the specimen's surface, an image with resolution better than the one imposed by the diffraction limit could be obtained. A comparison of diffraction-limited optical microscopy and near-field scanning optical microscopy is schematically represented in Figure (1.3).
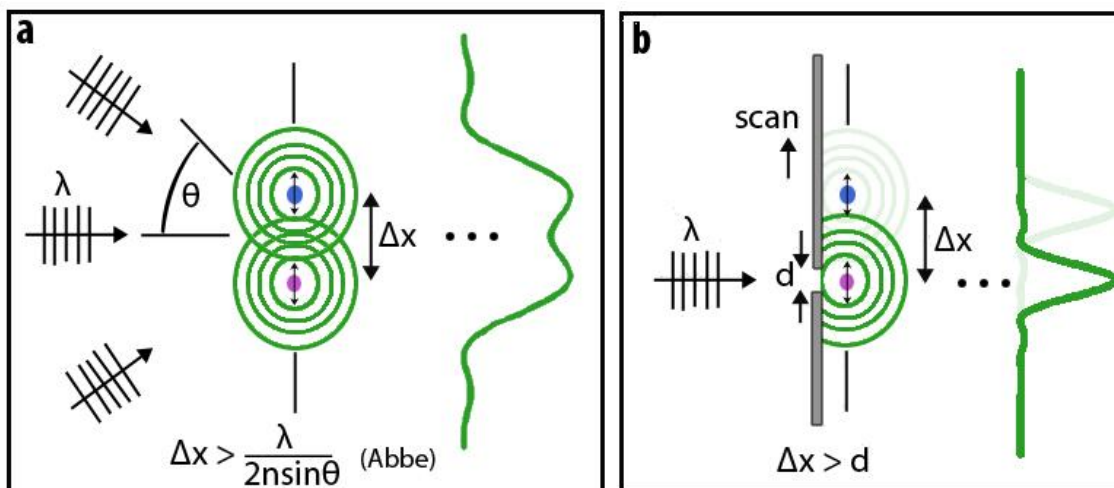
Figure 1.3 *Comparison of diffraction-limited far-field microscopy and near-field optical microscopy.*
(a) Schematic representation of the diffraction limit in optical microscopy showing the minimum resolvable spacing of two light sources.
(b) Schematic representation of aperture near-field scanning optical microscope.

In a follow-up article entitled: "An application of piezo-electricity to microscopy"[4] and published in 1932, Synge addressed the different technical difficulties associated with a practical implementation of his ideas. He also described the use of piezo electric position control for rapidly and accurately scanning the specimen, and proposed the use of an electronic image processing technique. Synge is credited for introducing the principle of scanning in which a source is manipulated in relation to a target in an imaging system[5]. This principle has been employed as an essential element in a wide range of imaging technologies.

After three decades of Synge's 1928 publication, J.A. O'Keefe, a mathematician, presented the same concept of near-field microscopy not knowing about Synge's original idea[6]. He also acknowledged the difficulties associated with a practical implementation and stated the following about his proposal: "The realization of this proposal is rather remote, because of the

difficulty providing for relative motion between the pinhole and the object, when the object must be brought so close to the pinhole"[6].

The first practical developments of near-field optics began with acoustical experiments carried out by Albert V. Baez in 1956 in which acoustic waves with a wavelength of 14 cm were used to demonstrate the principle of near-field imaging by showing that an object (his finger) smaller than the wavelength of sound can be resolved[7].

The microwave experiments performed by Ash and Nicholls in 1972[8] demonstrated the principle of resolution in a scanning near-field microwave microscope using 3 cm radiation and a 1.5 mm sized aperture placed 0.5 mm above an aluminum test sample, and were successful in achieving a resolution better than $\lambda/60$. Their work is considered the first validation of near-field microscopy using electromagnetic radiation.

The first practical realization of Synge's ideas performed using visible radiation was accomplished by Dieter W. Pohl and co-workers at the IBM Research Laboratory in Switzerland in 1984[9], sparking the growth of this new scientific field and leading to the modern day NSOM instrument.

1.3.2 NSOM Probes

Synge's original vision of passing light through a subwavelength aperture milled in an opaque screen does produce a point light source, and can fundamentally be used in a NSOM experiment if the screen is held very close to the sample surface. This arrangement however, can be technically challenging during the scanning process especially if the specimen's surface is relatively rough on the microscopic level, rendering image acquisition process ineffective.

There have been several attempts to fabricate wave guides that can be used as NSOM probes to shine light to a specific region on the sample surface. The first stage in the probe fabrication process has evolved around the formation of a sharply pointed glass tube that can both guide the light and focus it on the sample surface. Early probe designs were developed into pulled micropipets and etched quartz crystals, but these tips generally suffered from low throughput and poor reproducibility[9-12]. Tapered optical fibers offer an excellent choice for making high quality apertures that can serve as the "nano-eye", represented by the nanometric light source confined at the end of a tip. When compared to micropipettes, probes that are based on single-mode optical fibers have more than 1000 times better collection and transmission efficiency. The main advantages of optical fiber probes are low fabrication cost, ease of light coupling into the fiber and delivery into the aperture, and low propagation losses. In addition, polarization and other guiding properties can be controlled in the fiber. Another benefit of using optical fiber tips is that the operating wavelength of the fibers span from the visible to telecom wavelengths, which can be useful for recording spectroscopic information[13]. It is no surprise that the majority of NSOM probes nowadays are created from single-mode optical fibers.

Within this context, it would be appropriate to briefly describe the component layers of a single-mode optical fiber. A typical single-mode optical fiber consists of 3 main layers: the core, cladding and polymer jacket. The core is the center of the fiber where the light travels through and typically has a diameter of 3-8 μm. The cladding, which is the material surrounding the core, has a diameter of 125 μm and is made of glass or plastic substances with an index of

refraction that is lower than that of the core, thus reflecting the light back into the core. The outer polymer jacket on the other hand, is a plastic coating with a main purpose of protecting the fiber from external damage (Figure 1.4).
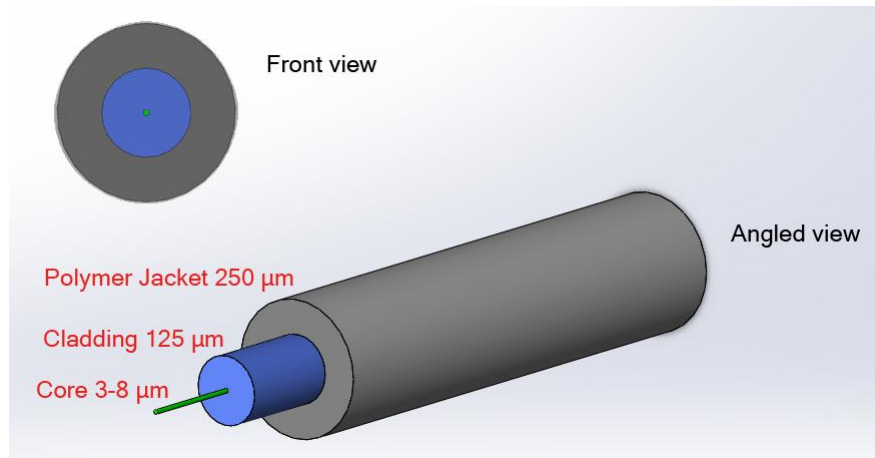
Figure 1.4 – *Typical single-mode optical fiber, showing diameters of the component layers.*

Two methods are commonly used for the fabrication of optical fiber tips: A mechanical pulling technique and chemical etching. A pulled fiber is obtained by combining the use of a CO_2 laser that locally heats and melts the glass at a central point, and a commercial micropipette puller that stretches the fiber at a specific speed. The result is two tapered ends with tip shapes that can vary depending on the temperature, the length of heating and pulling, and the size of the heated area[14,15](Figure 1.5). The first report on the use of thermally pulled fibers for the fabrication of NSOM probes emerged in 1991 marking a significant improvement to the scanning process in NSOM[14].
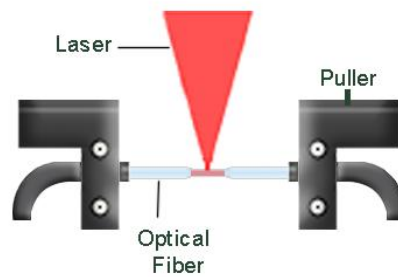
Figure 1.5 - *Schematic representation of the pulling method used to fabricate tapered optical fibers.*

Chemical etching provides an alternative method of taper formation by utilizing a powerful etchant such as hydrofluoric acid (HF), which can react with silicon dioxide, the exclusive ingredient in glass fiber. Initially, the etching process was performed using the meniscus method in which bare fibers (polymer jacket stripped off) are dipped into a 40% HF solution that is covered with a thin layer of an organic solvent or oil[16]. The overlayer is added to help control the taper angle and minimize the corrosive acid vapor. Taper formation is dependent on the meniscus height which lowers as the fiber is etched away. Figure 1.6 shows schematically the progress of the etching process in the meniscus method. The main drawback of this method is its sensitivity to environmental conditions such as temperature and vibrations, causing discontinuous movement of the HF meniscus along the fiber during the etching process and resulting in a rough taper surface.
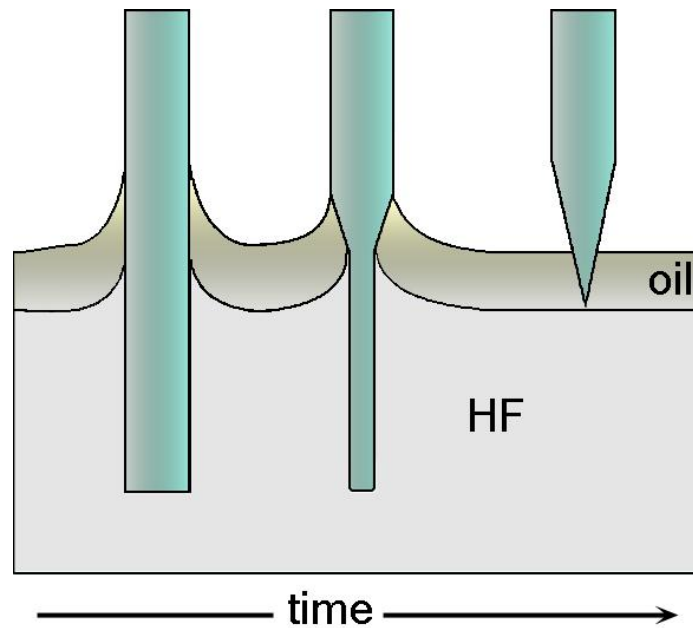
Figure 1.6 – *Schematic representation of the meniscus method used in chemical etching to fabricate tapered optical fibers.*

To overcome these problems, the open tube method was developed in which the polymer jacket is kept intact prior to etching, and consequently the whole etching process takes place inside a hollow cylinder formed by the fiber's protective polymer coating that withstands degradation by HF[17]. By minimizing environmental perturbations, this method yields high quality tips with large cone angles and smooth taper surfaces (Figure 1.7).
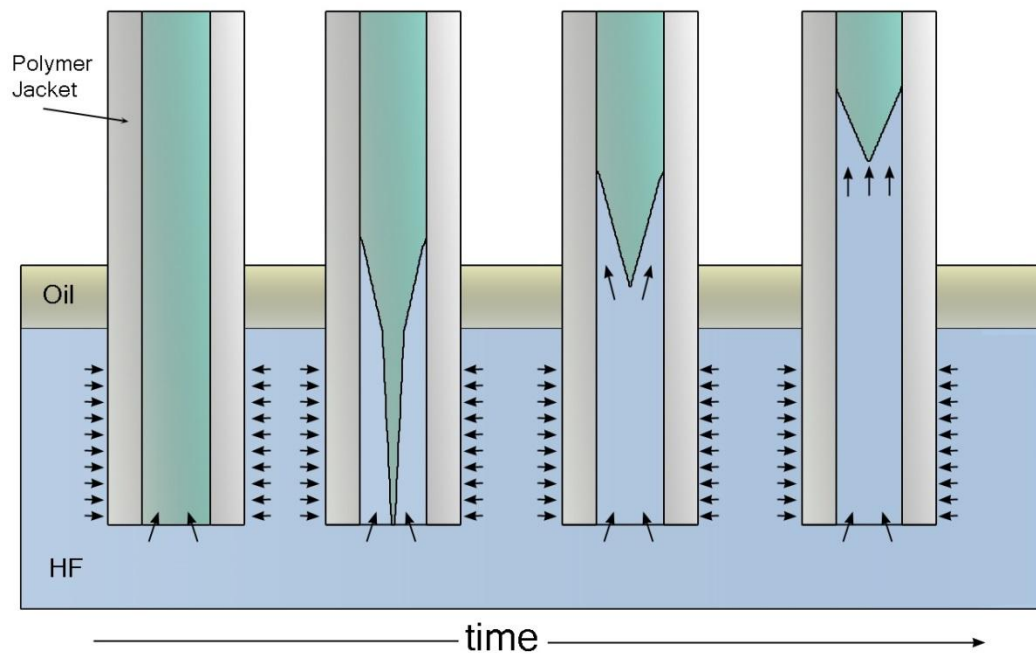
Figure 1.7 - *Schematic representation of the open tube method used in chemical etching to fabricate tapered optical fibers.*

The third etching technique is called the sealed tube method[18] in which a substance, both resistant and impermeable to HF, is used to block the bottom of the fiber during the etching process, restricting diffusion of the etchant to only through the polymer coating. Developing a highly reliable fabrication method has pushed the search for sealant materials that are inert, dense and immiscible with respect to the hydrofluoric acid solution. This has led to implementing a lower "sealing" layer of mercury in the HF solution[18] (Figure 1.8).
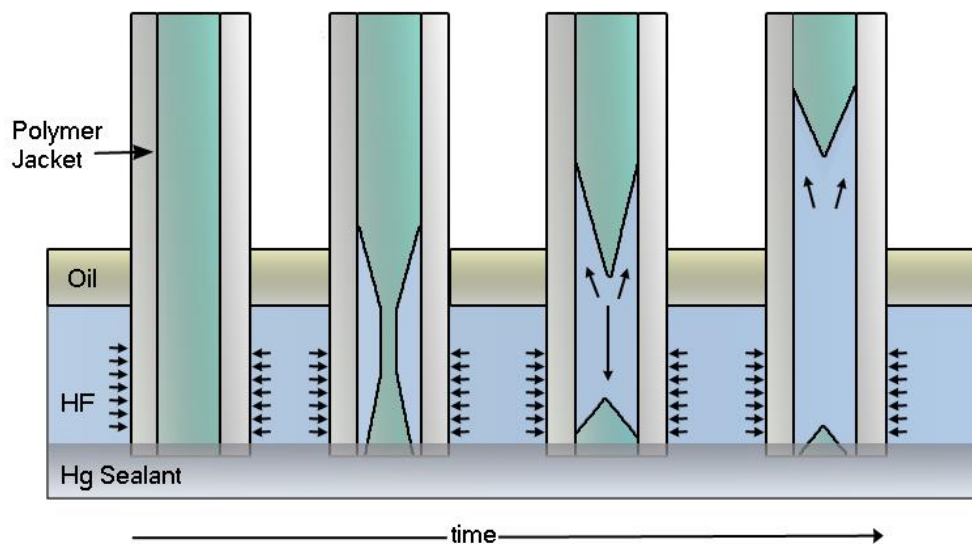
Figure 1.8 - *Schematic representation of the sealed tube method used in chemical etching to fabricate tapered optical fibers.*

This method can efficiently avoid most environmental variables and produce smooth tapered surfaces with great reproducibility. Therefore we are using this technique in the production of all probes used in our imaging experiments. Figure 1.9 shows optical images of chemically etched fiber probes utilizing the three previously discussed methods.
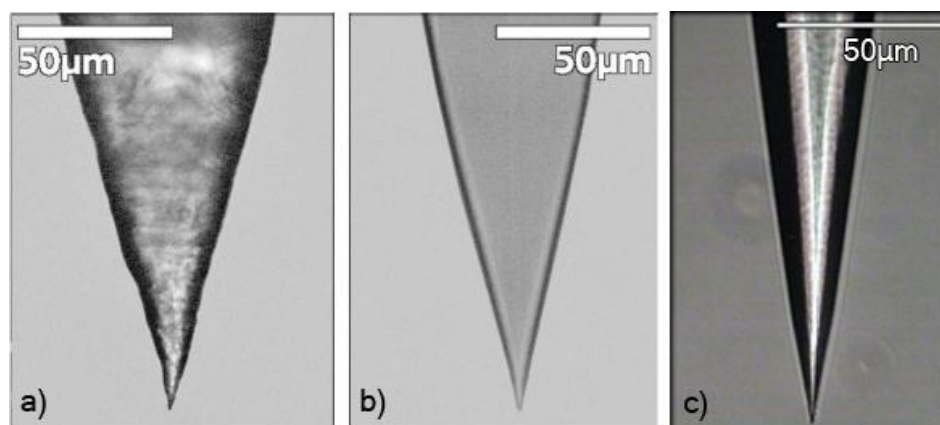
Figure 1.9 - *Optical images of chemically etched fiber probes using a) the meniscus method, b) the open tube method and c) the sealed tube method. a) & b) are from [17], c) a home-fabricated probe.*

In comparison to thermally heated and pulled fibers, chemically etched optical tips have a much shorter taper with larger cone angles, resulting in higher optical efficiency and better mechanical stability (Figure 1.10).
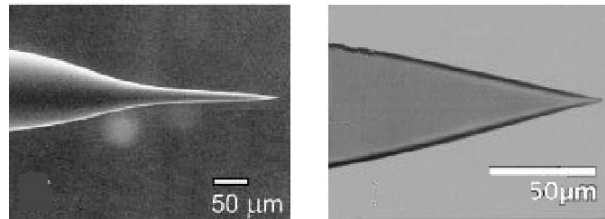
Figure 1.10 - *(Left) Optical probe produced by thermal heating and pulling methods. (Right) Optical probe produced by the chemical etching method*[17].

In addition, the chemical method does not deform the core as in the case with the thermal heating and pulling where the melting process causes undesirable mixing of the core and cladding material, which results in poor light guidance, and in turn lowers the transmission coefficients even further[19]. The thermal heating and pulling method however, has the advantages of being relatively simple, convenient and user-friendly.

Optical fiber tips, regardless of the method of fabrication, undergo considerable light leakage along the tapered side of the fiber. This is primarily due to the reduction in the diameter of the core, which is responsible for light confinement and guiding properties of the fiber. To ensure maximum efficiency of light transmission at the sharpened end of the fiber, tapered optical fibers are placed in a thermal evaporation apparatus and coated with one or more metallic element(s) such as aluminum, silver and gold, to produce a relatively thick metallic coating typically in the order of 100 nanometers. Subsequently, it is

necessary to open up the tip apex so that light can emerge. For that, a focused ion beam (FIB) instrument is used to slice away the very end of tip to create the nano aperture (Figure 1.11).
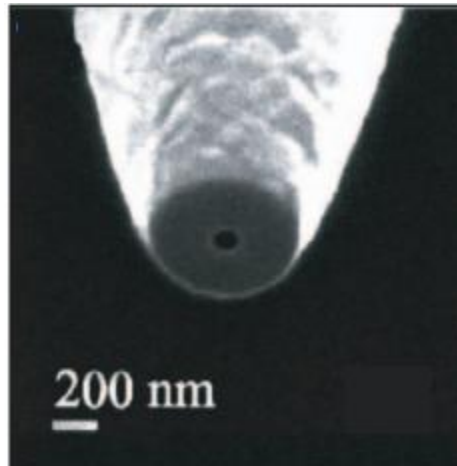
Figure 1.11 *SEM image of smooth aperture probe fabricated by slicing away the very end of a metal coated, tapered optical fiber with a focused ion beam (FIB)* [20].

In a variation to this metallization method, the tapered optical fiber is placed in a thermal evaporator at a predetermined angle and rotated smoothly and continuously, while a metal coating is being evaporated onto the fiber's sidewall. An aperture is formed on the tip apex due to the effect of shadow evaporation, stemmed from the inclination angle of the fiber in relation to the source (Figure 1.12). In contrast to the conventional thermal evaporation of fibers, this method doesn't require the use of focused ion beam (FIB) milling to fabricate the nano aperture.
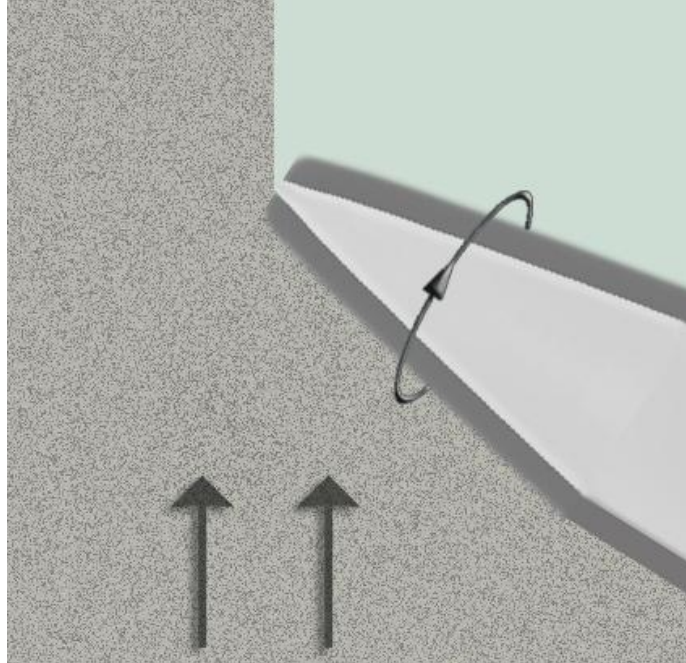
Figure 1.12 *Schematic representation of the shadow evaporation method for the fabrication of nano apertures.*

1.3.3 Evanescent Fields

NSOM takes advantage of the evanescent or non-propagating fields that are created by total internal reflection and exist only near the surface of an object. These optical near-fields allow imaging beyond the diffraction limit because they carry the high spatial frequencies which are associated with fine details of the object. However, the electric field of evanescent waves is exponentially attenuated with increasing distance from the object in the z-direction. Because of this, these fields cannot be detected by the objective of a classical microscope and the detector must be placed very close to the sample in the near field zone of typically a few nanometers. Alternatively, the surface evanescent waves created by the object can be transformed (or frustrated) into propagating radiation by local scatterers (or by interaction with fluorescent molecules) placed in the vicinity

of the surface of the object. Based on Babinet's principle, local scattering is analogous to local illumination. Therefore, the same spatial information and fine details that are available by local scattering can be attained by illuminating the object with evanescent fields created by a local source such as the tip of a pointed optical fiber. The field from the local source is converted by the object into a far-field optical signal that is collected and detected[21](Figure 1.13). It is due to this interchangeable nature of local scattering and local illumination that there are several possible operation modes and systems of NSOM.
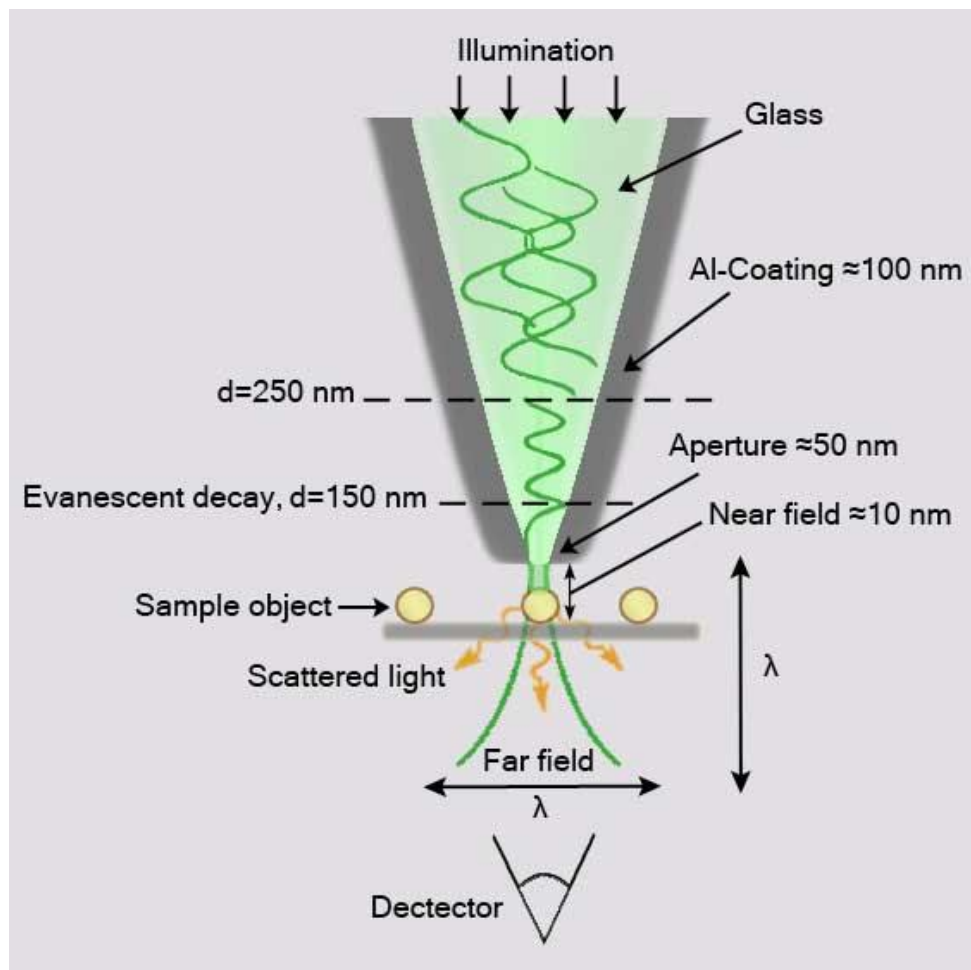
Figure 1.13 - *Schematic representation of a probe of near-field optical microscopy showing the evanescent fields formation at the tip of the probe, the near-field region and the light diffracted out in the far-field (adapted from[22]).*

1.3.4 NSOM Modes of Operation

There are five major configurations that can be employed in an NSOM setup, the choice of which is governed by the optical properties of the sample and experimental conditions. These modes are schematically illustrated in Figure 1.14 and detailed below:

- Illumination: In this configuration, the sample is illuminated through the probe and the light (emitted or transmitted) is collected from underneath the transparent sample typically using the objective lens.

- Collection: The sample is illuminated from the far-field and the probe is used to collect the light from the sample surface.

- Reflection: The sample is illuminated through the probe and the light reflected from the opaque sample surface is collected from the side.

- Reflection collection: The sample is illuminated from the sides and the light is collected by the probe. Reflection modes in general yield less light but allow to study opaque samples

- Illumination collection: The probe in this mode is a shared aperture as it is used to both illuminate and collect the light from the sample. Here, the signal is largely comprised of the background light.
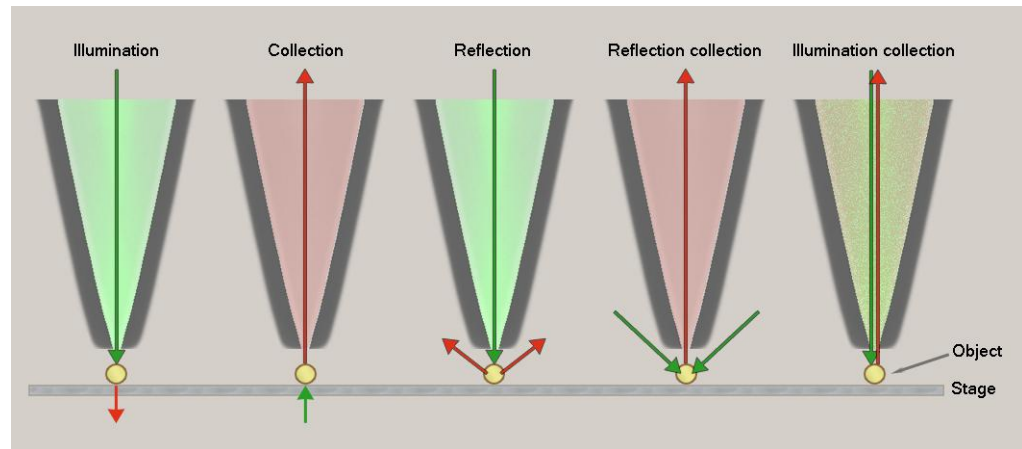
Figure 1.14 *NSOM primary modes of operation.*

The modes that have been discussed heretofore are often referred to as apertured modes of operation since they all utilize a probe that is used to guide the light to or from the sample. In contrary, apertureless modes of operation involve the use of a very sharp uncoated (or metallic) tip to frustrate an evanescent wave produced in a sample by total internal reflection. This generates propagating waves that can be collected by the probe. This method is generally referred to as photon scanning tunneling microscopy (PSTM)[3,23-28]. A comparison of probes used in apertured NSOM mode to apertureless configuration is shown in Figure 1.15.
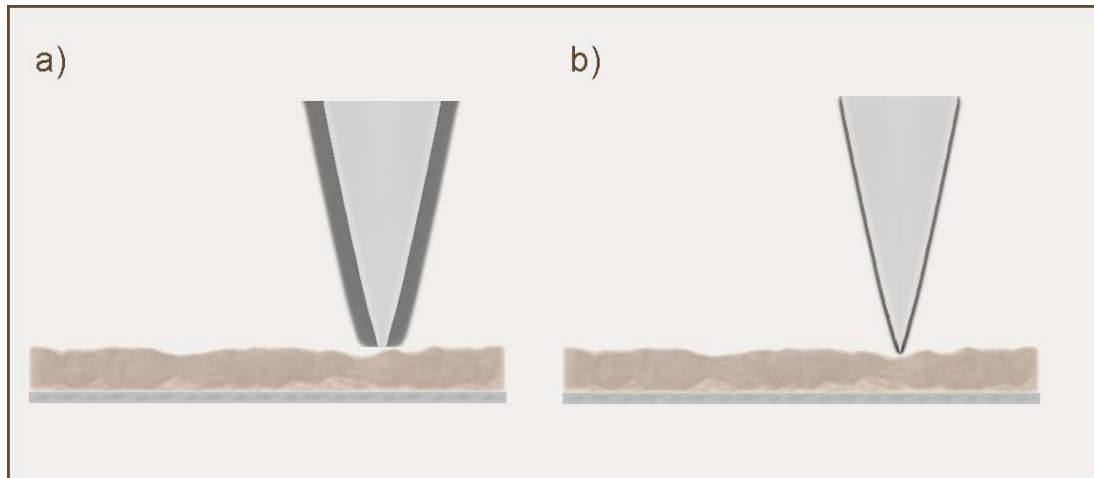
Figure 1.15 *Comparison of probes used in NSOM modes of operations. (a) Typical metal-coated probe used in apertured NSOM. (b) Sharp metallic or transparent tip used in apertureless NSOM mode.*

1.3.5 Feedback Mechanism

It is well known that placing a nanoprobe at a very close proximity from the sample under investigation is a principal requirement for scanning probe microscopy techniques. This had been a notable technical challenge for many years until the early eighties of the last century, when the first use of a physical probe that scans the specimen to form images of the surface emerged with the invention of the scanning tunneling microscope (STM) [29] in 1981, laying the foundation stone of a new field of scanning probe microscopy (SPM).

This significant breakthrough came to practical realization primarily as a result of the development and implementation of piezoelectric-based technology, which directly benefited other SPM techniques subsequently, leading to the introduction of the near-field scanning optical microscope (NSOM) in 1984[9], followed by the atomic force microscope (AFM) in 1986[30].

Tip approach towards the sample surface in SPMs typically utilizes a combination of a *z* piezoelectric scanner for fine approach and a stepper motor for coarse positioning. Once the tip is in the general vicinity of the sample, the coarse positioning system is turned off and the piezoelectric scanner smoothly brings the tip within a few nanometers (or less depending on the SPM technique) from the sample surface. To form images of the surface, a separate *xy* piezoelectric scanner is used to scan the tip over the specimen's surface, or alternatively the tip remains fixed while the sample moves in the *xy* plane.

To obtain high-resolution optical and topographical imaging with NSOM, tip damage must be avoided during the initial approach to the sample surface and the following *xy* scanning. Therefore, the tip must be positioned and held at a constant distance of a few nanometers of the sample surface during scanning. This precise positioning can be accomplished by a means of a shear-force technique, combined with the sensing capability of a crystalline quartz tuning fork employed as a distance detector, and an electronic feedback system controlling the *z* piezoelectric scanner.

The most common feedback mechanism for NSOM is a lateral interaction, in which the tip deflection is parallel to sample surface. Imaging based on this lateral interaction feedback mechanism is commonly referred to as shear force microscopy (SFM). NSOM and non-contact AFM both belong to the family of SFM as they employ similar shear-force feedback modes.
The shear-force technique first surfaced in 1992 when two independent groups almost simultaneously introduced the technique to control the distance between the probe and the sample[31,32]. Shear-force distance control relies on a vibrating

element, onto which the tip is rigidly fixed while extruding out about 1 mm from the vibrating element. During the tip approach, the element is vibrated at resonance while the amplitude of the oscillation is monitored. When in close proximity to the specimen, the mechanical interactions with the surface (shear forces) dampen the vibrations and a reduction in the oscillation amplitude, which strongly depends on the tip-sample separation, is measured. During the early development stage of the shear-force technique, optical feedback detection methods were most common for monitoring the tip vibration amplitude. Typically, a laser spot is tightly focused at the end of the imaging probe, and the reflection is collected by a split photodiode that measures the difference between the signals from each side of the detector; that "difference signal" is proportional to the oscillation amplitude. The main drawback of this technique is the potential addition of stray light into the vicinity of the probe, which could interfere with the near-field optical signal. Moreover, this scheme requires precise alignment of external optics with respect to the imaging probe.

In 1995, Karrai and Grober[33] invented an alternative mechanism to the laser feedback system, in which the shear-force method is combined with the sensing capability of a quartz crystal tuning fork (TF). Quartz is one of the natural materials that exhibit the most piezoelectric characteristics. It was first developed into an oscillator in 1921 by Walter Guyton Cady[34]. The size and shape of the quartz crystal cuts determine the resonance frequency of the crystal[35]. In tuning forks, the crystal is shaped and positioned to oscillate at a common resonance frequency of 32,768 Hz, at which the bending amplitude of the prongs is

maximum. This frequency is also used in electronic circuitry to define clock cycles.

A tuning fork shear force feedback technique uses the basics of piezoelectricity; piezoelectric materials in the form of a tuning fork quartz crystal generate piezoelectric voltage when the fork is mechanically excited by an external source of vibration such as a piezoelectric dither. The output piezoelectric voltage is proportional to the amplitude of oscillation. Based on this idea, a NSOM probe is rigidly attached along one of the prongs of a tuning fork and the fork is mechanically driven to oscillate at its resonance frequency, causing the tip and the fork to vibrate parallel to the sample surface (Figure 1.16). The tuning fork piezoelectric voltage is monitored as the tip approaches the sample surface. When the tip is within some tens of nanometers of the surface, shear-forces start to dampen the tip oscillation and gradually induce a measurable reduction of the tuning fork signal amplitude.
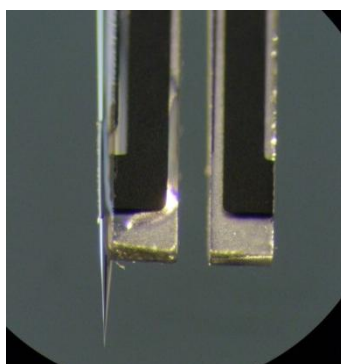
Figure 1.16 *Optical fiber tip rigidly mounted alongside a tuning fork.*

The magnitude of the signal reduction is strongly dependent on the tip-surface separation. The sensitivity of the TF crystal allows for the detection of shear-force interactions as low as 50 pN[33]. Based on a predetermined setpoint, the tip

approach towards the sample surface will stop as soon as the tuning fork signal

matches the setpoint, at which point the tip is held within a few nanometers of the

surface of the sample (Figure 1.17).
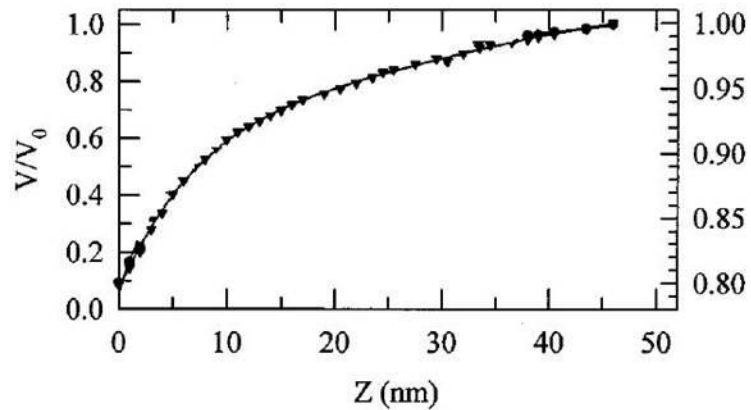
Figure 1.17 *Approach curve of the simultaneous measured piezoelectric signal of the tuning fork as function of the tip-sample distance (adapted from* [33] *).*

To maintain the proper working distance of the probe to the sample during the *xy*

scanning, the damping signal is fed to an electronic feedback system that

maintains constant oscillation amplitude and consequently constant distance

between the tip and the sample topography, directly via the *z* piezoelectric scan

stage. The feedback signal used to keep the tip-sample distance constant is

utilized to generate a topographic map of the sample surface (Figure 1.18).
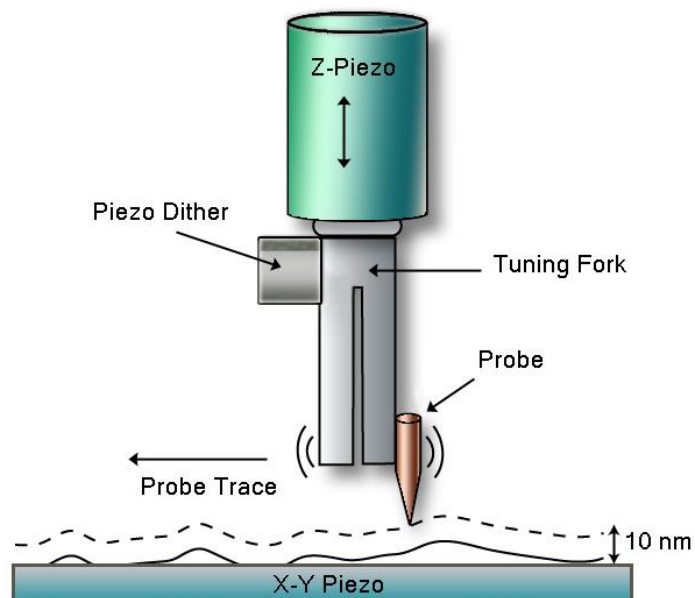
Figure 1.18 *Schematic representations of a tuning fork distance control setup in a shear-force microscope.*

Chapter 2

Theoretical Modeling

2.1 Tuning Fork Distance Control

2.1.1 Simple Harmonic Oscillator

A tuning fork's vibrational motion can be thought of as a spring-mass

system of a simple harmonic oscillator in which a mass is attached to one end of

a spring while the other end is attached to a solid surface (Figure 2.1).
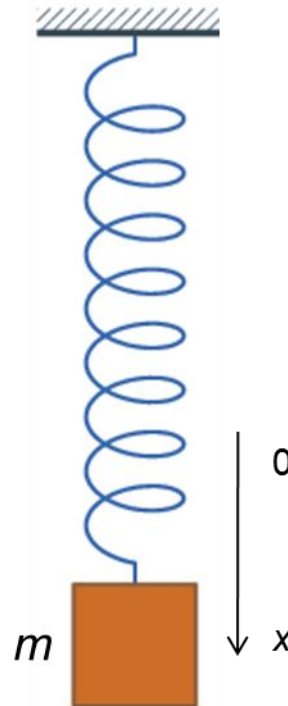
Figure 2.1 "*Mass on a spring" system as an example of simple harmonic motion.*

To obtain the equation of motion of a simple harmonic oscillator, we start with Hook's law in the form

$$\vec{F} = -K\vec{x} \tag{1}$$

This defines the restoring force $\vec{F}$ exerted by a spring on objects attached to its free end and its direct relationship to the spring's displacement $\vec{x}$ from the equilibrium position. K is the spring constant and it is a measure of the spring's stiffness.

According to Newton's second law, the vector sum of the forces $\vec{F}$ on an object is equal to the mass m of that object multiplied by the acceleration vector $\vec{a}$ of the object.

$$\vec{F} = m\vec{a} \tag{2}$$

Assuming there are no other forces acting on the system, we can set Equations 1 and 2 equal to obtain

$$m\vec{a} + K\vec{x} = \vec{0} \tag{3}$$

By using the definitions of velocity $\vec{v}$ and acceleration $\vec{a}$,

$$\vec{v} = \frac{\mathrm{d}\vec{x}}{\mathrm{d}t} \qquad\qquad \vec{a} = \frac{\mathrm{d}\vec{v}}{\mathrm{d}t} = \frac{\mathrm{d}^2\vec{x}}{\mathrm{d}t^2}$$

we can write the equation of motion for a simple harmonic oscillator as

$$m\frac{\mathrm{d}^2\vec{x}}{\mathrm{d}t^2} + K\vec{x} = \vec{0}$$

or expressed In scalar form

$$m\frac{d^2x}{dt^2} + Kx = 0 \tag{4}$$

This is the differential equation for a simple harmonic oscillator that is neither damped nor driven. To solve the equation, we rewrite the equation as

$$\frac{d^2x}{dt^2} = \frac{-K}{m}x$$

We find that the general solution is a linear combination of $\sin(w_o t)$ and $\cos(w_o t)$

$$x(t) = a\sin(w_o t) + b\cos(w_o t)$$

$$\Downarrow$$

$$x(t) = A\sin(w_o t + \emptyset) \tag{5}$$

where the amplitude A and the phase $\emptyset$ are given by

$$A = \sqrt{a^2 + b^2}$$

$$\sin\emptyset = \frac{b}{\sqrt{a^2 + b^2}}$$

$$\cos\emptyset = \frac{a}{\sqrt{a^2 + b^2}}$$

and w_o is the angular frequency or angular speed (in radians per second).

The oscillatory motion is sinusoidal in time and demonstrates a constant amplitude A and a single resonant frequency. Other parameters that are often used to describe oscillatory motion is the time period T, which is the time for a single oscillation, and the frequency f, which is the number of oscillations per unit time ($f = 1/T$). The motion is also characterized by its phase $\emptyset$, which defines

where the wave starts, and its location in space. Figure 2.2 illustrates the displacement against time in a simple harmonic motion.
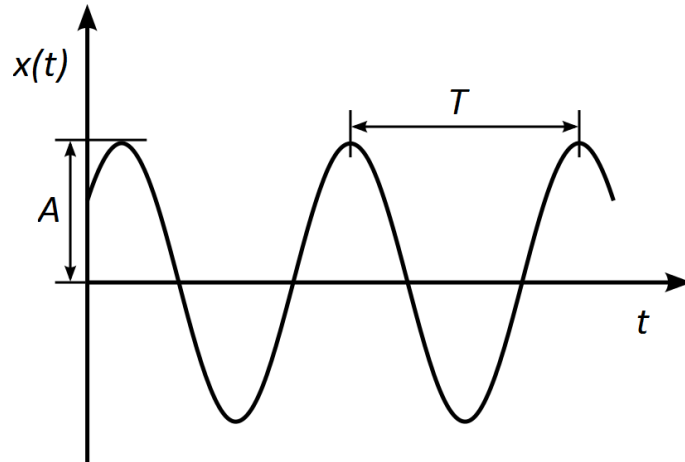
Figure 2.2 *Illustration of the sinusoidal motion of a simple harmonic oscillator showing the main parameters of the wave.*

Now, we determine the first and second derivatives of x with respect to t for Equation 5.

$$\frac{\mathrm{d}x}{\mathrm{d}t} = Aw_o\cos(w_o t + \emptyset) \tag{6}$$

$$\frac{\mathrm{d}^2 x}{\mathrm{d}t^2} = -Aw_o^2 \sin(w_o t + \emptyset) \tag{7}$$

Substituting Equations 5 and 7 into the differential equation for a simple harmonic oscillator (Equation 4), yields

$$-mAw_o^2 \sin(w_o t + \emptyset) + KA \sin(w_o t + \emptyset) = 0$$

Factoring out $A\sin(w_o t + \emptyset)$ leads to

$$(-mw_o^2 + K)\, A \sin(w_o t + \emptyset) = 0$$

The term $(-mw_o^2 + K)$ is set to zero for the left side of the equation to equal zero at any time t.

$$(-mw_o^2 + K) = 0$$

$$w_o^2 = \frac{K}{m}$$

$$w_o = \sqrt{\frac{K}{m}} \tag{8}$$

Therefore, the angular frequency w_o can be determined by specifying the spring constant K and the mass m of the object. In addition, the frequency f and the period T can be calculated from the angular frequency as follows

$$f = \frac{1}{2\pi}\sqrt{\frac{K}{m}}$$

$$T = 2\pi\sqrt{\frac{m}{K}}$$

2.1.2 Damped Harmonic Oscillator

Building upon the simple harmonic oscillator model, and taking into account the frictional force acting on the system and slowing down its motion, a more accurate equation for real oscillators can be obtained.

In damped harmonic motion, we assume that a frictional force $\vec{F}_D$ is directly proportional to the velocity of the object.

$$\vec{F}_{\mathrm{D}} = -\gamma \frac{\mathrm{d}\vec{x}}{\mathrm{d}t} \qquad (9)$$

where γ is called the viscous damping coefficient. The negative sign indicates

that the frictional force is opposite to movement and with time causes the

oscillations to come to a stop. Newton's second law gives us the balance of

forces for damped harmonic oscillator

$$\vec{F} = m\vec{a} = -K\vec{x} + \left(-\gamma \frac{\mathrm{d}\vec{x}}{\mathrm{d}t} \right)$$

As before, we substitute $\vec{a}$ by $\mathrm{d}^2\vec{x}/\mathrm{d}t$ and rearrange the above equation to obtain

$$m\frac{\mathrm{d}^2\vec{x}}{\mathrm{d}t^2} + \gamma \frac{\mathrm{d}\vec{x}}{\mathrm{d}t} + K\vec{x} = \vec{0}$$

Dividing by mass m and expressing in scalar form results in

$$\frac{\mathrm{d}^2 x}{\mathrm{d}t^2} + \frac{\gamma}{m}\frac{\mathrm{d}x}{\mathrm{d}t} + \frac{K}{m}x = 0 \qquad (10)$$

The general solution of Equation 10 can be expressed as

$$x(t) = A\mathrm{e}^{-ct}\sin(wt + \emptyset) \qquad (11)$$

This result indicates that the frequency and time period are constant for a

damped harmonic oscillator, whereas the amplitude undergoes exponential

decay over time (Figure 2.3).

x(t)

T

t
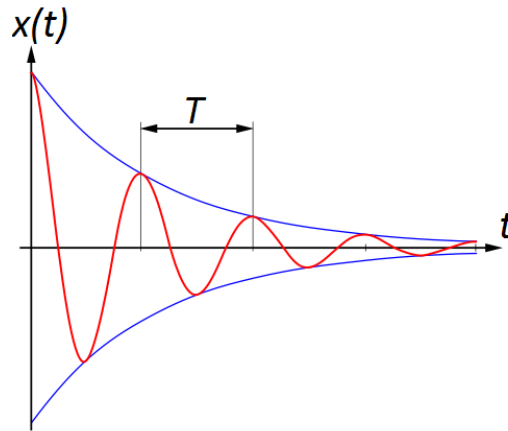
Figure *2.3* *A plot of the sinusoidal motion of a damped harmonic oscillator showing the exponential decay of the amplitude.*

We then carry out first and second order differentiations with respect to time t

$$\frac{dx}{dt} = A[-ce^{-ct}\sin(wt + \emptyset) + we^{-ct}\cos(wt + \emptyset)] \tag{12}$$

$$\frac{d^2x}{dt^2} = A[c^2e^{-ct}\sin(wt + \emptyset) - ce^{-ct}w\cos(wt + \emptyset)$$

$$- wce^{-ct}\cos(wt + \emptyset) - w^2e^{-ct}\sin(wt + \emptyset)]$$

Combining similar terms in the second derivative equation gives

$$\frac{d^2x}{dt^2} = A[(c^2 - w^2)e^{-ct}\sin(wt + \emptyset) - 2wce^{-ct}\cos(wt + \emptyset)] \tag{13}$$

We then substitute Equations 11, 12 and 13 into Equation 10 to get

$$A[(c^2 - w^2)\mathrm{e}^{-ct}\sin(wt + \emptyset) - 2wc\mathrm{e}^{-ct}\cos(wt + \emptyset)]$$

$$+ \frac{\gamma}{m}A[-c\mathrm{e}^{-ct}\sin(wt + \emptyset) + w\mathrm{e}^{-ct}\cos(wt + \emptyset)]$$

$$+ \frac{K}{m}[A\mathrm{e}^{-ct}\sin(wt + \emptyset)] = 0$$

With distributive multiplications we obtain

$$(c^2 - w^2)A\mathrm{e}^{-ct}\sin(wt + \emptyset) - 2wcA\mathrm{e}^{-ct}\cos(wt + \emptyset)$$

$$- \frac{\gamma}{m}cA\mathrm{e}^{-ct}\sin(wt + \emptyset) + \frac{\gamma}{m}wA\mathrm{e}^{-ct}\cos(wt + \emptyset)$$

$$+ \frac{K}{m}A\mathrm{e}^{-ct}\sin(wt + \emptyset) = 0$$

Factoring out the sine and cosine terms yields

$$\left(c^2 - w^2 - \frac{\gamma}{m}c + \frac{K}{m}\right)A\mathrm{e}^{-ct}\sin(wt + \emptyset)$$

$$+ \left(\frac{\gamma}{m}w - 2wc\right)A\mathrm{e}^{-ct}\cos(wt + \emptyset) = 0 \tag{14}$$

Given that $\mathrm{e}^{-ct} > 0$ and the initial amplitude A and angular frequency w of the oscillation must not substantially decline ($A, w \nrightarrow 0$), we can safely set the two bracketed groups to zero. Thus

$$c^2 - w^2 - \frac{\gamma}{m}c + \frac{K}{m} = 0 \tag{15}$$

and

$$\frac{\gamma}{m}w - 2wc = 0 \tag{16}$$

By solving Equation 16 for c, we have

$$\frac{\gamma}{m} - 2c = 0$$

$$c = \frac{\gamma}{2m} \tag{17}$$

where c is called the damping constant. By substituting $\gamma/2m$ for c in Equation 15, we get

$$\frac{\gamma^2}{4m^2} - w^2 - \frac{\gamma^2}{2m^2} + \frac{K}{m} = 0 \tag{18}$$

By solving for w^2 and subsequently for w

$$w^2 = \frac{K}{m} - \frac{\gamma^2}{4m^2}$$

$$w = \sqrt{\frac{K}{m} - \left(\frac{\gamma}{2m}\right)^2} \tag{19}$$

Recall that the natural frequency of simple harmonic oscillator w_o is given by

$$w_o = \sqrt{\frac{K}{m}}$$

Therefore, Equation 19 can be written as

$$w = \sqrt{w_o^2 - c^2} \tag{20}$$

where w here is the damped oscillation frequency, which is clearly lower than the natural frequency w_o for a simple harmonic oscillator. In the case of a tuning fork, friction exists internally due to the bending motion of the prongs. With these

forces taken into account, a common tuning fork in air has a "natural" frequency of 32768 Hz. Operating the tuning fork in a viscous medium introduces external frictional forces that will shift the natural frequency to a lower value. Moreover, the attachment of a probe to one of the tuning fork prongs increases the mass of the system, thus slowing down the oscillations, and consequently shifting the natural frequency lower.

2.1.3 Driven Harmonic Oscillator with Damping

On the basis of the damped harmonic oscillator model, and factoring in the driving force for the oscillator, we can derive a more accurate equation of motion that reflects the oscillation of a tuning fork as a driven oscillator with damping. The driving force in shear-force microscopy (SFM) is typically generated from an electrically driven dither piezoelectric element. A force of this type is oriented along the vibrational displacement x. This allows for lateral deflection of the fork in relation to the sample surface (Figure 2.4).

The driving force acting on the system is a periodic steady-state force that is characterized by its own amplitude F_o and frequency w. The amplitude of a tuning fork vibration is directly proportional to the amplitude of the driving force. For example, if we double the driving force, the tuning fork's vibration will double as well.
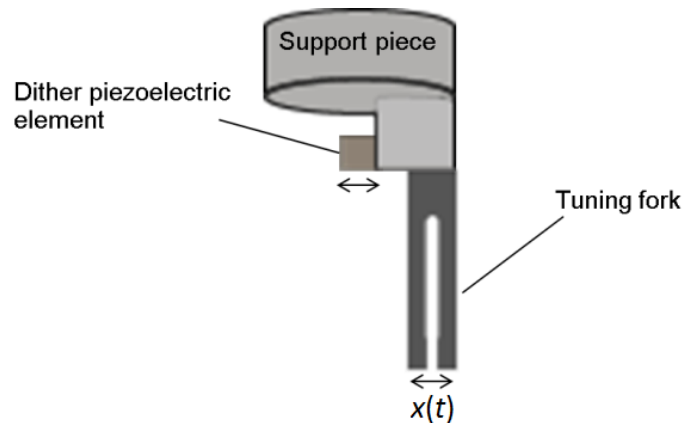
Figure 2.4 *Schematic representation of a tuning fork as a driven oscillator. The dither piezoelectric element is electrically driven to vibrate along the vibrations $x(t)$ of the tuning fork.*

Let's consider the case when we "drive" a tuning fork from rest (at equilibrium) with an applied force oscillating at or near the fork's natural frequency. The initial "disturbance" to the tuning fork results in a transient "pre-steady-state", during which the vibrations gain more momentum and keep on increasing with time until the amplitude quickly grows to a maximum and the fork settles into a "steady-state" motion (Figure 2.5). The driving frequency dictates the frequency of the system. Thus, the frequency of the steady state motion of the tuning fork is equal to the driving frequency, not the natural frequency of the tuning fork. However, for the experiments the frequency of the applied force is tuned to the natural frequency of the tuning fork, so the amplitude of vibrations can get very high. This phenomenon is called resonance, and it follows that the natural frequency of a system is commonly referred to as the resonant frequency. Because the tuning fork displacement (vibration) lags the applied force, the vibration of the steady-state is 90° out of phase with the forcing frequency.
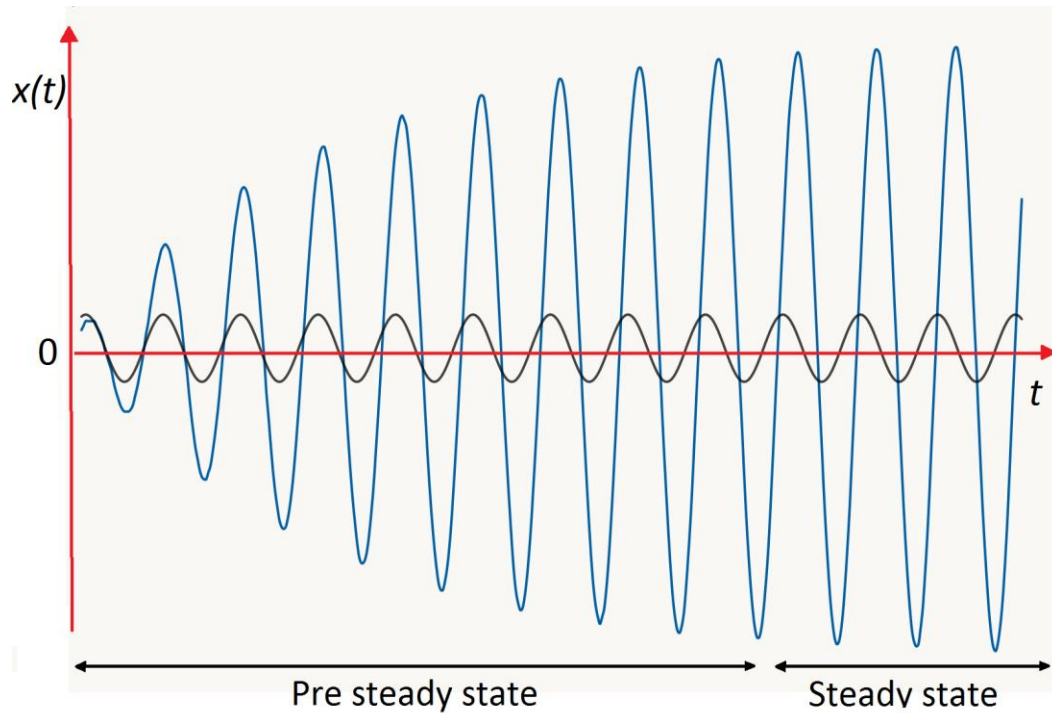
Figure 2.5 *A plot of displacement vs time. The oscillator is being driven at resonance with an applied force. The black curve shows the applied force and the blue curve shows the tuning fork oscillations in response to the applied force.*

The sinusoidal driving force is given by

$$\vec{F}(t) = F_o \sin(wt) \tag{21}$$

where F_o is the amplitude and w is the frequency of the driving force.

Newton's second law gives us the balance of forces for driven harmonic oscillator with damping

$$\vec{F} = m\vec{a} = -K\vec{x} - \gamma \frac{\mathrm{d}x}{\mathrm{d}t} + \vec{F}(t)$$

Rearrangement of this equation gives

$$m\vec{a} + \gamma \frac{\mathrm{d}\vec{x}}{\mathrm{d}t} + K\vec{x} = \vec{F}(t)$$

Substituting $\vec{a}$ by $d^2\vec{x}/dt^2$ and dividing by m yields the following differential

equation in scalar form

$$\frac{d^2x}{dt^2} + \frac{\gamma}{m}\frac{dx}{dt} + \frac{K}{m}x = \frac{F_o}{m}\sin(wt) \tag{22}$$

Having realized the differential equation of motion for a driven harmonic oscillator

with damping, we now look into obtaining the amplitude A and phase shift $\emptyset$.

A general solution for Equation 22 can take this form

$$x(t) = A\sin(wt + \emptyset)$$

Due to phase shift, we have $(wt + \emptyset)$ for the steady-state and (wt) for the pre-

steady-state motion. Hence, we need to split up (wt) from $\emptyset$. This leads to

$$x(t) = A[\sin(wt)\cos\emptyset + \cos(wt)\sin\emptyset] \tag{23}$$

As earlier, we differentiate with respect to time to obtain

$$\frac{dx}{dt} = A[w\cos(wt)\cos\emptyset - w\sin(wt)\sin\emptyset] \tag{24}$$

$$\frac{d^2x}{dt^2} = A[-w^2\sin(wt)\cos\emptyset - w^2\cos(wt)\sin\emptyset] \tag{25}$$

By substituting Equations 23, 24 and 25 into Equation 22 we obtain

$$A[-w^2\sin(wt)\cos\emptyset - w^2\cos(wt)\sin\emptyset]$$

$$+ \frac{\gamma}{m}A[w\cos(wt)\cos\emptyset - w\sin(wt)\sin\emptyset]$$

$$+ \frac{K}{m}A[\sin(wt)\cos\emptyset + \cos(wt)\sin\emptyset] = \frac{F_o}{m}\sin(wt)$$

By distributive multiplications we have

$$-w^2 A\sin(wt)\cos\emptyset - w^2 A\cos(wt)\sin\emptyset + \frac{\gamma}{m} wA\cos(wt)\cos\emptyset$$

$$-\frac{\gamma}{m} wA\sin(wt)\sin\emptyset + \frac{K}{m} A\sin(wt)\cos\emptyset$$

$$+\frac{K}{m} A\cos(wt)\sin\emptyset = \frac{F_o}{m} \sin(wt)$$

Factoring out the sine and cosine terms results in

$$A\sin(wt)\left(-w^2\cos\emptyset - \frac{\gamma}{m} w\sin\emptyset + \frac{K}{m}\cos\emptyset\right)$$

$$+ A\cos(wt)\left(-w^2\sin\emptyset + \frac{\gamma}{m} w\cos\emptyset + \frac{K}{m}\sin\emptyset\right)$$

$$= \frac{F_o}{m} \sin(wt)$$

These equations must be valid at any given time, such as $t = \pi/2w$ and $t = 0$.

This results in the following two equations

$$A\left(-w^2\cos\emptyset - \frac{\gamma}{m} w\sin\emptyset + \frac{K}{m}\cos\emptyset\right) = \frac{F_o}{m} \tag{26}$$

and

$$-w^2\sin\emptyset + \frac{\gamma}{m} w\cos\emptyset + \frac{K}{m}\sin\emptyset = 0$$

Factoring out $\sin\emptyset$ in the above equation gives

$$\left(\frac{K}{m} - w^2\right)\sin\emptyset + \frac{\gamma}{m} w\cos\emptyset = 0 \tag{27}$$

Recall that the square of natural frequency of the system w_o^2 is given by

$$\frac{K}{m} = w_o^2$$

also the damping constant c is

$$c = \frac{\gamma}{2m} \Rightarrow \frac{\gamma}{m} = 2c$$

By substituting these two derivations into Equation 27 we get

$$(w_o^2 - w^2)\sin\emptyset + 2cw\cos\emptyset = 0$$

Followed by rearrangement, we obtain

$$(w_o^2 - w^2)\sin\emptyset = -2cw\cos\emptyset \tag{28}$$

$$\Downarrow$$

$$\frac{\sin\emptyset}{\cos\emptyset} = \frac{-2cw}{w_o^2 - w^2}$$

$$\Downarrow$$

$$\tan\emptyset = \frac{-2cw}{w_o^2 - w^2} \tag{29}$$

Equation 29 defines the phase shift between the driving force and the tuning fork after reaching the steady state, at which the displacement lags behind the applied force by an angle $\emptyset$.

We are going to square Equation 28 for subsequent use.

$$(w_o^2 - w^2)^2\sin^2\emptyset = 4c^2w^2\cos^2\emptyset \tag{30}$$

To find the amplitude A, we recall Equation 26

$$A\left(-w^2\cos\emptyset - \frac{\gamma}{m}w\sin\emptyset + \frac{K}{m}\cos\emptyset\right) = \frac{F_o}{m} \tag{26}$$

By distributive multiplication of A

$$A\frac{K}{m}\cos\emptyset - Aw^2\cos\emptyset - A\frac{\gamma}{m}w\sin\emptyset = \frac{F_o}{m}$$

Collecting equal terms of $A\cos\emptyset$ yields

$$\left(\frac{K}{m} - w^2\right)A\cos\emptyset - A\frac{\gamma}{m}w\sin\emptyset = \frac{F_o}{m}$$

As before, we substitute the frequency and damping constant to get

$$(w_o^2 - w^2)\cos\emptyset - 2cw\sin\emptyset = \frac{F_o}{Am}$$

We square both sides of the equation

$$(w_o^2 - w^2)^2\cos^2\emptyset - 2(w_o^2 - w^2)\cos\emptyset\, 2cw\sin\emptyset + 4c^2w^2\sin^2\emptyset = \frac{F_o^2}{A^2m^2} \quad (31)$$

Now we use Equation 28 to replace the shaded terms in Equation 31. We also use $\sin^2\emptyset + \cos^2\emptyset = 1$. This results in

$$(w_o^2 - w^2)^2\cos^2\emptyset + 2(w_o^2 - w^2)^2\sin^2\emptyset + 4c^2w^2(1 - \cos^2\emptyset) = \frac{F_o^2}{A^2m^2}$$

$$\Downarrow$$

$$(w_o^2 - w^2)^2\cos^2\emptyset + 2(w_o^2 - w^2)^2\sin^2\emptyset + 4c^2w^2 - 4c^2w^2\cos^2\emptyset = \frac{F_o^2}{A^2m^2}$$

Substituting $4c^2w^2\cos^2\emptyset$ by the equivalent term from Equation 30 yields

$$(w_o^2 - w^2)^2\cos^2\emptyset + 2(w_o^2 - w^2)^2\sin^2\emptyset + 4c^2w^2 - (w_o^2 - w^2)^2\sin^2\emptyset$$

$$= \frac{F_o^2}{A^2m^2}$$

Combining equal terms gives

$$(w_o^2 - w^2)^2 + 4c^2w^2 = \frac{F_o^2}{A^2m^2}$$

By solving for A^2, we obtain

$$A^2 = \frac{F_o^2/m^2}{[(w_o^2 - w^2)^2 + 4c^2w^2]}$$

$$\Downarrow$$

$$A = \frac{F_o/m}{\sqrt{(w_o^2 - w^2)^2 + 4c^2w^2}} \tag{32}$$

This defines the amplitude of tuning fork oscillations after reaching the steady state of damped motion (note that the amplitude is time-independent and does not decay to zero under these conditions). As discussed earlier, the amplitude A depends on the driving frequency w and is directly proportional to the driving force F_o . Due to the phenomena of resonance, the greatest amplitude occurs at or around $w = w_o$ (when the driving frequency equals the natural frequency). Additionally, assuming no damping $(c = 0)$ at resonance, the denominator in Equation 32 will approach zero, which means that the motion will theoretically continue to grow on into infinity. Fortunately, the amplitude remains finite even with the smallest amount of damping.

Typically, the heavier the damping, the more the resonance peaks will be decreased, broadened and shifted to left (lower frequency). The resonant response of a driven damped oscillator under four levels of damping is shown in Figure 2.6. Similarly, as the tuning fork with attached tip approaches a sample surface, dampening causes the oscillation amplitude to decrease and the resonant frequency to shift to a lower value.

The phase shift between the driving force and the tuning fork also depends on the frequency. A plot of the phase of the system with respect to the driving frequency is shown in Figure 2.7. We can see that the phase is close to zero at low forcing frequencies so the system oscillates in phase with the driving force, but quickly changes to a $-\pi/2$ phase shift at resonance, as the displacement lags the driving force.
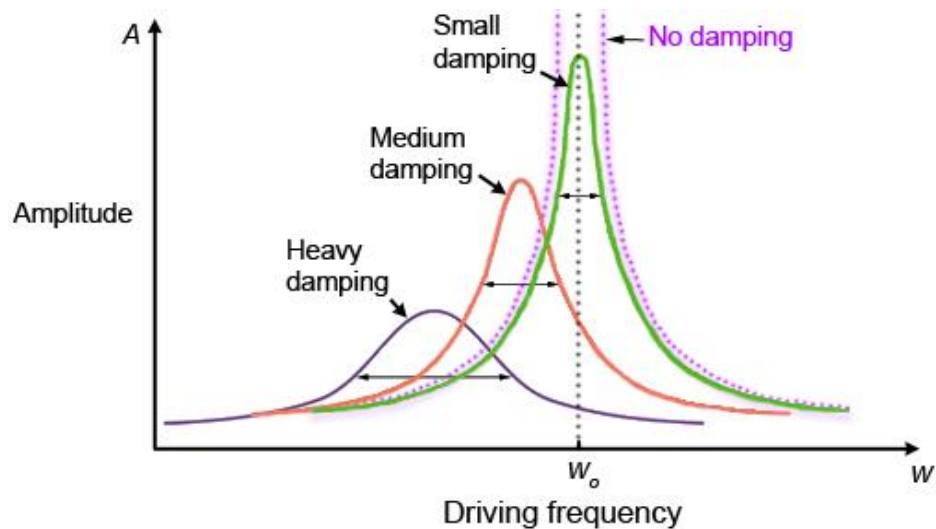
Figure 2.6 *The steady-state amplitude of a damped oscillator as a function of the frequency of the driving force. The effect of damping on the resonant frequency is shown. The colored curves represent the resonant response of the oscillator under four levels of damping (no damping, small, medium and heavy damping).*
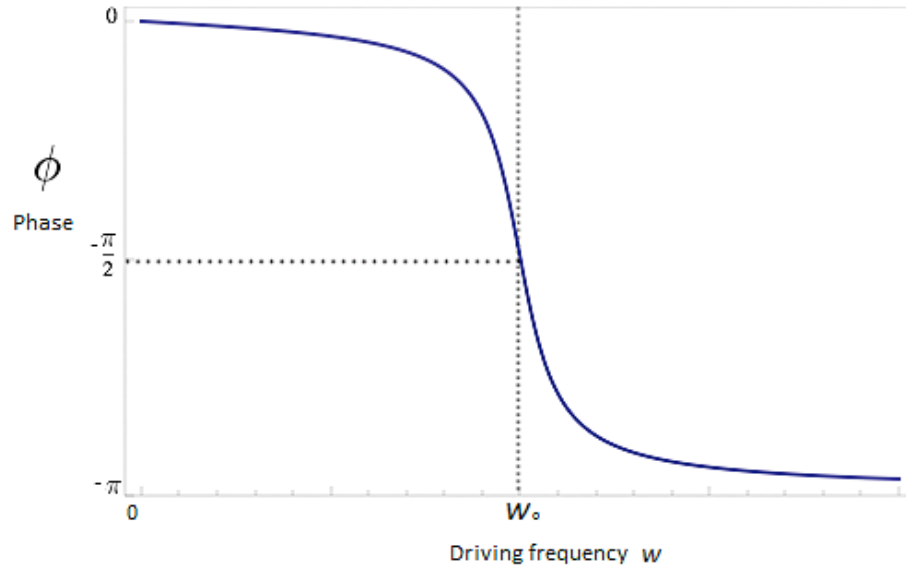
Figure 2.7 *Phase of the steady-state motion as a function of the driving frequency.*

We now shift gears into the evaluation of the maximum amplitude A_{res} of the resonance peak and the frequency at A_{res}. Also, we will look into the full width at half maximum (FWHM) of resonance peaks.

Figure 2.8 shows important parameters of a resonance curve including the full width at half maximum (FWHM), the peak amplitude A_{res} and the resonance frequency W_{res}.

According to the amplitude equation of the steady state

$$A = \frac{F_o}{m\sqrt{(w_o^2 - w^2)^2 + 4c^2 w^2}} \qquad (32)$$

$A(w)$ as a function of w becomes zero for $w \rightarrow \infty$ and shows another minimum at the other end when $w = 0$ (then $A(0) = F_o/mw_o^2$). In between these limits the amplitude peaks at some value of w. To determine this maximum we first solve $\mathrm{d}A/\mathrm{d}w = 0$ for w
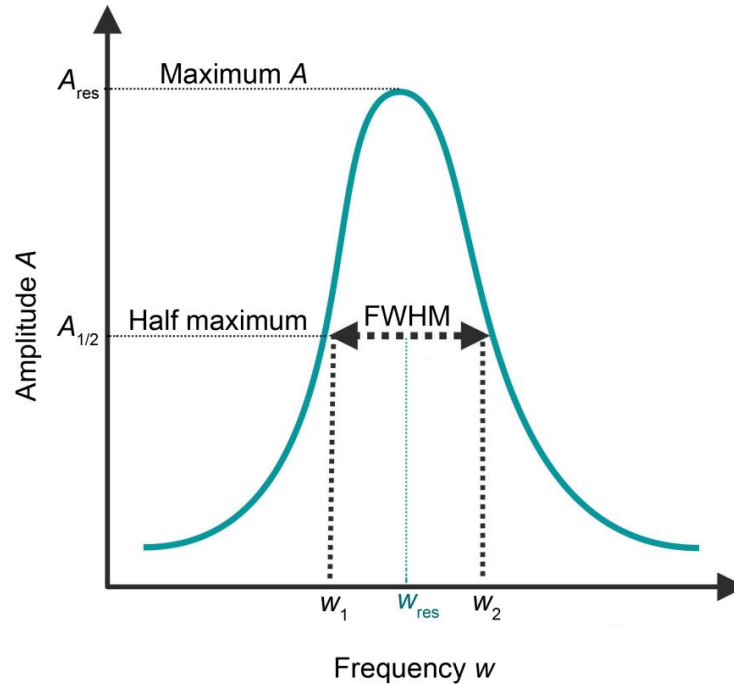
Figure 2.8 *Typical example of a resonance curve showing important characteristics such as full width at half maximum (FWHM), the peak amplitude A_{res} and the resonance frequency W_{res}.*

$$\frac{\mathrm{d}A}{\mathrm{d}w} = \frac{F_o w[4c^2 + 2(w^2 - w_o^2)]}{m[(w^2 - w_o^2)^2 + (2cw)^2]^{3/2}} = 0$$

which leads to

$$F_o w[4c^2 + 2(w^2 - w_o^2)] = 0$$

Setting the bracketed terms to zero will result in one relevant solution

$$w = w_{\text{res}} = \sqrt{w_o^2 - 2c^2} \tag{33}$$

This confirms that the resonance frequency is not found at w_o but rather at a lower frequency due to damping. Since w here represents the resonance frequency, it is referred to as w_{res}. Next we substitute w_{res} into Equation 32 to obtain the peak amplitude A_{res}

$$A_{\text{res}} = \frac{F_o}{m\sqrt{(w_o^2 - [w_o^2 - 2c^2])^2 + 4c^2(w_o^2 - 2c^2)}}$$

$$\Downarrow$$

$$A_{\text{res}} = \frac{F_o}{m\sqrt{4c^4 + 4c^2 w_o^2 - 8c^4}}$$

$$\Downarrow$$

$$A_{\text{res}} = \frac{F_o}{m\sqrt{4c^2 w_o^2 - 4c^4}}$$

$$\Downarrow$$

$$A_{\text{res}} = \frac{F_o}{m\sqrt{4c^2(w_o^2 - c^2)}}$$

$$\Downarrow$$

$$A_{\text{res}} = \frac{F_o}{2mc\sqrt{w_o^2 - c^2}} \tag{34}$$

What is the full width at half maximum FWHM?

We now write an equation that defines half of the peak amplitude

$$A_{1/2} = \frac{A_{\text{res}}}{2} = \frac{F_o}{4mc\sqrt{w_o^2 - c^2}}$$

Then we set the following condition

$$A = A_{1/2}$$

$$\Downarrow$$

$$\frac{F_o}{m\sqrt{(w_o^2 - w^2)^2 + (2cw)^2}} = \frac{F_o}{4mc\sqrt{w_o^2 - c^2}}$$

$$\Downarrow$$

$$m\sqrt{(w_o^2 - w^2)^2 + (2cw)^2} = 4mc\sqrt{w_o^2 - c^2}$$

$$\Downarrow$$

$$(w_o^2 - w^2)^2 + (2cw)^2 = 16c^2(w_o^2 - c^2)$$

$$\Downarrow$$

$$w_o^4 - 2w_o^2 w^2 + w^4 + 4c^2 w^2 - 16c^2 w_0^2 + 16c^4 = 0$$

$$\Downarrow$$

$$w^4 + (4c^2 - 2w_o^2)w^2 + (w_o^4 - 16c^2 w_0^2 + 16c^4) = 0$$

This is a quadratic equation in w^2. Solving the equation follows

$$w^2 = \frac{(2w_o^2 - 4c^2) \pm \sqrt{(4c^2 - 2w_o^2)^2 - 4(w_o^4 - 16c^2 w_0^2 + 16c^4)}}{2}$$

$$\Downarrow$$

$$w^2 = (w_o^2 - 2c^2) \pm \frac{1}{2}\sqrt{(4c^2 - 2w_o^2)^2 - 4(w_o^4 - 16c^2 w_0^2 + 16c^4)}$$

$$\Downarrow$$

$$w^2 = {w_{res}}^2 \pm \frac{1}{2}\sqrt{(16c^4 - 16c^2w_o^2 + 4w_o^4) - 4w_0^4 + 64c^2w_o^2 - 64c^4}$$

$$\Downarrow$$

$$w^2 = {w_{res}}^2 \pm \frac{1}{2}\sqrt{48c^2w_o^2 - 48c^4}$$

$$\Downarrow$$

$$w^2 = {w_{res}}^2 \pm \frac{1}{2}\sqrt{48c^2(w_o^2 - c^2)}$$

$$\Downarrow$$

$$w^2 = {w_{res}}^2 \pm \frac{1}{2}\sqrt{(4c)^2 3(w_o^2 - c^2)}$$

$$\Downarrow$$

$$\qquad\qquad {w_{1/2}}^2 = {w_{res}}^2 \pm 2c\sqrt{3(w_o^2 - c^2)} \qquad\qquad (35)$$

We refer to the frequency at this point as $w_{1/2}$ since it represents the two

frequencies at half of the amplitude. For simplicity, we will substitute the term

$2c\sqrt{[3(w_o^2 - c^2)]}$ by Δw^2. Therefore Equation 35 becomes

$$ {w_{1/2}}^2 = {w_{res}}^2 \pm \Delta w^2 $$

Thus, the two solutions (limits) are given by

$$\qquad\qquad {w_1}^2 = {w_{res}}^2 - \Delta w^2 \qquad\qquad (36)$$

and

$$w_2{}^2 = w_{\text{res}}{}^2 + \Delta w^2 \tag{37}$$

To determine the FWHM, we need to obtain $(w_2 - w_1)$. We will start by

subtracting Equation 36 from 37

$$w_2{}^2 - w_1{}^2 = w_{\text{res}}{}^2 + \Delta w^2 - (w_{\text{res}}{}^2 - \Delta w^2)$$

$$\Downarrow$$

$$w_2{}^2 - w_1{}^2 = 2\Delta w^2$$

For simplification we write

$$w_2{}^2 - w_1{}^2 = (w_2 - w_1)(w_2 + w_1) = 2\Delta w^2 \tag{38}$$

If the resonance peak is very sharp ($c \ll w_o$), w_2 and w_1 become very

comparable so that we can assume

$$(w_2 + w_1) = 2w_{\text{res}}$$

By substituting this into Equation 38 we get

$$2\Delta w^2 = (w_2 - w_1)\, 2w_{\text{res}}$$

Solving for $(w_2 - w_1)$ followed by replacing w_{res} by its equivalence from Equation

33 and expressing Δw^2 as $2c\sqrt{3(w_o^2 - c^2)}$ results in

$$(w_2 - w_1) = \frac{2\Delta w^2}{2w_{\text{res}}} = \frac{2c\sqrt{3(w_o^2 - c^2)}}{\sqrt{w_o^2 - 2c^2}}$$

Based on our condition ($c \ll w_o$), the above equation can be reduced to

$$\text{FWHM} = (w_2 - w_1) = 2c\sqrt{3} \tag{39}$$

A more general equation for evaluating FWHM can be obtained as follows

$$(w_2 - w_1)^2 = w_2^2 + w_1^2 - 2w_1 w_2$$

Substituting w_1^2 and w_2^2 from Equations 36 and 37 yields

$$(w_2 - w_1)^2 = w_{res}^{\,2} + \Delta w^2 + w_{res}^{\,2} - \Delta w^2 - 2w_1 w_2$$

$$\Downarrow$$

$$(w_2 - w_1)^2 = 2w_{res}^{\,2} - 2w_1 w_2$$

$$\Downarrow$$

$$(w_2 - w_1)^2 = 2(w_{res}^{\,2} - w_1 w_2)$$

$$\Downarrow$$

$$w_2 - w_1 = \sqrt{2(w_{res}^{\,2} - w_1 w_2)} \qquad (40)$$

Now, we need to solve for $w_1 w_2$

$$(w_1 w_2)^2 = w_1^2 w_2^2 = (w_{res}^{\,2} - \Delta w^2)(w_{res}^{\,2} + \Delta w^2) = w_{res}^{\,4} - (\Delta w^2)^2$$

$$\Downarrow$$

$$w_1 w_2 = \sqrt{w_{res}^{\,4} - (\Delta w^2)^2}$$

Substituting this result in Equation 40 yields

$$w_2 - w_1 = \sqrt{2[w_{res}^{\,2} - \sqrt{w_{res}^{\,4} - (\Delta w^2)^2}\,]}$$

By substituting $2c\sqrt{3(w_o^2 - c^2)}$ for Δw^2 we obtain

$$w_2 - w_1 = \sqrt{2[w_{\text{res}}{}^2 - (w_{\text{res}}{}^4 - 12c^2w_o^2 + 12c^4)^{1/2}]} \tag{41}$$

This is a general equation for determining the FWHM. To verify the derivation, we apply the same earlier condition of very low damping $(c \ll w_o)$.

Under this condition, the term $12c^4$ in Equation 41 becomes negligible.

Also $w_{res} = w_o$. Therefore we get

$$w_2 - w_1 = \sqrt{2[w_o{}^2 - (w_o{}^4 - 12c^2w_o^2)^{1/2}]}$$

Similarly, we can assume the following

$$w_o{}^4 - 12c^2w_o^2 \approx (w_o^2 - 6c^2)^2$$

Thus

$$w_2 - w_1 = \sqrt{2[w_o{}^2 - w_o^2 + 6c^2]}$$

$$\Downarrow$$

$$\text{FWHM} = w_2 - w_1 \approx \sqrt{12c^2} = 2\sqrt{3}c$$

This is a confirmation to the same result obtained in Equation 39.

We now apply the same condition to the amplitude function. Recall Equation 32

$$A = \frac{F_o}{m\sqrt{(w_o^2 - w^2)^2 + (2cw)^2}} \tag{32}$$

At very low damping $(c \ll w_o)$, we obtain a very sharp resonance peak under which all the values of w that display a non-zero amplitude are very close to w_o $(w \approx w_o)$. Thus, the square root term in the denominator can be reduced as following

$$w_o^2 - w^2 = (w_o - w)(w_o + w) \approx (w_o - w)2w_o$$

Also

$$2cw \approx 2cw_o$$

Substituting into Equation 32 leads to

$$A \approx \frac{F_o}{m\sqrt{4w_o^2(w_o - w)^2 + 4c^2w_o^2}}$$

$$\Downarrow$$

$$A \approx \frac{F_o}{2mw_o\sqrt{(w_o - w)^2 + c^2}} \tag{42}$$

Squaring both sides results in a Lorentzian function

$$A^2 = \left(\frac{F_o^2}{4m^2w_o^2}\right)\left(\frac{1}{(w_o - w)^2 + c^2}\right) \tag{43}$$

Constant   Lorentzian

A Lorentzian function is defined as

$$L(x) = \frac{1}{\pi}\frac{\frac{1}{2}\Gamma}{(x - x_o)^2 + (\frac{1}{2}\Gamma)^2} \tag{44}$$

where:

- x_o - center of peak

- $\frac{1}{2}\Gamma$ - half-width at half maximum (HWHM)

By comparison, we conclude that c in Equation 43 is equivalent to the HWHM ($\frac{1}{2}\Gamma$) in Equation 44. Thus the FWHM for the A^2 function is $2c$, whereas for the A function, the FWHM equals $2c\sqrt{3}$.

Figure 2.9 illustrates the typical form of a Lorentzian distribution.
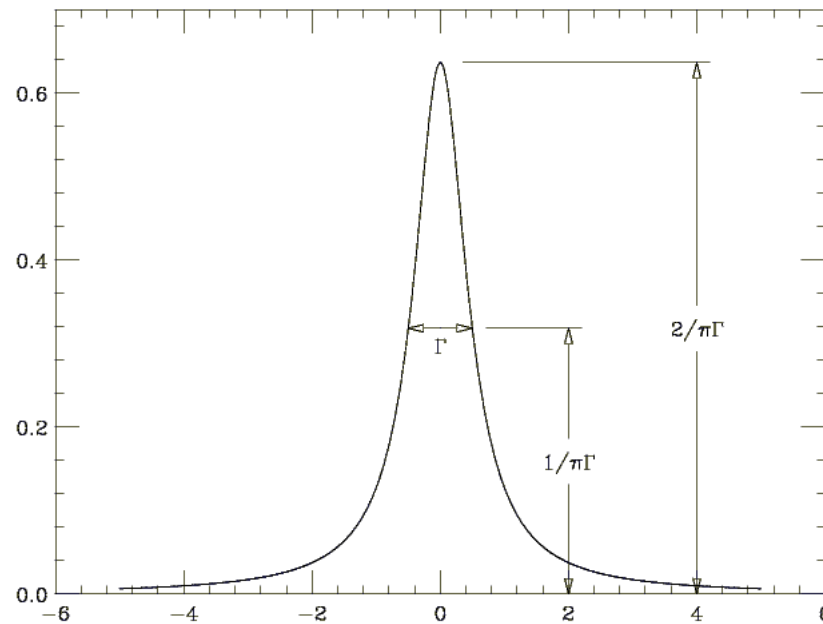
Figure 2.9 *Typical Lorentzian distribution showing important parameters such as the FWHM and the peak height.*

Having the A^2 function matching well with a Lorentzian model indicates that it is related to intensity or energy. To validate this statement, we recall the solution of motion as a function of time

$$x(t) = A\sin(wt + \emptyset)$$

By differentiating with respect to time, we obtain the velocity

$$v = \frac{\mathrm{d}x}{\mathrm{d}t} = wA\cos(wt + \emptyset)$$

Substituting the velocity into the kinetic energy E_K equation gives

$$E_k = \frac{1}{2}mv^2 = \frac{1}{2}mw^2A^2\cos^2(wt + \emptyset)$$

The potential energy is given by

$$E_p = \frac{1}{2}Kx^2$$

Substituting the solution $x(t)$ into the potential energy equation leads to

$$E_p = \frac{1}{2}KA^2\sin^2(wt + \emptyset)$$

Recall that the natural frequency w_o is given by

$$w_o = \sqrt{\frac{K}{m}}$$

Therefore

$$K = mw_o^2$$

Assuming $w = w_o$ and combining the kinetic and potential energies lead to the total energy of the system

$$E_T = E_k + E_p$$

$$= \frac{1}{2}mw_o^2A^2\cos^2(w_ot + \emptyset)$$

$$+ \frac{1}{2}mw_o^2A^2\sin^2(w_ot + \emptyset) = \frac{1}{2}mw_o^2A^2$$

Solving for A^2 gives

$$A^2 = E_T2mw_o^2$$

Therefore, A^2 is directly proportional to the total energy of the system. The rise of the energy term within this context is simple to understand by considering a

spring-mass system. Let's view the mass as kinetic energy storage and the spring as potential energy storage. While the spring is being stretched, kinetic energy of the mass is being converted into potential energy of the spring until the spring reaches a maximum potential energy, at which point the kinetic energy of the mass reaches zero. The spring is quickly released and is returning to its equilibrium position while all its potential energy is being converted back to kinetic energy of the mass. The energy transfer rate between the mass and the spring is equal to the natural frequency of the system. The intensity of oscillations on the other hand, is the square of the amplitude of the oscillations.

The FWHM and the resonance frequency characterize the resonance peak. Quality factor (Q) combines these parameters into one equation

$$Q = \frac{w_o}{\text{FWHM}} \tag{45}$$

Substituting our FWHM results for A and A^2 (energy) into Equation 45 gives

$$Q_A = \frac{w_o}{2\sqrt{3}c}$$

$$Q_{\text{energy}} = \frac{w_o}{2c}$$

The Q-factor is inversely proportional to FWHM. Heavily damped systems yield broader resonance curves and in response their Q is lower compared to lightly damped systems. Therefore, Q can be used as a measure of the sharpness of the resonance. Additionally, lower Q implies a higher damping c and therefore a higher rate of energy loss in comparison to the stored energy of the oscillator,

which means the oscillations diminish faster. Undamped tuning forks have Q that can reach 10,000 in air.

2.1.4 Driven Damped Harmonic Oscillator in Complex Notation

In the previous section we derived the differential equation of motion for a driven harmonic oscillator with damping as:

$$\frac{d^2x}{dt^2} + \frac{\gamma}{m}\frac{dx}{dt} + \frac{K}{m}x = \frac{F_o}{m}\sin(wt) \tag{22}$$

where the right side of the equation arises from a simple harmonic driving force

$$\vec{F}(t) = F_o \sin(wt) \tag{21}$$

In this section, we will describe the driven damped harmonic oscillator in complex notation.

We start by writing $\vec{F}(t) = F_o \sin(wt)$ as a complex number with a condition that a real part is equal to $F_o \sin(wt)$.

$$\hat{F} = F_o e^{i(wt+\Delta)} = F_o \cos(wt+\Delta) + iF_o \sin(wt+\Delta) \tag{46}$$

Equation 46 is a linear combination of a real part

$$F_r = F_o \cos(wt+\Delta) \tag{47}$$

and an imaginary part

$$F_i = iF_o \sin(wt+\Delta) \tag{48}$$

We set a condition $\Delta = -\pi/2$ to switch the cosine into sine in Equation 47.

$$\hat{F} = F_o e^{i(wt+\Delta)} = F_o e^{i\Delta} e^{iwt}$$

where we can define $\hat{F}_o$ as the complex constant

$$\hat{F}_o = F_o e^{+i\Delta}$$

Solution to this differential equation with a complex force $\hat{F}$

A complex solution takes this general form

$$\hat{x} = x_r + ix_i$$

Writing Equation 22 in complex notation yields

$$\frac{d^2\hat{x}}{dt^2} + \frac{\gamma}{m}\frac{d\hat{x}}{dt} + \frac{K}{m}\hat{x} = \frac{\hat{F}(t)}{m} \tag{49}$$

with

$$\frac{d\hat{x}}{dt} = \frac{dx_r}{dt} + i\frac{dx_i}{dt}$$

$$\frac{d^2\hat{x}}{dt^2} = \frac{d^2x_r}{dt^2} + i\frac{d^2x_i}{dt^2}$$

Substituting into Equation 49 gives

$$\frac{d^2x_r}{dt^2} + \frac{\gamma}{m}\frac{dx_r}{dt} + \frac{K}{m}x_r + i\left(\frac{d^2x_i}{dt^2} + \frac{\gamma}{m}\frac{dx_i}{dt} + \frac{K}{m}x_i\right) = \frac{F_r}{m} + i\frac{F_i}{m}$$

The real parts of the above equation are

$$\frac{d^2x_r}{dt^2} + \frac{\gamma}{m}\frac{dx_r}{dt} + \frac{K}{m}x_r = \frac{F_r}{m}$$

If we can solve this Equation 49 using complex numbers then we have solved the equation since the real components of the equation must be equal. This only works for linear equations.

So, we will attempt to solve the complex differential equation

$$\frac{d^2\hat{x}}{dt^2} + \frac{\gamma}{m}\frac{d\hat{x}}{dt} + \frac{K}{m}\hat{x} = \frac{\hat{F}_o}{m}e^{iwt} \tag{50}$$

A general solution (the steady-state solution) can take this form

$$\hat{x} = Ae^{i(wt + \Delta + \emptyset)} = \hat{A}e^{iwt} \tag{51}$$

First and second order differentiation with respect to time leads to

$$\frac{d\hat{x}}{dt} = \hat{A}iwe^{iwt}$$

$$\frac{d^2\hat{x}}{dt^2} = \hat{A}(-w^2)e^{iwt}$$

Substituting into Equation 50 yields

$$-\hat{A}w^2e^{iwt} + i\frac{\gamma}{m}\hat{A}we^{iwt} + \frac{K}{m}\hat{A}e^{iwt} = \frac{\hat{F}_o}{m}e^{iwt}$$

$$\Downarrow$$

$$\hat{A}\left(\frac{K}{m} - w^2 + i\frac{\gamma}{m}w\right) = \frac{\hat{F}_o}{m}$$

Substituting K/m by w_o^2 and γ/m by $2c$ gives

$$\hat{A} = \frac{\hat{F}_o}{m(w_o^2 - w^2 + i2wc)}$$

By substituting in Equation 51 we have

$$\hat{x} = \frac{\hat{F}_o}{m(w_o^2 - w^2 + i2wc)}e^{iwt} \tag{52}$$

So the amplitude of $\hat{x}$ can be obtained by

$$A = \sqrt{\hat{x}\hat{x}^*} = \sqrt{\frac{F_o \cdot e^{iwt}}{m(w_o^2 - w^2 + i2wc)} \cdot \frac{F_o \cdot e^{-iwt}}{m(w_o^2 - w^2 - i2wc)}}$$

$$\Downarrow$$

$$A = \sqrt{\frac{F_o^2}{m^2[(w_o^2 - w^2)^2 - (i2wc)^2]}}$$

$$\Downarrow$$

$$A = \frac{F_o}{m\sqrt{(w_o^2 - w^2)^2 + (2wc)^2}}$$

This is the same result obtained before, confirming Equation 32.

To obtain the phase shift Ø, we use

$$\hat{x} = Ae^{i(wt + \Delta + \emptyset)} = Ae^{i\emptyset}e^{i\Delta}e^{iwt}$$

$$\hat{A} = \frac{\hat{F}_o}{(w_o^2 - w^2 + i2wc)}$$

Since $\hat{F}_o = F_o e^{i\Delta}$ and $\hat{A} = Ae^{i\emptyset}e^{i\Delta}$ we have

$$Ae^{i\emptyset} = \frac{F_o}{m(w_o^2 - w^2 + i2wc)}$$

By substituting $e^{i\emptyset} = \cos\emptyset + i\sin\emptyset$

$$A\cos\emptyset + iA\sin\emptyset = \frac{F_o}{m(w_o^2 - w^2 + i2wc)}$$

Rearranging and grouping real and imaginary parts yield

$$A \cos \emptyset. m(w_0^2 - w^2) - A \sin \emptyset. m2wc$$

$$+ i[A \cos \emptyset. m2wc + A \sin \emptyset. m(w_o^2 - w^2)]$$

$$= F_o + i * 0$$

Real and imaginary parts must be equal, therefore

$$A \cos \emptyset. m(w_o^2 - w^2) - A \sin \emptyset. m2wc = F_o$$

$$A \cos \emptyset. m2wc + A \sin \emptyset. m(w_o^2 - w^2) = 0 \tag{53}$$

Rearranging Equation 53 gives

$$\sin \emptyset(w_o^2 - w^2) = -\cos \emptyset . 2wc$$

$$\Downarrow$$

$$\tan \emptyset = \frac{\sin \emptyset}{\cos \emptyset} = \frac{-2wc}{(w_o^2 - w^2)}$$

This is the same result as before, confirming Equation 29.

2.1.5 Modeling a Tuning Fork as a Driven Damped Harmonic Oscillator

Karrai and Grober[33] successfully modeled a tuning fork as a driven damped harmonic oscillator and described the tip-fork system quantitatively before and after approach.

Equation 50 can be rewritten as

$$m \frac{d^2 \hat{x}}{dt^2} + \gamma \frac{d\hat{x}}{dt} + K\hat{x} = \hat{F}_o e^{iwt}$$

where $\gamma = 2cm$. Let $\acute{\gamma} = 2c$, then $\gamma = m\acute{\gamma}$. Substituting this into our differential

equation yields

$$m\frac{\mathrm{d}^2\hat{x}}{\mathrm{d}t^2} + m\acute{\gamma}\frac{\mathrm{d}\hat{x}}{\mathrm{d}t} + K\hat{x} = \hat{F}_o\mathrm{e}^{\mathrm{i}wt}$$

Based on Karrai et al.[33], the time dependence of the tip position $x(t)$ is described

by an effective harmonic oscillator equation of motion driven at frequency w

$$m_{\mathrm{e}}\frac{\mathrm{d}^2\hat{x}}{\mathrm{d}t^2} + m_{\mathrm{e}}\acute{\gamma}\frac{\mathrm{d}\hat{x}}{\mathrm{d}t} + K\hat{x} = \hat{F}_o\mathrm{e}^{\mathrm{i}wt} \tag{54}$$

Where:

$\hat{F}_o$ is the amplitude of the driving force tuned by adjusting the voltage applied on

the dither piezoelectric element.

$\hat{F}_{\mathrm{D}} = m_{\mathrm{e}}\acute{\gamma}\frac{\mathrm{d}\hat{x}}{\mathrm{d}t}$ is the sum of all drag forces acting on the cantilever.

$m_e = 0.2427\,\rho\,L\,t\,w$ is the effective mass corresponding to about 1/4 of the total

mass of one prong.

ρ = 2.650 g/cm^3 = 2650 kg/m^3 is the density of quartz.

L, w and t = 4 mm, 0.4 mm and 0.6 mm respectively, are the dimensions of the

prong (see Figure 2.10).

$K = E.w.t^3/4L^3$ is the static compliance "spring constant" of cantilever.

$E = 7.87 \times 10^{10}\,\mathrm{N/m}^2$ is the cantilever's Young modulus.
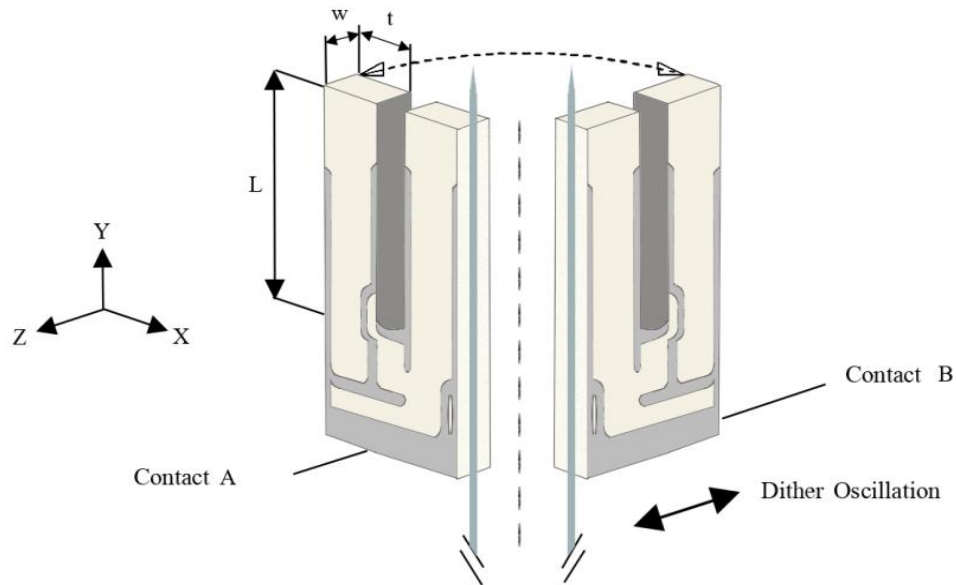
Figure 2.10 *Front and back view of a crystal quartz tuning fork with a 125 μm tapered fiber probe glued along one of its prongs. The tip protrudes 0.8 mm out of the prong's end (adapted from [33]).*

The solution for the above differential equation is

$$\hat{x} = \frac{\hat{F}_o}{m_e\left(w_o^2 - w^2 + i\acute{\gamma}w\right)}\; e^{iwt} \tag{55}$$

The natural frequency of the tuning fork can be expressed as follows

$$\acute{\gamma} = 2c \Rightarrow c = \acute{\gamma}/2$$

Substituting into the resonance frequency equation below yields

$$w_{res} = \sqrt{w_o^2 - 2c^2} = \sqrt{w_o^2 - (2c)c} \tag{33}$$

$$w_{res} = \sqrt{w_o^2 - \acute{\gamma}\frac{\acute{\gamma}}{2}} = \sqrt{w_o^2 - \frac{\acute{\gamma}^2}{2}}$$

For small drag ($\acute{\gamma} \ll w$) at resonance, $w_{res} \approx w_o$.

➤ **Evaluation of w_o**

We can calculate w_o by

$$w_o = \sqrt{\frac{K}{m_e}} = \frac{26.6 \times 10^3 \text{ N/m}}{0.2427 \times 2650 \text{ kg/m}^3 \, (4 \times 0.4 \times 0.6 \times 10^{-9}\text{m}^3)}$$

$$= 2.07 \times 10^5 \text{Hz} \cong (2\pi)32{,}768 \text{ Hz}$$

➤ **What is the tip amplitude at resonance A_{res}?**

The tip amplitude at resonance I given by Equation 34

$$A_{res} = \frac{F_o}{2mc\sqrt{w_o^2 - c^2}} \tag{34}$$

In terms of m_e and $\acute{\gamma}$, this can be rewritten as

$$A_{res} = \frac{F_o}{2m_e \frac{\acute{\gamma}}{2}\sqrt{w_o^2 - \left(\frac{\acute{\gamma}}{2}\right)^2}}$$

With assumption $(\acute{\gamma} \ll w_o)$

$$A_{res} = \frac{F_o}{m_e \acute{\gamma} w_o}$$

By applying the quality factor relations

$$Q = \frac{w_o}{\text{FWHM}}$$

$$Q_A = \frac{w_o}{2\sqrt{3}c} = \frac{w_o}{\sqrt{3}\acute{\gamma}}$$

we can write the amplitude as a function of Q

$$A_{res} = \frac{F_o}{m_e \acute{\gamma} w_o}\frac{w_o}{w_o} = \frac{F_o w_o}{K\acute{\gamma}}$$

$$A_{\text{res}} = \frac{F_o Q_A \sqrt{3}}{K}$$

➢ **Drag force experienced by the fork at peak resonance**

In general $\widehat{F}_D = m_e \acute{\gamma} \frac{d\hat{x}}{dt}$. Differentiating Equation 55 yields

$$\frac{d\hat{x}}{dt} = iw \frac{\widehat{F}_o}{m_e(w_o^2 - w^2 + i\acute{\gamma}w)} e^{iwt} \qquad (56)$$

Substituting into $\widehat{F}_D = m_e \acute{\gamma} \frac{d\hat{x}}{dt}$ yields

$$\widehat{F}_D = m_e \acute{\gamma} \, iw \frac{\widehat{F}_o}{m_e(w_o^2 - w^2 + i\acute{\gamma}w)} e^{iwt}$$

$$\Downarrow$$

$$\widehat{F}_D = im_e \acute{\gamma} \, w \, \hat{x}$$

At peak resonance $\hat{x} = A_{\text{res}}$ and $w \approx w_o$ (for small damping). This leads to

$$F_{\text{D,res}} = im_e \acute{\gamma} \, w_o \, A_{\text{res}}$$

Multiplying by w_o / w_o yields

$$F_{\text{D,res}} = \frac{im_e \acute{\gamma} \, w_o^2 \, A_{\text{res}}}{w_o}$$

Since

$$w_o = \sqrt{\frac{K}{m_e}} \rightarrow K = m_e w_o^2$$

we then obtain

$$F_{D,res} = \frac{iK\acute{\gamma}A_{res}}{w_o}$$

We can express $F_{D,res}$ in terms of quality factor Q_A

$$Q_A = \frac{w_o}{\sqrt{3}\acute{\gamma}} \Rightarrow \frac{\acute{\gamma}}{w_o} = \frac{1}{\sqrt{3}Q_A} \qquad (45)$$

Applying this result in our $F_{D,res}$ equation yields

$$F_{D,res} = \frac{iKA_{res}}{\sqrt{3}Q_A}$$

In order to evaluate $F_{D,res}$ we need to determine K, A_{res} and Q_A.

The static compliance K can be determined by the formula

$$K = \frac{E.w.t^3}{4.L^3} = \frac{(7.87 \times 10^{10} \text{ N/m}^2)(4 \times 10^{-4} \text{ m})(6 \times 10^{-4} \text{ m})^3}{4(4 \times 10^{-3} \text{ m})^3}$$

$$K = 26.6 \times 10^3 \text{ N/m}$$

The quality Q factor is quantitatively obtained by measuring the full frequency width at half-maximum of the piezoelectric signal amplitude resonance.

Q for bare tuning forks can reach 10,000 in air and up to 64,000 in vacuum. Q in air is usually reduced to about 1000, however, when a fiber probe is glued along one of the prongs.

A_{res} can be determined experimentally (interferometry measurements). Using this technique, the resonance piezoelectric signal of the tuning fork v_{res} is calibrated against A_{res}. A typical value of amplitude at resonance is $A_{res} = 0.35$ nm, at which tip-sample approach is normally operated. The measured dependence of the resonance piezoelectric signal on the oscillation amplitude is

27 µV/nm. Therefore at peak amplitude; we get a maximum piezoelectric signal v_{res} of

$$v_{res} = 0.35 \text{ nm} \times 27 \ \mu V/nm = 9.45 \ \mu V \cong 10 \ \mu V$$

Figure 2.11 shows the amplitude of the piezoelectric signal (in µV) and the tip amplitude (in nm) as function of the driving frequency. Based on these results, the drag force in absence of tip-sample interaction is evaluated as follows

$$\widehat{F}_{D,res} = \frac{iKA_{res}}{\sqrt{3}Q_A} \Rightarrow \left|F_{D,res}\right| = \sqrt{\frac{iKA_{res}}{\sqrt{3}Q_A}\frac{-iKA_{res}}{\sqrt{3}Q_A}} = \frac{KA_{res}}{\sqrt{3}Q_A}$$

By substituting the predetermined parameters, $F_{D,res}$ can be calculated

$$\left|F_{D,res}\right| = \frac{KA_{res}}{\sqrt{3}Q_A} = \frac{(26.6 \times 10^3 \text{N/m})(0.35 \times 10^{-9} \text{m})}{\sqrt{3}(1000)}$$

$$\left|F_{D,res}\right| = 5.4 \times 10^{-9} \text{N} = 5.4 \text{ nN}$$

This represents the drag force originated from internal friction of the fork/fiber system.

When the sample is approached by the tip, some parameters of the system stay unaffected, while others show dependence on the tip-sample interaction. The following parameters stay unchanged:

L, w, t, ρ, m_e, E, K (dynamics of the cantilever), F_o (driving amplitude), w (driving frequency), w_o (oscillator frequency, still under assumption $w_{res} = w_o$)
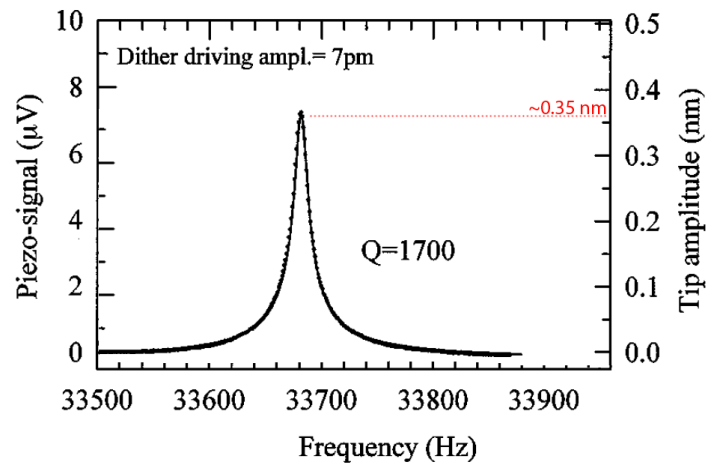
Figure 2.11 *Amplitude of the piezoelectric signal (µV) and tip amplitude (nm) as function of the driving frequency (Hz) (adapted from* [33] *).*

On the contrary, tip-sample interaction induces reduction in A_{res} and Q_A in the same proportion. This direct proportionality is shown in the equation

$$A_{\mathrm{res}} = \frac{F_o Q_A \sqrt{3}}{K}$$

$$A_{\mathrm{res}} = \left(\frac{F_o \sqrt{3}}{K} \right) Q_A$$

<div style="text-align:center; color:red;">constant</div>

In general, the following system characteristics are altered when the tip is in interaction range with the sample:

$\acute{\gamma}$ increases (to $\acute{\gamma}_{\mathrm{sf}}$) because of additional shear force F_{sf}, i.e. $\acute{\gamma}_{\mathrm{sf}} > \acute{\gamma}$

Amplitude decreases to $A_{\mathrm{res},\mathrm{sf}} = \dfrac{\acute{\gamma}}{\gamma_{\mathrm{sf}}} A_{\mathrm{res}}$

Q_A decreases to $Q_{A,\mathrm{sf}} = \dfrac{\acute{\gamma}}{\gamma_{\mathrm{sf}}} Q_A$

v_{res} decreases (piezoelectric signal) to $v_{\text{res,sf}} = \dfrac{\dot{\gamma}}{\dot{\gamma}_{\text{sf}}} v_{\text{res}}$

These changes can be viewed jointly in the following relations

$$\frac{\dot{\gamma}}{\dot{\gamma}_{\text{sf}}} = \frac{A_{\text{res,sf}}}{A_{\text{res}}} = \frac{Q_{A,\text{sf}}}{Q_A} = \frac{v_{\text{res,sf}}}{v_{\text{res}}}$$

Since A_{res} and Q_A change by the same factor, the drag force $F_{\text{D,res}}$ remains

unchanged at about 5.4 nN on interaction. This can be viewed from the equation

$$F_{\text{D,res}} = \underbrace{\left(\frac{K}{\sqrt{3}}\right)}_{\text{constant}} \frac{A_{\text{res}}}{Q_A}$$

Since the tip is in frictional motion parallel to the sample surface, the shear force

stemming from the tip-sample interaction F_{sf} is a drag force contributing to $F_{\text{D,res}}$.

Therefore, before approach $\left|F_{\text{D,res}}\right| = 5.4$ nN and is solely limited to internal

friction $\left|F_{\text{D,res}}\right| = F_{\text{int}}$, and after approach (on tip-sample interaction), the drag

force stays unchanged $\left|F_{\text{D,res}}\right| = 5.4$ nN and comprised of internal friction

$F_{\text{int,sf}}$ plus shear forces F_{sf}, $\left|F_{\text{D,res}}\right| = F_{\text{int,sf}} + F_{\text{sf}}$

Assuming $F_{\text{int,sf}}$ is directly proportional to the amplitude after approach

$(F_{\text{int,sf}} \propto A_{\text{res,sf}})$, we obtain

$$F_{\text{int,sf}} = \frac{\dot{\gamma}}{\dot{\gamma}_{\text{sf}}} F_{\text{int}} = \frac{\dot{\gamma}}{\dot{\gamma}_{\text{sf}}} \left|F_{\text{D,res}}\right|$$

This leads to

$$F_{\text{sf}} = \left|F_{\text{D,res}}\right| - F_{\text{int,sf}} = \left|F_{\text{D,res}}\right| - \frac{\dot{\gamma}}{\dot{\gamma}_{\text{sf}}} \left|F_{\text{D,res}}\right|$$

$$F_{sf} = |F_{D,res}| \left(1 - \frac{\acute{\gamma}}{\acute{\gamma}_{sf}}\right)$$

$$F_{sf} = |F_{D,res}| \left(1 - \frac{v_{res,sf}}{v_{res}}\right)$$

A 1% decrease in v_{res} corresponds to

$$F_{sf} = 5.4 \text{ nN} \left(1 - \frac{9.9 \text{ μV}}{10 \text{ μV}}\right) = 0.054 \text{ nN}$$

Also, the shear force acting on the tip can be up to 2 nN without aperture damage and up to 40 nN before tip damage. Thus, topographic NSOM images can be obtained with a 37% piezoelectric signal reduction, which corresponds to about 10 nm working distance (Figure 2.12).

$$2 \text{ nN} = 5.4 \text{ nN.} \left(1 - \frac{v_{res,sf}}{v_{res}}\right)$$

$$\frac{2 \text{ nN}}{5.4 \text{ nN}} = 1 - \frac{v_{res,sf}}{v_{res}} = 0.37 \implies \frac{v_{res,sf}}{v_{res}} = 0.63$$
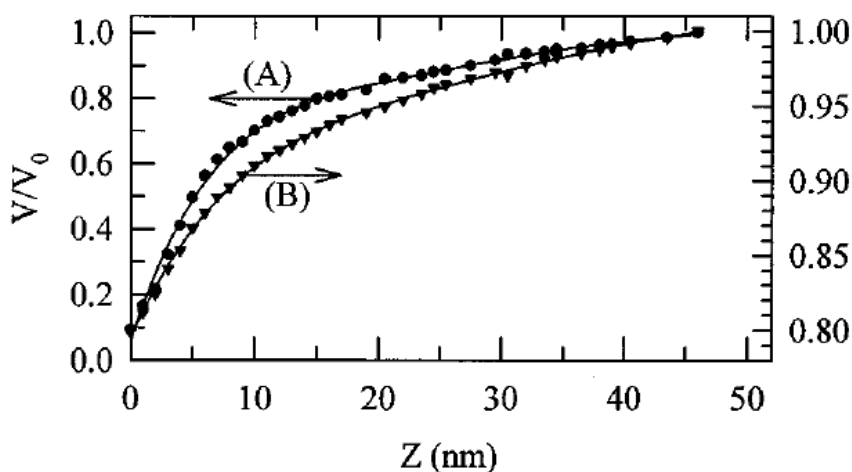
Figure 2.12 *Approach curves of the normalized signal amplitude at resonance frequency as function of the tip-sample distance. **Curve A**: The signal results from an optical measurement of the amplitude of a resonance mode of the tip. **Curve B**: is the simultaneous measured piezoelectric signal of the tuning fork*[33].

Oscillating the running fork at high Q, allows for the detection of shear force interactions as low as 50 pN. Although high Q gives high sensitivity to the TF crystal, it contributes to slowing down the scanning speed by causing relatively long damping time. When the TF is displaced from equilibrium, the prong's amplitude relaxes exponentially with a rate $\tau = \sqrt{3}/(\pi\,\mathrm{FWHM})$. High Q means low width of the TF resonance curve, and therefore high time constant. Using $\mathrm{FWHM} = 30\ \mathrm{Hz}$, the time constant can be evaluated to $\tau = 18\ \mathrm{ms}$. Therefore, for high-resolution imaging, the scan speed needs to be sufficiently slow to give the TF time to react to change in sample topography.

Chapter 3

Design and Instrumentation

In this chapter, we will discuss the design and construction of our NSOM module for inverted optical microscopes.

There are several components that make up NSOM today. These components can be grouped into three main categories: Optical, mechanical and electronic components.

3.1 Optical Components

Typically, these components consist of the light source, various optical elements such as mirrors, prisms, lenses, fibers, polarizers, objectives and photodetectors. The main optical components constituting our NSOM are shown in Figure 3.1 and detailed herein:

1. The light source: Argon ion laser (Stabilite 2017, Spectra-Physics) operating at a wavelength of 514 nm.

2. Polarizers:

- Glan-Taylor prism (Casix): This polarizer ensures that only *p*-polarized light is transmitted. It has a wavelength range of 350-2300 nm and an extinction ratio less than $5x10^{-5}$. It is coated with a single layer MgF_2 on Input and output surface with black anodized Aluminum as housing.

- Fresnel Rhomb prism (Casix): This prism is used to convert linearly polarized light into circularly polarized light. It is made of UV grade fused silica with 200-2000 nm wavelength range and λ/4 retardation.

3. Mirrors (Casix): Au metal coated mirrors with λ/4 flatness.

4. Optical fiber (Nufern #S405-HP): Single-mode pure silica core fiber optimized for use at visible wavelengths from 400 up to 550 nm. Geometrical specifications include a core diameter of 3 μm, 125.0 ± 1.0 μm cladding diameter and 245.0 ± 15.0 μm coating diameter. Operating temperature range -60 to 85 °C.

5. Objectives: 10x and 40x.

6. Intensity stabilizer (Brockton Electro-Optics, model LS-PRO): This laser Intensity stabilizer reduces laser noise and drift by a factor of up to 400 over a wide range of wavelengths and laser powers.

7. Photodetectors: Cascade CCD camera for fluorescence imaging and a XLI camera for birghtfield microscopy.
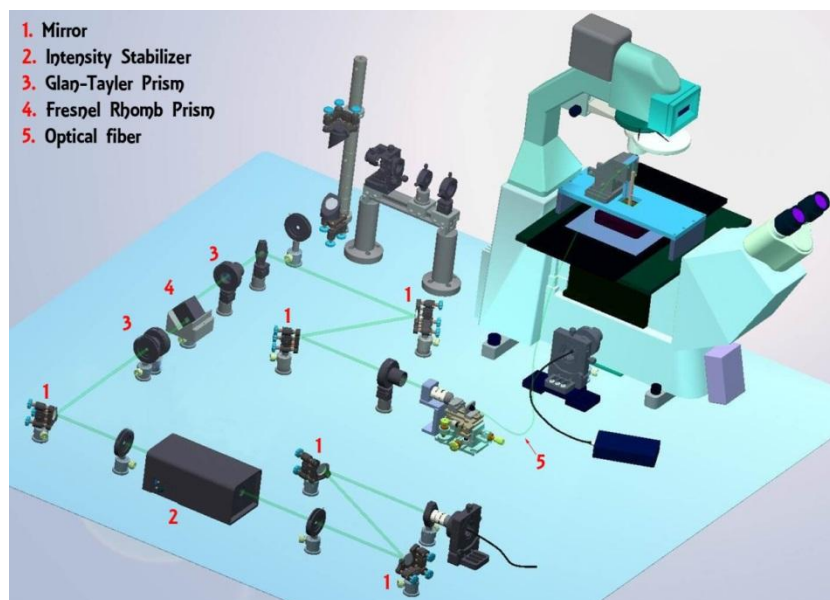
Figure 3.1 *Main optical components of our NSOM setup.*

3.2 Mechanical Components

The mechanical components include a translation stage, an anti-vibration table, piezo scanners and the various holders for the objectives, fibers and other optical elements. Next we will discuss the main mechanical components used in our experimental setup:

1. *XYZ* translational stage (New Focus, Gothic-Arch Translation Stage 9062-*XYZ*): This stage is fabricated in stainless steel and has a platform size of 40x40 mm^2 (Figure 3.2).
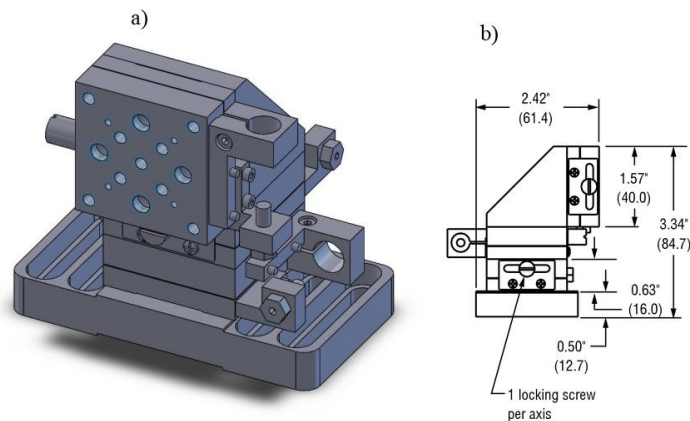
Figure 3.2 *a) Illustration of New Focus, Gothic-Arch Translation Stage 9062-XYZ b) drawing of the stage showing the dimensions in inches and millimeters. This drawing is adapted from Newport*[36].

The stage is equipped with three Picomotor™ actuators (SN #007190, #007539 and #006781) integrated on *x*, *y* and *z* axes. Each motorized actuator has a 12 mm travel range with 30 nm per step linear resolution. The maximum load an actuator can exert is about 5 lbs (22 N), which is ideal for mounting additional parts to the system. Moreover, these actuators can hold their position with no power applied, which makes them ideal for scanning a sample over a relatively long period of time (a few days) with numerous stoppages in between. Figure 3.3

shows a typical motorized Picomotor and our *xyz* translation stage after being

loaded with the three (*x,y* and *z*) Picomotors.
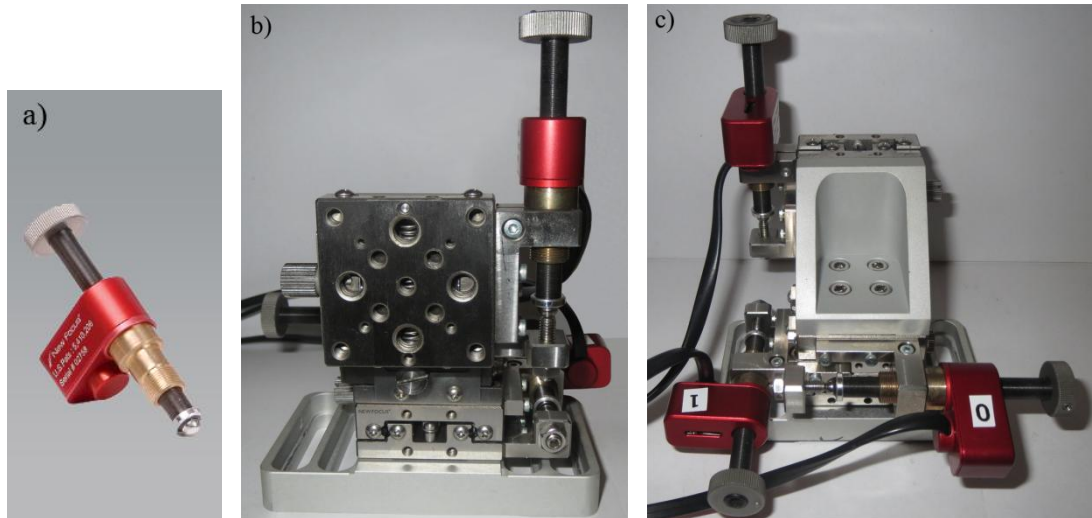
Figure 3.3 *a) Typical motorized Picomotor used in the translation stage. b) Front view of the xyz translational stage with x, y and z Picomotors integrated along the axes. c) Back view of the stage.*

The Picomotor drivers generate the electronic pulses that provide open-loop

control of the Picomotors. The Picomotor Ethernet Controller (model #8752)

offers a compact and versatile method for controlling the Picomotors as it can

drive the three individual Picomotors simultaneously through its three 4-pin

single-channel output ports. The Picomotor Ethernet Controller can be used to

interface a computer using a standard Ethernet communication port, or serial

interface. Additionally, it can be used with Hand Terminal (model #8757) and

Joystick (model #8754) for manual control of Picomotors (Figure 3.4).

We use the *xyz* translation stage to position the fiber on the optical axis and to

bring the tip into the general vicinity of the sample (≈ 1 mm).
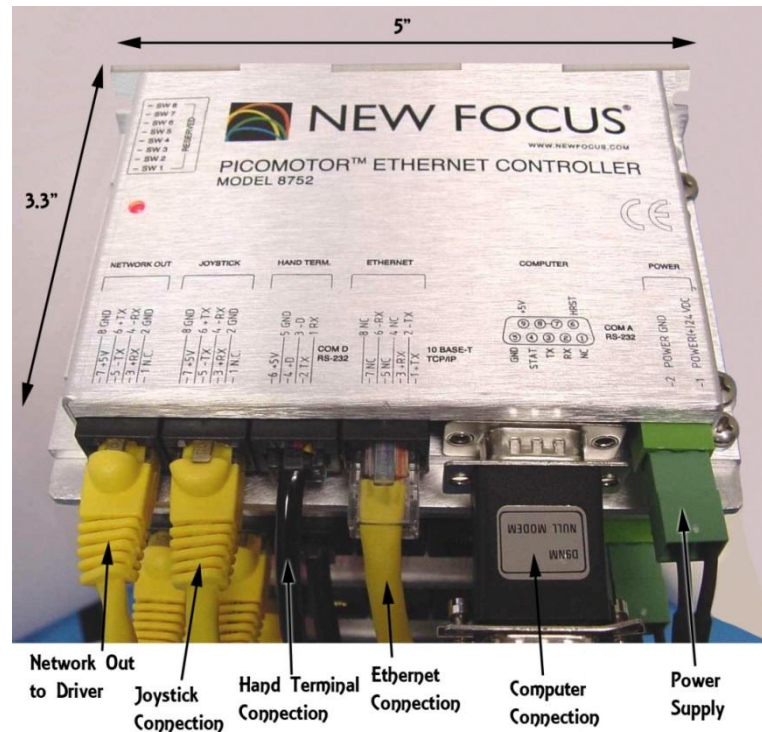
Figure 3.4 *Picomotor Ethernet Controller with all available ports.*

To be able to employ the translation stage in our setup, custom-made attachment pieces have been fabricated to fit the platform of the stage. The choice of material is stainless steel for its stability and chemical corrosion resistance. The first two parts that were machined are identical to each other and are directly attached to the translation stage platform (Figure 3.5). The height of each piece is 40 mm, which matches the edge length of the *xyz* stage platform. Mounting these two pieces onto the platform creates a track channel that supports the insertion of a custom-made "slider" piece. The lower end of the slider piece has a curved edge to facilitate the insertion and removal before and after experiments. As shown in Figure 3.6a, this piece is equipped with mounting holes on the front face to enable the permanent attachment of a separate piezoelectric *z*-scanner mount. The mount features a M3 coarse-threaded 8 mm-deep hole located on the bottom

side to accommodate a piezoelectric *z*-scanner (Figure 3.6b). Coupling of the

slider piece and the *z*-scanner mount is shown in Figure 3.6c, insertion of which

into the chancel track (shown in Figure 3.5b) results in the composite assembly

(Figure 3.6d).
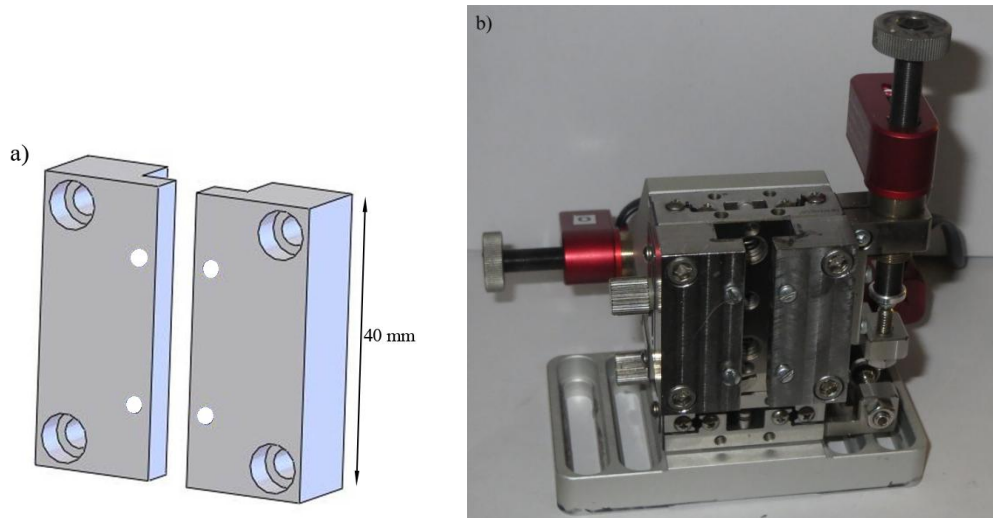
Figure 3.5 *a) Drawing of the first two machined attachments to the xyz translation stage, b) the attachments mounted on the platform of the translation stage.*

2. Piezoelectric *z*-scanner: The *xyz* translation stage provides a "coarse"

positioning system for bringing the tip into the general vicinity of the sample. In

order to achieve fine positioning at the sub-nanometer level, a piezoelectric *z*-

scanner (piezo tube actuator) is employed. In the search for a *z*-scanner, we

have determined that the following factors constitute an "ideal" scanner for our

setup:

a) Enclosure for housing the piezoscanner plays an important role in our

selection since bare scanners lack both mechanical stability electrical shielding.

b) Push/pull force capacity is another important factor as it determines the amount of forces a scanner can exert at a given time. In general, piezoelectric scanners are more sensitive to pulling forces. This is particularly critical because the tip, tuning fork and other *z*-scanner attachments add extra weight that translates into pulling forces during experiments.
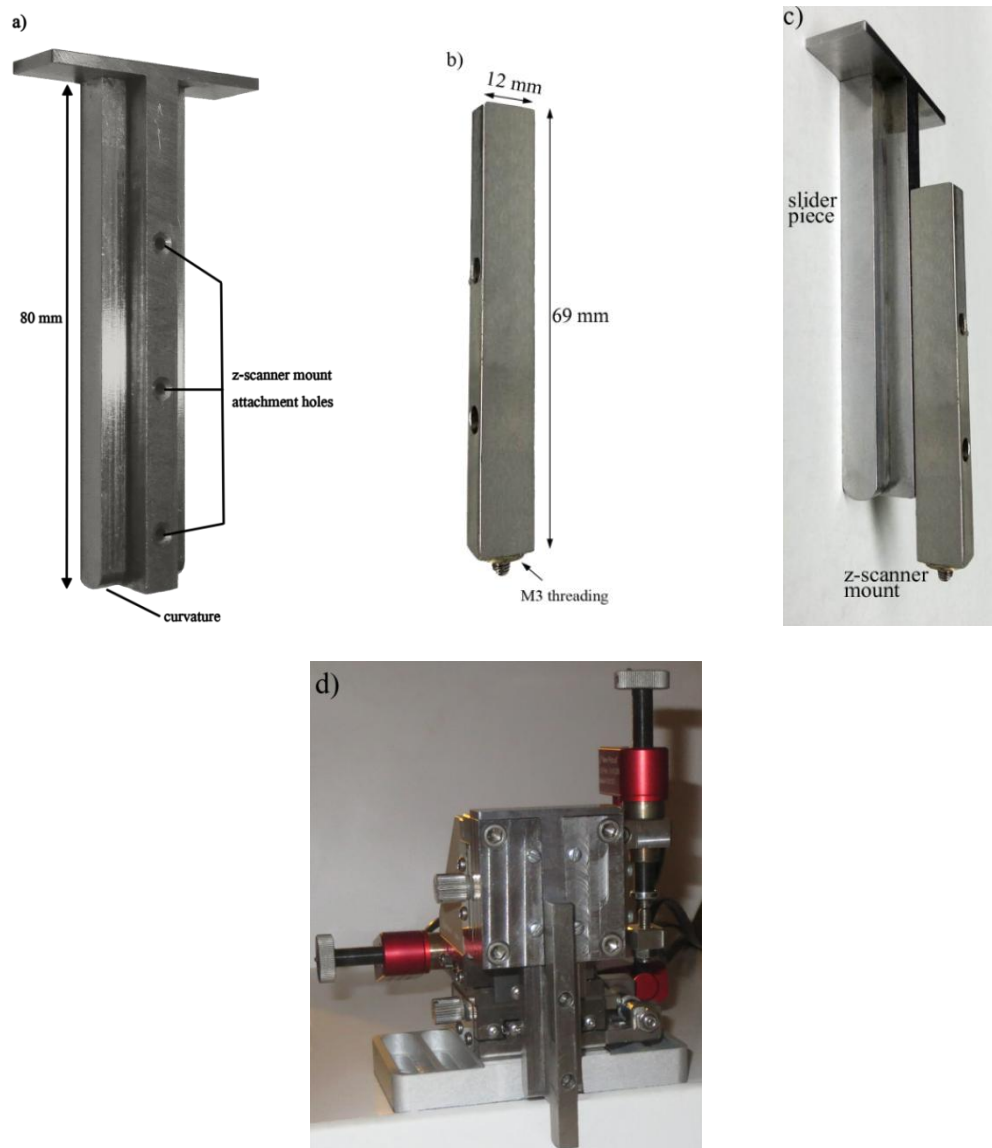
Figure 3.6 *a) Our custom-made slider piece. b) Piezoelectric z-scanner mount. c) Coupling of the slider piece and the z-scanner mount. d) Assembly resulted from insertion the coupled parts in c) into the chancel track.*

We have calculated that a piezo tube actuator with a push/pull force capacity of 50/1 N (Physik Instrumente, model P-810.10) would not meet the physical requirements. Therefore, the search has led to model P-820.10 which has a push/pull capacity of 50/10 N. This actuator is in a relaxed state at 0 V and expands approximately 15 µm at 100 V, with a linear resolution of 0.15 nm (Figure 3.7).
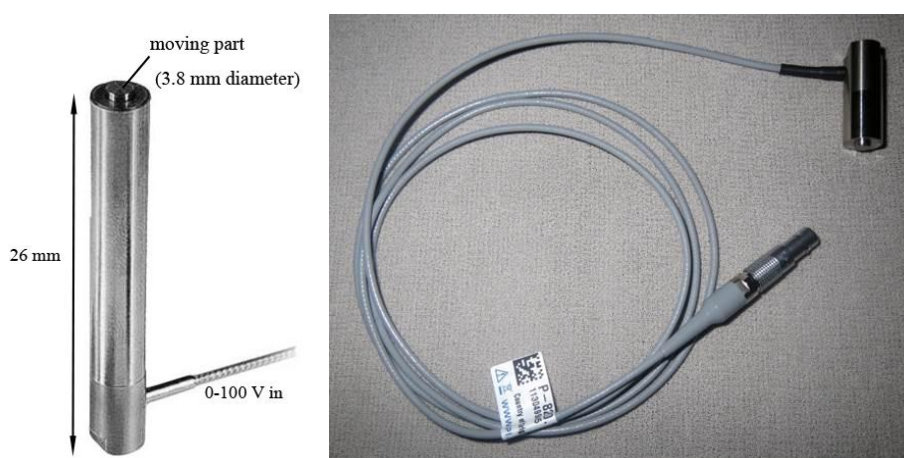
Figure 3.7 *The piezoelectric z-scanner (P-820-10) employed in our setup for fine positioning of the optical fiber tip above the sample surface.*

As shown in Figure 3.7, the moving part (piston) of the scanner is the small disk located at the top of the scanner body and has a diameter of 3.8 mm and a height of about 1 mm. For practical reasons, we have created a "spacer" piece that is rigidly glued (by J-B Weld 8265-S epoxy adhesive) to the moving part. This enables us to use the scanner more efficiently by extending the moving part away from the scanner body, thus creating more room to add other necessary attachments (Figure 3.8). The spacer head has two 1.4 mm Ø dents (only one can be seen in the Figure) that are used for locking our "support" piece which will be discussed later in this section.
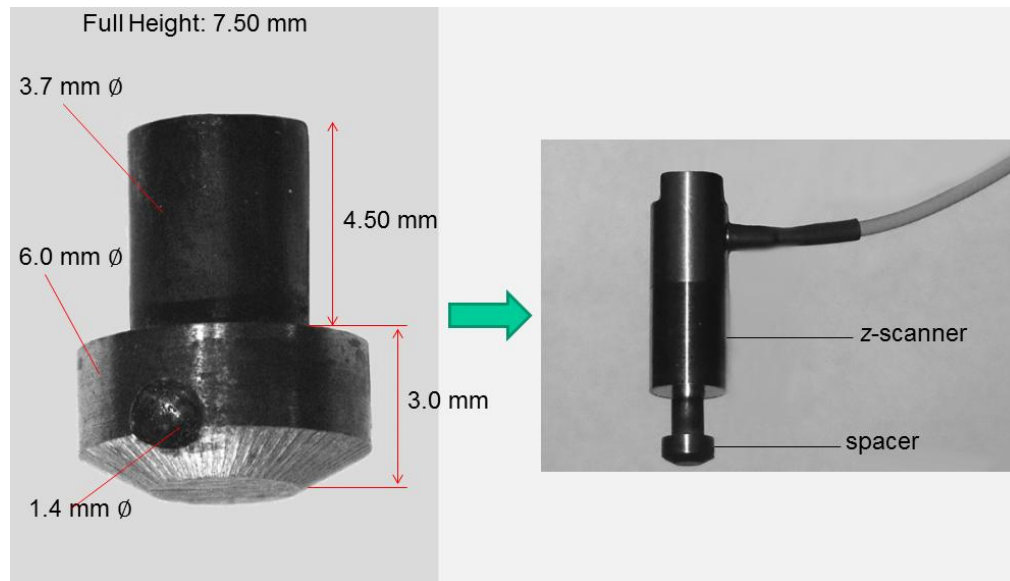
Figure 3.8 *(Left) A close-up of custom-fabricated spacer piece. (Right) The spacer piece after being rigidly glued to the piezoelectric z-scanner (P-820-10).*

3. Tuning fork and dither piezo: A tuning fork (TF) is employed as a means of sensing the vertical position of the tip. We use commercial grade tuning forks with common resonance frequency of 32,768 Hz (Newark part #13J1829). Quartz crystals of newly ordered tuning forks come protected in plastic caps (Figure 3.9a). These caps are glued to the base of the fork and need to be gently removed using a tool such as plier (Figure 3.9b). After removal of the cap, the two leads serving as piezoelectric signal pickup are bent by carefully heating their soldier joints with a soldier gun for a few seconds and letting them fall naturally under the effect of gravity. Bending the leads is necessary from a practical standpoint since it allows gluing the tuning fork on its non-conductive base (Figure 3.9c). To implement the TF in our setup, we have fabricated a "support" piece onto which the TF can be glued. This piece also features a specially

designed 500 µm groove for hosting and guiding the fiber probe and lining it up along the same level of the TF prong (Figure 3.10).
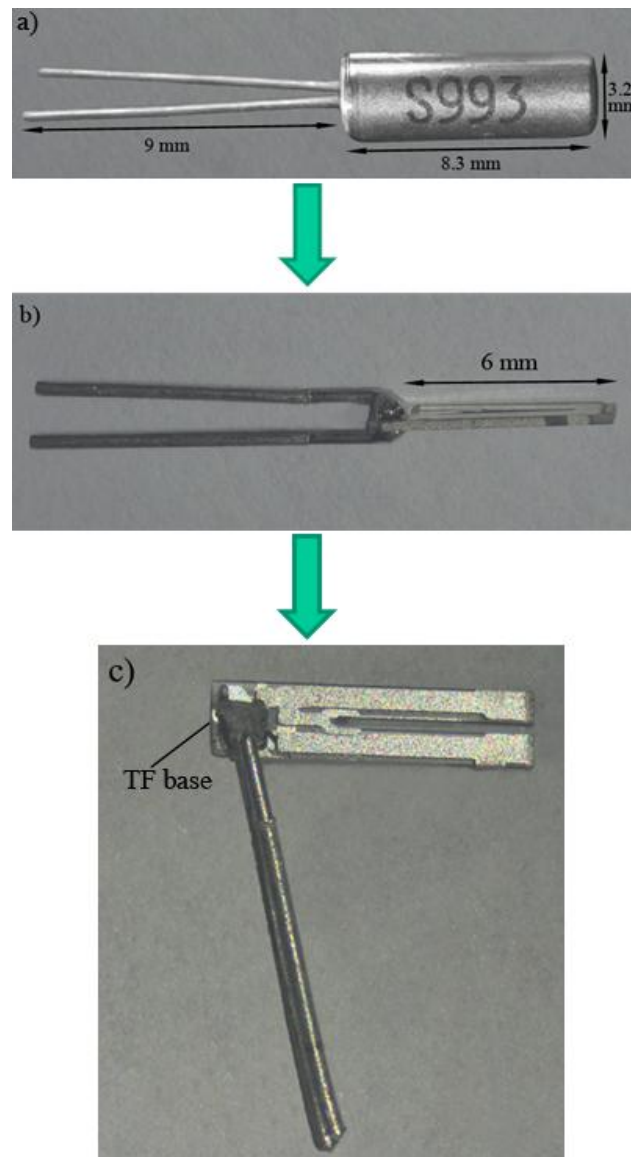
Figure 3.9 *a) A tuning fork with the protective cap still on. b) The TF after removal of the protective cap. c) The TF after bending the contacts with a soldier gun.*

The two threaded holes with 6-32x1/16" set screws (1/16" long, 32 threads per inch, 1/32" socket head) are used to securely attach the support piece to the spacer (which is rigidly glued to the *z*-scanner as described above). To prevent

parts loosening due to vibration and to protect threads from corrosion,

Threadlocker (Permatex #24206) is applied to the threads before experiments.

Figure 3.10 *Three different views of the support piece showing the 500 μm fiber guide (groove) and the two set screws for locking the support piece into the spacer. (Bottom, right) Before and after the application of Threadlocker to the threads of the locking set screws.*

Figure 3.11 illustrates the coupling of the support piece into the spacer's two

dents using the two locking set screws. It is important that these parts are well

fitted so that mechanical vibrations are kept minimal during the tip-sample

approach and the subsequent scanning of the specimen.
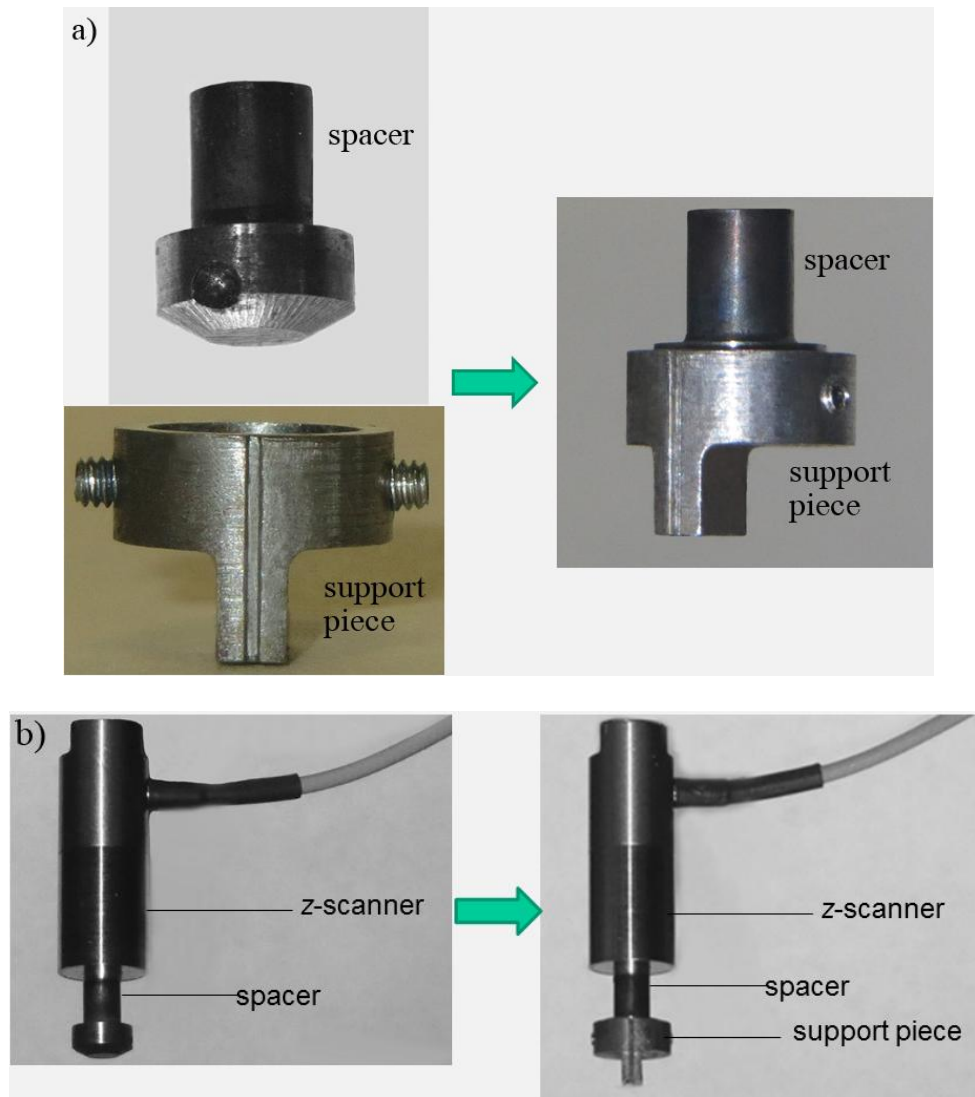
Figure 3.11 *a) A close-up view of the attachment of the support piece to the spacer using the two locking set screws. b) The support piece coupling with the spacer in relation to the piezoelectric z-scanner.*

In order to excite the mechanical vibrations of the TF, a dither piezoelectric element is rigidly glued to the support piece. We use an ultra-compact $2 \times 2 \times 2$ mm^3 multilayer actuator (Physik Instrumente, PL022.31), with 2.2 μm displacement at maximum applied voltage of 100 V. This model has the advantage over other actuators (for example the PL022.30) of having the wire leads already soldered to the appropriate electrodes, eliminating the need for

manual soldering of wires to the piezo chip, which could expose the actuator to thermal damage if temperatures exceed 320 °C for longer than 3 seconds (Figure 3.12).
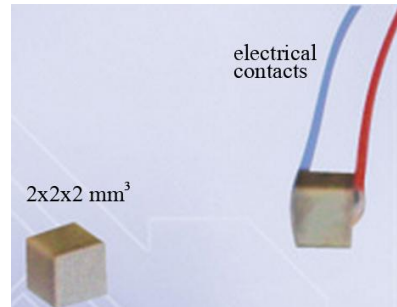
Figure 3.12 *Illustration of the piezoelectric actuator (PL022.31) used to excite the mechanical vibration of the tuning fork.*

The piezo actuator is permanently attached to the support piece using a 2-component epoxy (Devcon, # 31345). Figure 3.13 shows the result of this attachment (wire leads are not shown in this Figure). It is important that this bond is very strong so that the oscillations generated from the mechanical vibrations of the piezo actuator are transferred efficiently to the tuning fork with minimum damping arising from the bond.
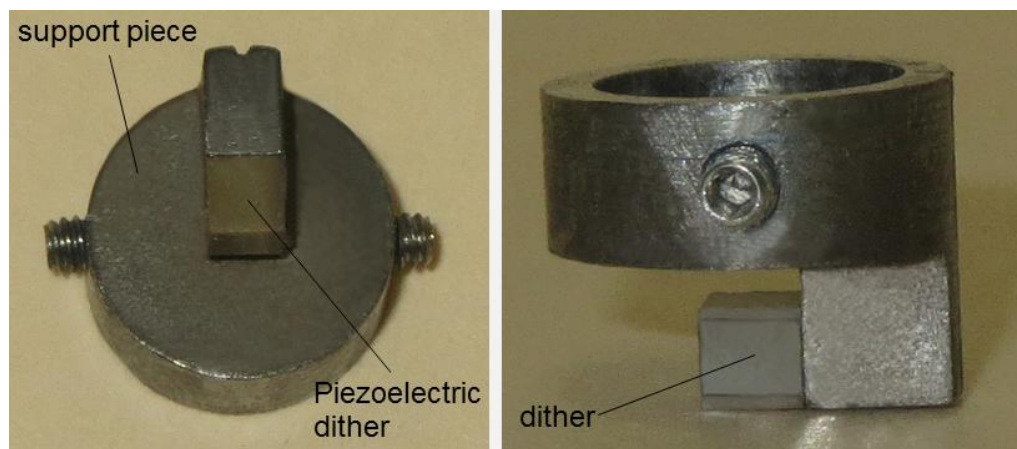
Figure 3.13 *Permanent attachment of the piezoelectric actuator (PL022.31) to the support piece (different views).*

Our next step requires the attachment of a tuning fork onto the support piece. Earlier attempts of gluing a TF onto the support piece yielded inconsistent resonance curves of the fork. Since this process is done regularly, a more dependable procedure has been developed in which reproducible coupling of the TF-support piece can be achieved. This involves the design and fabrication of a Teflon glue fixture that accommodates both the TF and support piece and allows for their precise alignment, which leads to consistent attachments (Figure 3.14).
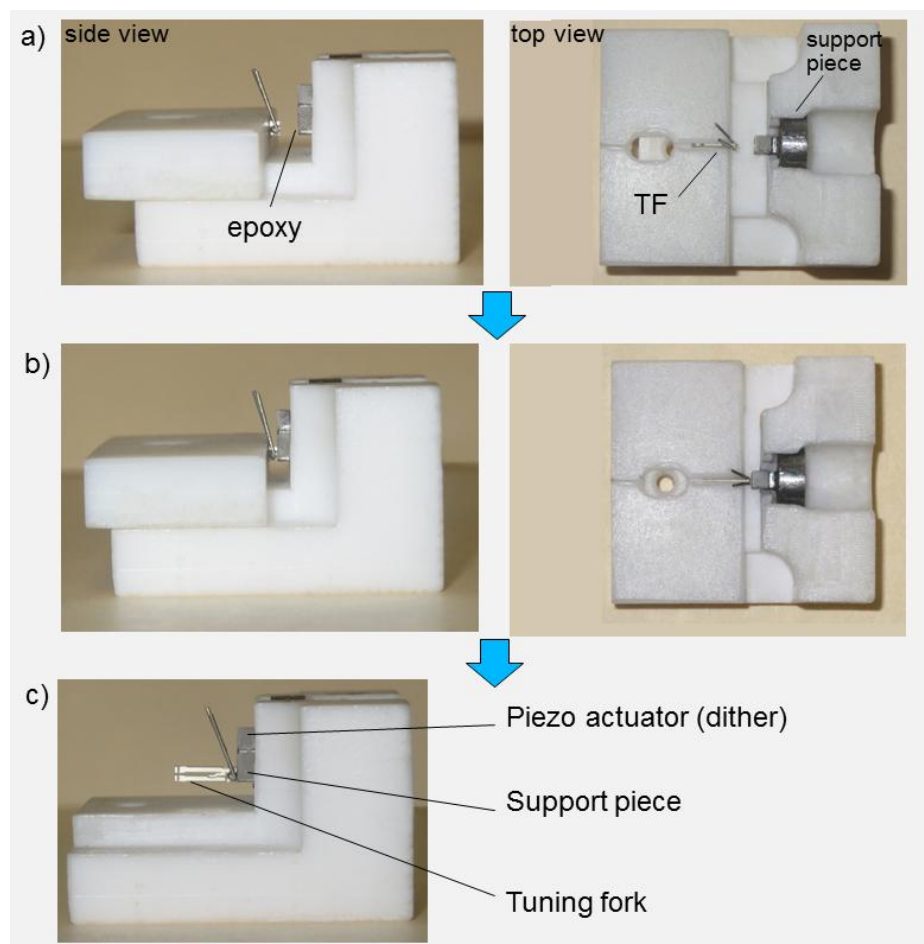
Figure 3.14 *a) Side and top views of the Teflon glue fixture showing the precise alignment of the TF with the support piece. b) Curing of the TF-support piece epoxy bond. c) Side view of the glue fixture after curing of the TF-support piece bond.*

After the epoxy bond has cured as in Figure 3.14c, the support piece is carefully

slid out of the glue fixture yielding the final assembly shown in Figure 3.15.

Figure 3.15 *Different views of the support piece after the TF attachment, also showing the previously glued piezoelectric dither.*

Under ambient conditions, typical 2-component epoxies can take hours to cure.

This translates to downtime periods during which the system is unavailable.

To speed up the process, we use a combination of a UV-cure system (Thorlabs,

ELC-410) and light cure adhesive (Loctite #3491) to produce TF-support piece

strong coupling in a short amount of time (1-3 minutes) (Figure 3.16).
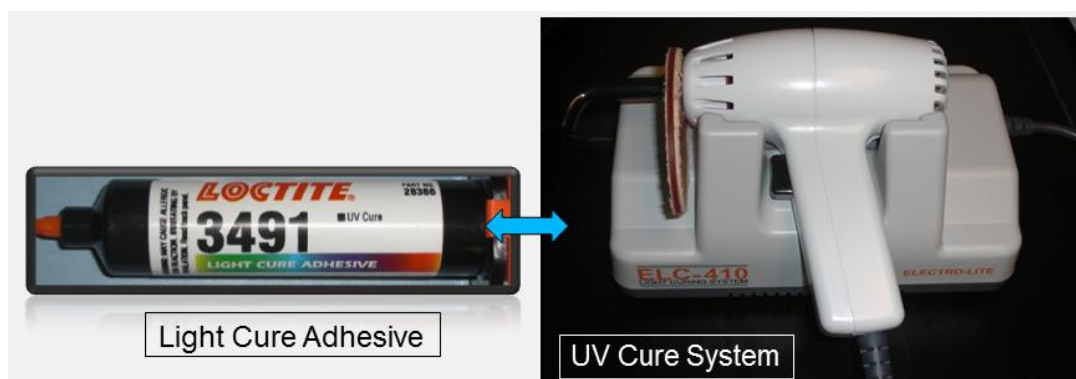
Figure 3.16 *The combination of Loctite #3491 light cure adhesive with ELC-410 UV-cure system yields very strong bonds with 1-3 minutes of UV exposure.*

4. Optical fiber tip attachment: Minimal amount of the light cure adhesive (Loctite #3491) is placed on the end of one of the prongs of a TF, followed by positioning a chemically etched optical fiber along the side of the prong, while extruding about 0.8 mm out of the prong's end. Subsequently, curing of the adhesive is carried out by shining UV light from the UV-cure system into the TF-fiber interface for 1-3 minutes (Figure 3.17).
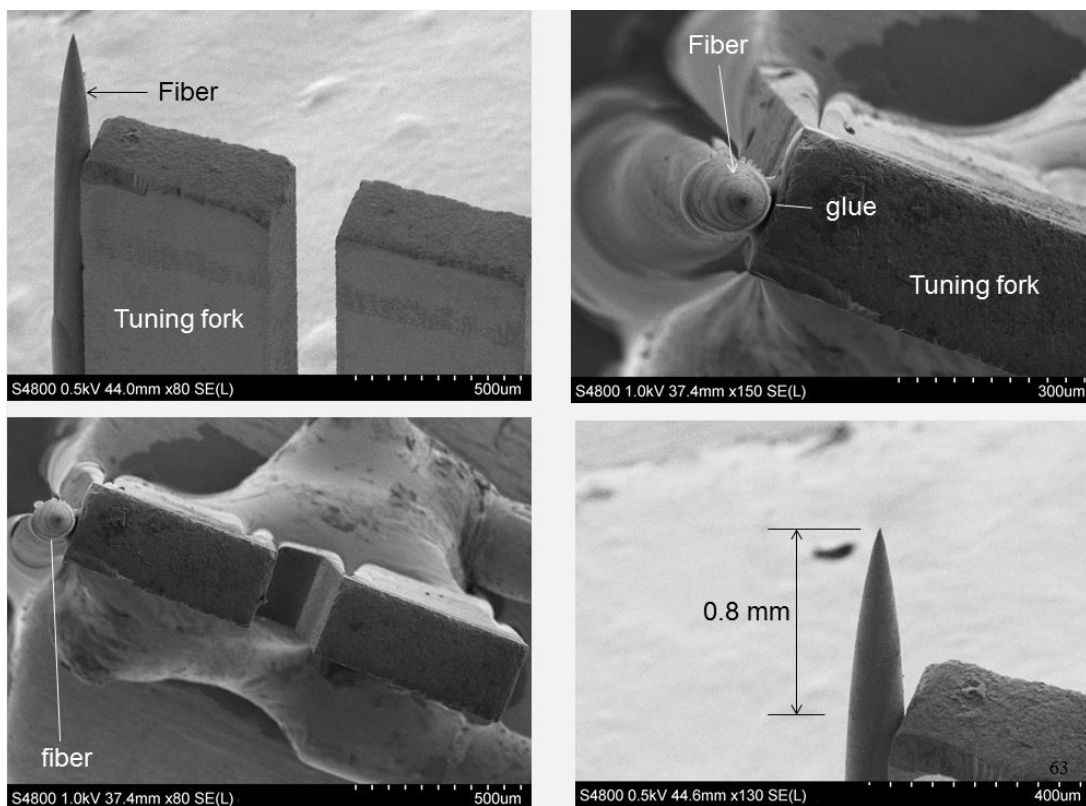
Figure 3.17 *SEM images of a TF with an optical fiber probe attached along the side of one of its prongs while extruding out of the prong by about 0.8 mm.*

5. Platform: A stainless steel platform that supports the mechanical, optical and electrical components of the NSOM module atop of our inverted microscope was designed and fabricated (Figure 3.18). During operation, the platform is tightly

fixed onto the inverted microscope (Zeiss Axiovert 200M) with the aid of four 45 mm-long stainless steel socket head cap screws (Mcmaster # 92290A260) which are tightened into the corresponding threaded holes on microscope.
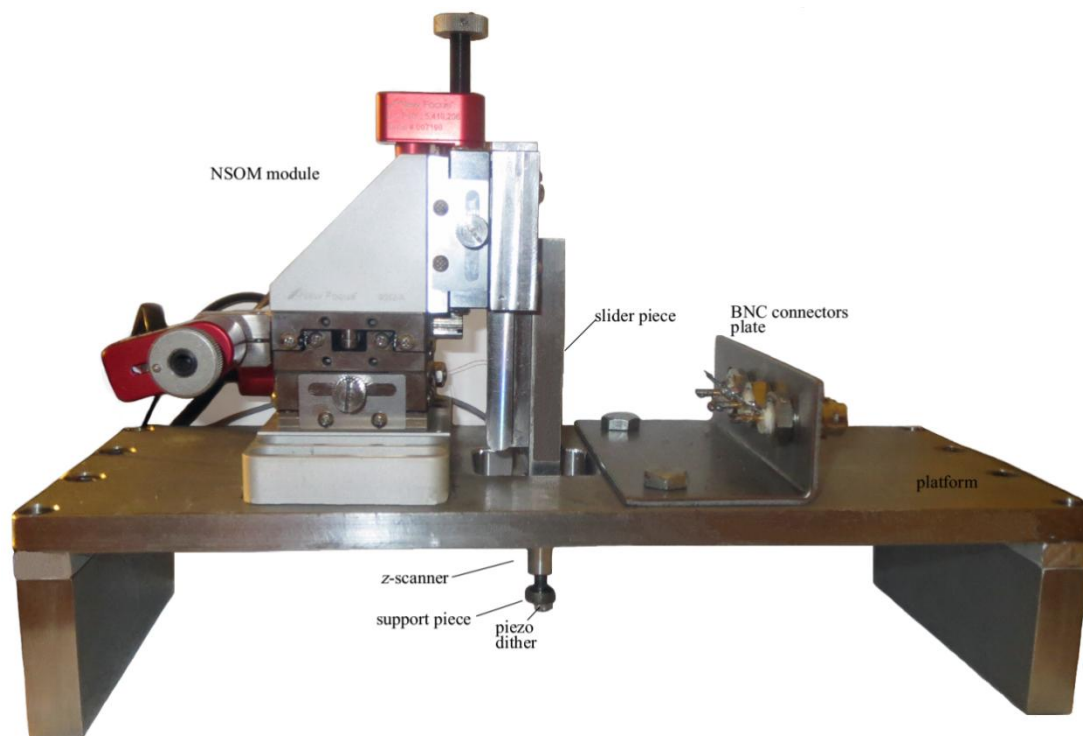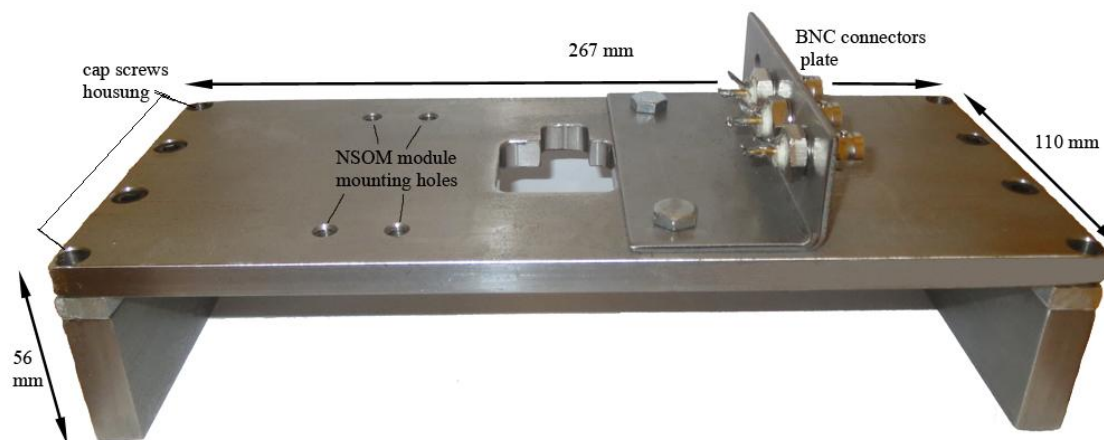
Figure 3.18 (Top) Custom-made stainless steel platform for the support of NSOM module. (Bottom) NSOM module mounted on top of the platform.

6. *XY*-piezoelectric scanner: When the tip is in interaction range with the specimen's surface, raster scanning of the sample is conducted by moving the sample under the probe, while the tip stays fixed in x and y. This ensures that the laser illumination and probe alignment are maintained, and also eliminates any noise resulting from moving the elastic fiber probe across the sample surface. For our xy scanning needs we employ a piezo-nanopositioning stage (Physik Instrumente, P-733.2cl), which has a scan size of 100 μm × 100 μm, and is driven by a Modular Piezo Controller (Physik Instrumente E-501) (Figure 3.19).
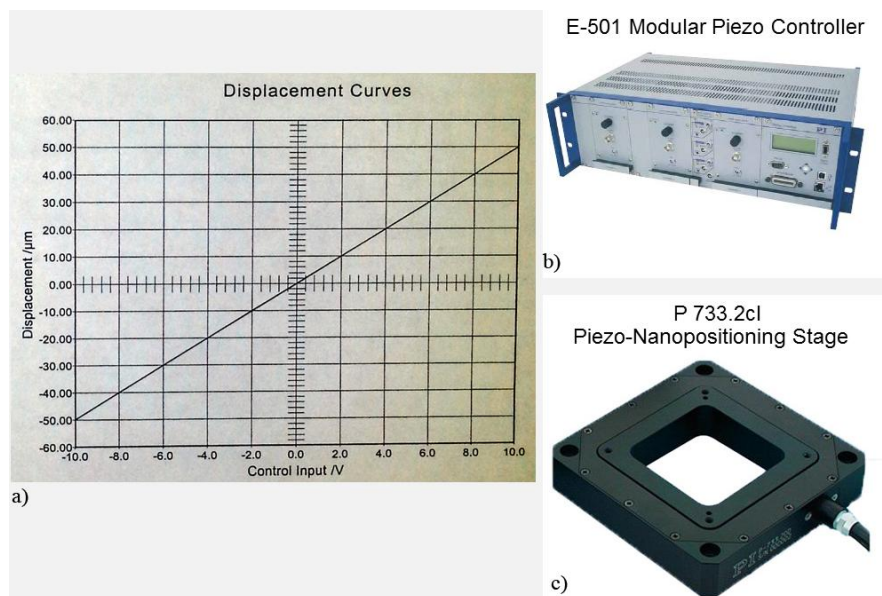
Figure 3.19 *a) Displacement curve for the xy scanner (P-733.2cl) showing a maximum scan size of 100 μm x 100 μm b) Modular piezo controller (E-501) for driving the xy scanner. c) xy scanner (P-733.2cl) is used for raster scanning the sample under investigation.*

7. Anti-vibration optical table: Since the probe is held within a few nanometers of the sample surface, very small mechanical perturbations can cause significant fluctuations of the detected signal. Therefore, the imaging system must be mechanically insulated with a device such as an anti-vibration table. Such a table

employs air cushion structures and anti-vibration feet to help dissipate energy from induced vibrations (Figure 3.20). Elimination of vibrations from the microscope also involves shielding from external air flow by a means of a curtain. The implementation of the NSOM module atop our inverted microscope along with the main optical and mechanical components are shown in Figure 3.21.
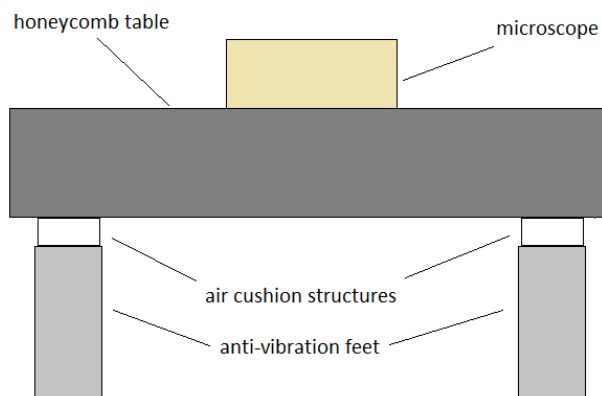
Figure 3.20 *Illustration of an air cushion honeycomb table (Bottom) NSOM module mounted on top of the platform.*
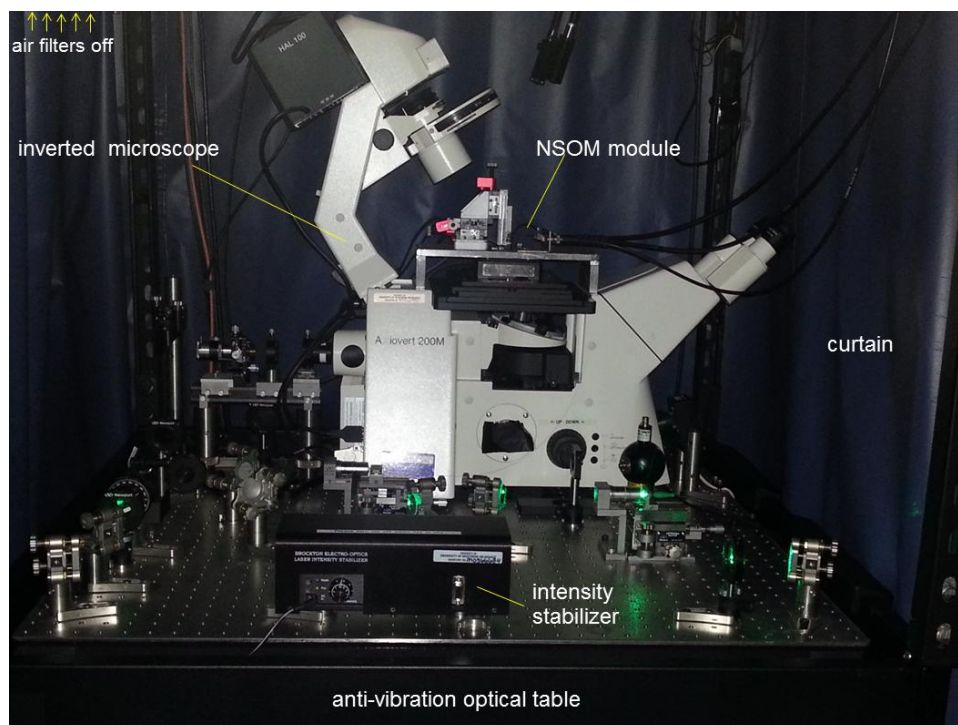
Figure 3.21 *Implementation of NSOM module atop our inverted microscope along with the main optical and mechanical components.*

3.3 Electrical Components

The electronic components include the scanning drivers for the piezoelectric z-scanner and the xy piezo-nanopositioning stage, high-speed electronics composed of a set of amplifiers associated with monitoring the oscillator's signal and a z-distance control (feedback) system, and a computer system that drives the scanners, measures data and converts the data into an image. In this section, we will discuss the main electrical components used in our experimental setup:

1. Lock-in Amplifier (Signal Recovery DSP Lock-in Amplifier, model 7265): A device used to generate the dither piezo driving signal and detect and amplify the piezoelectric signal generated from the TF oscillations to achieve signal levels up to 1 V (Figure 3.22).

2. Feedback control mechanism (RHK Technology SPM 1000 Control System). This control box has several essential functions in our setup. It is a high voltage power source (output -215 V to +215 V) that can drive our piezo scanners while providing a Proportional-Integral-Differential (PID) feedback loop that monitors the TF signal and allows for tip-sample approach and subsequent scanning (Figure 3.22).

The feedback control mechanism is shown in Figure 3.23. Please refer to this Figure when you see a blue number in the discussion below. These numbers are shown in the Figure and represent a process or a device such as a computer. The lock-in amplifier electrically drives the piezoelectric dither to vibrate at various frequencies typically within ±1000 Hz of the common TF resonance frequency of 32,768 Hz (#1). This in turn excites the mechanical resonance of the

tuning fork in such a way that the TF and attached tip are vibrated parallel to the

sample surface. A tuning fork piezoelectric signal is simultaneously measured

(#2) and plotted versus the driving frequency to construct a resonance curve (#3).

Figure 3.22 *(Top) Signal Recovery DSP Lock-in Amplifier, model 7265. (Bottom) RHK Technology SPM 1000 Control System.*
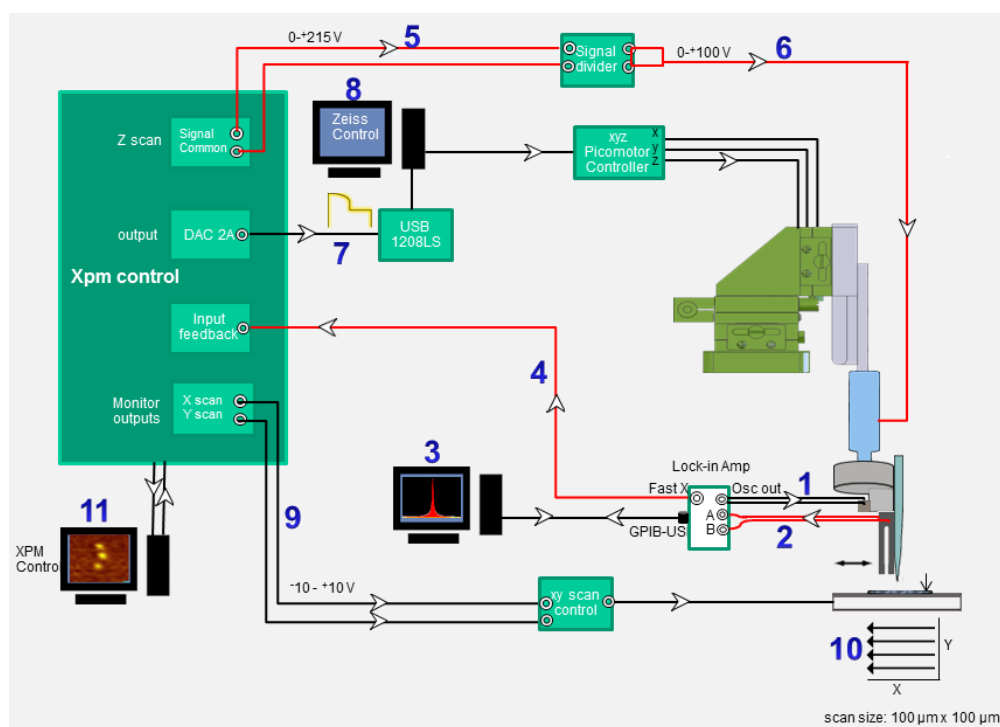
Figure 3.23 *Feedback control mechanism (not to scale)*

With the aid of a custom-developed computer software that communicates directly with the lock-in amplifier, we are able to construct a resonance curve (Data tab) and fit the curve to a Lorentzian function to obtain important parameters such as the peak frequency, FWHM, the peak amplitude and Q-factor (Analyze tab) (Figure 3.24). We can also use the software to manually set the dither amplitude such that a TF peak amplitude of 10 µV is obtained. Depending on the experimental conditions, small dither amplitudes of about 100 µV could be sufficient, whereas in other cases it could require a few volts to generate the same output. In any case, once the desired dither amplitude is found and set, it doesn't need to be changed throughout the experiment. Additionally, the software (Experiment tab) allows us to set any target oscillator amplitude (default is 10 µV) so the appropriate dither amplitude is automatically found and applied.

In preparing for a new experiment and before the probe is attached to the TF, the resonance curve for a free TF in air is obtained (Figure 3.25). In this example, the resonance is characterized by: peak frequency = 32,650 Hz, peak amplitude = 16 µV, FWHM = 8 Hz and Q-factor = 8,000. As expected, upon attachment of the fiber probe, the resonance frequency of the TF shifts to a lower value (32,130 Hz) while the peak amplitude is reduced to 10.92 µV. In addition, the FWHM increases to 15 Hz and the Q-factor drops to 2,135 (Figure 3.25). Following attachment of the fiber probe to the TF and the subsequent resonance curve construction and fitting, we can now set up the experiment, starting with accessing the "Experiment" tab of our software and setting the target amplitude to 10 µV. This will send the peak amplitude of the TF through the FastX port of the lock-in amplifier to the "input feedback" of the XPM control box (#4).
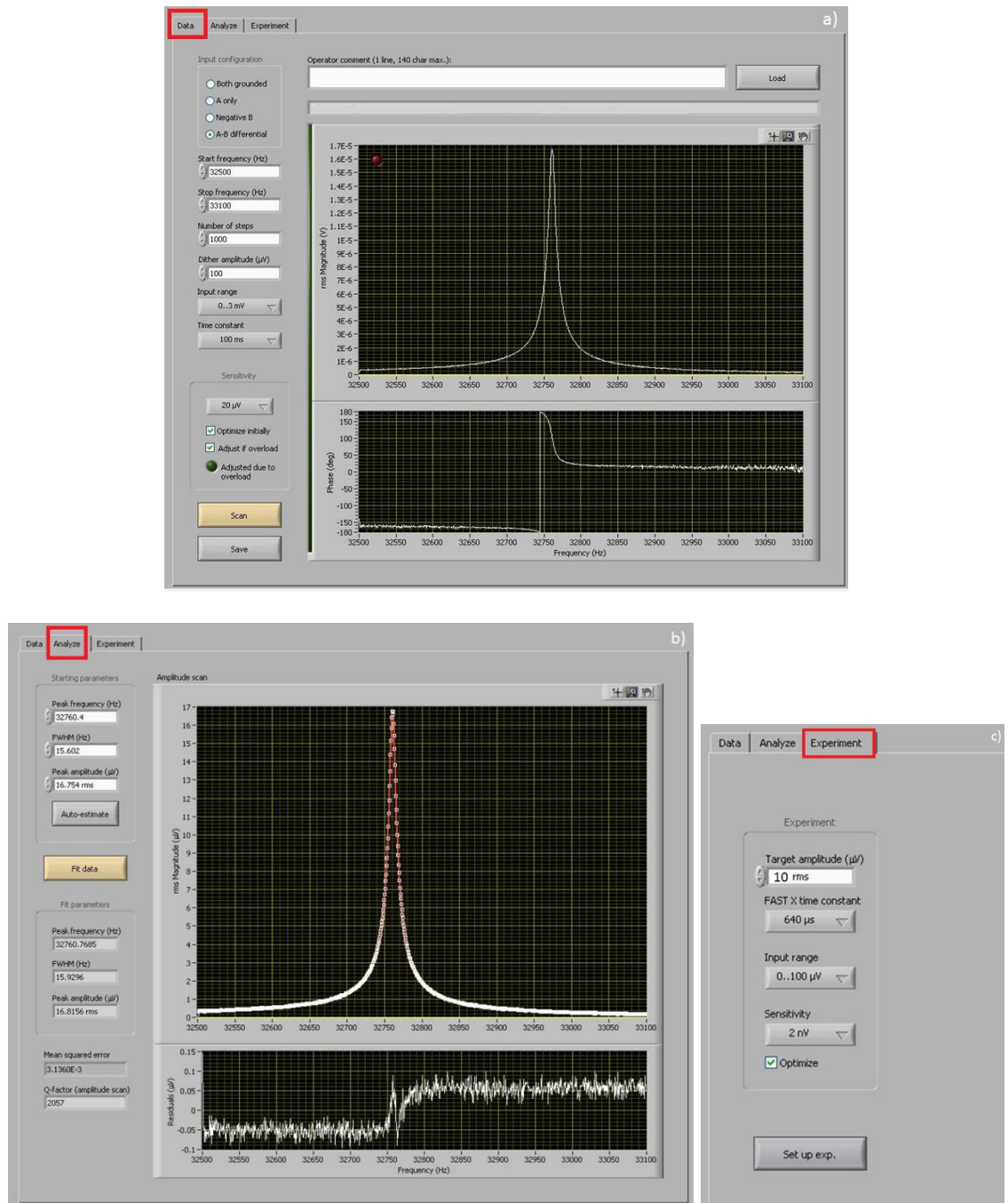
Figure 3.24 *a) Data tab of our custom-developed computer software for constructing a tuning fork resonance curve, b) Analyze tab is used for fitting the resonance curve to a Lorentzian function and obtain important parameters such as the peak frequency, FWHM, the peak amplitude and Q-factor. c) Experiment tab allows us to select a target TF peak amplitude and to set up the experiment by communicating with the lock-in amplifier which will then provide the XPM control with the TF piezoelectric signal continuously.*
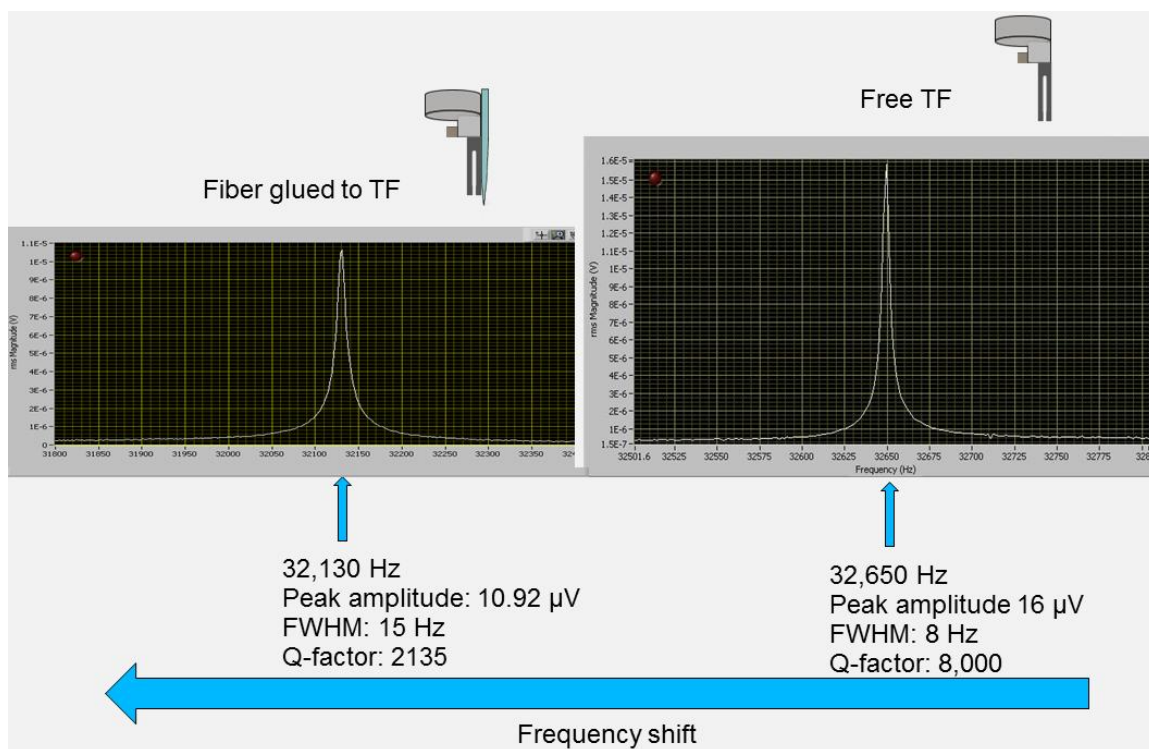
Figure 3.25 *Resonance curves for a free TF in air and a TF-fiber system.*

A typical value of the amplified TF piezoelectric signal is about 475 mV. This signal can be viewed on the front panel of the XPM control box as well as from the RHK XPM software (#11). The setpoint is typically chosen at 200 mV (42% of the peak amplitude). This means that the tip-sample approach will stop as soon as the TF signal drops to 200 mV. In addition to assigning the setpoint using the RHK XPM software (#11), other approach parameters are also configured. Our settings include:

Approach system: (Kinetic waveform). This is the approach mechanism used by the scan head.

Waveform: (Double arc). This setting specifies the waveform for kinetic approach. Double arc waveform will accelerate the motor followed by a smooth de-acceleration (Figure 3.26).

Figure 3.26 *A graphical representation of the kinetic waveform that drives the xyz Picomotor actuators.*

Approach mode: (Tip retract). This is the safest and slowest mode. The program pulls the tip back, makes a motion cycle then releases the tip and waits to see if the feedback loop stabilizes with the z position above the threshold.

Approach threshold: (-75%). The approach is continued until the control loop stabilizes above the threshold. The range is -100% to +100% where -100% is just barely within range and +100% is fully retracted z piezo. A value of 0% means that once the approach is completed, the tip will need to advance until just past the midpoint of the feedback range to reach the surface.

Approach steps: (150). During tip-sample approach, this is the number of motion cycles to perform between in-range tests. Typically, this should be the number of cycles or steps to cover ~10% of the total z-piezo range.

Feedback delay: (10.00 s). Tip-retract approach mode monitors the feedback signal until the control loop stabilizes above the threshold value. If the loop position is still above the threshold after this delay time has elapsed, the

approach is consider finished. If the tip goes below the threshold, the approach continues.

Tip-restore delay: (10.00 s). Delay time after the tip is retracted and before any coarse approach starts.

Period: (80 ms). The wait time between each kinetic wave output. The delay allows the Zeiss control center software (which intercepts the SPM1000 signals and generates the commands for moving the Picomotors) does not miss any of the signals.

After having the approach mode configured, tip-sample approach is started. Initially, the tip is manually placed at about 1 mm away from the sample surface. Fine approach begins with z-scan output voltage ramping from 0 to +215 V (#5). A custom-made signal divider steps down the voltage to (0 to +100 V) (#6). This is necessary in order match the allowed voltage range for the z-scanner (0 to +100 V). The applied z-scan voltage causes the z-scanner to extend by 15 μm while the TF amplitude is being monitored and compared to the setpoint. If the tip is out of range, the tip is retracted and kinetic wave is sent through the output (DAC 2A) of the XPM control box (#7) via a USB 1208LS interface to the Zeiss Control Center (#8) which is constantly "listening" to this wave and relaying it to the *XYZ* Picomotor Ethernet Controller, causing the z motor to take 150 steps (~30 nm each, 4.5 μm total) with feedback mechanism off. This concludes the first cycle of the tip-sample approach. Similarly, the second cycle starts with fine approach (#5, #6) in which the z-scanner is extended by 15 μm while checking for feedback (TF piezoelectric signal against the setpoint). If no feedback is detected, the tip is retracted and the coarse approach kicks in (#7) causing the z-

motor to take another 150 steps (4.5 µm) with feedback turned off. This continues until the tip gets close enough to interact with the sample surface and dampen the oscillations, causing a reduction in TF signal amplitude. When the reduced tip amplitude matches the setpoint (200 mV) and the approach threshold has been reached, the approach is finished (Figure 3.27). Under our approach parameters, it takes approximately 21 seconds for one cycle to complete. Assuming that the tip was originally 1 mm (1000 µm) away from the sample, it would take 222 cycles to reach the tip-sample interaction range (1000 µm / 4.5 µm = 222 cycles). Therefore, the approach time is calculated to be 77 minutes (222 x 21 s = 3333 s = 77 min). The functionality of Zeiss Control Center (#8) in receiving the kinetic wave signal and delivering it to the Picomotor Controller is added to many other benefits implemented in this custom-developed software. In this context, it can be used to adjust many parameters of the x, y and z Picomotors such as velocity and acceleration and can manually control the motion of the motors with increments as small as 1 step (Figure 3.28).
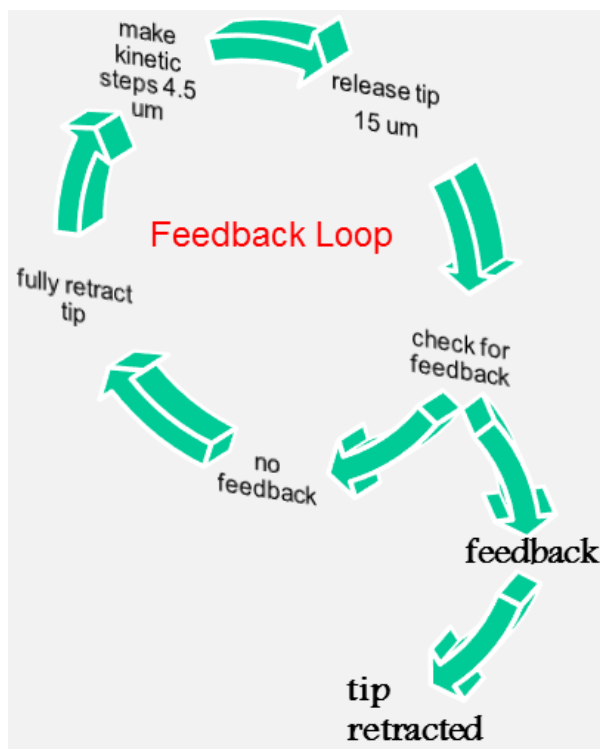
Figure 3.27 *Feedback control mechanism for the tip-sample approach.*

Figure 3.28 *Custom-developed Zeiss Control Center during approach.*

When the tip is in interaction range with the sample, raster scanning can be started. The process is initiated from the RHK XPM software (#11) where -10 to +10 V is sent through "monitor output" x-scan and y-scan of the XPM Control box (#9). The signal is picked up by the Modular Piezo Controller (E-501) and relayed to the xy Piezo-Nano positioning stage (P-733.2cl), which in turn "scans the tip" by moving the sample under the tip while the tip is fixed in x and y (#10). The feedback loop controls the z-piezo to ensure a constant distance between the tip and the sample topography while scanning. A topographical image is constructed, pixel by pixel, from the distance control information used to keep the tip-sample distance constant.

Chapter 4

Materials and Methods

4.1 Chemicals

Minor impurities, especially large sized and optically active, arising from some commercial chemical products may interfere with low levels of sample particles being investigated. Therefore, all of the solvents and reagents used to fabricate the optical fiber probes, clean the glass cover slips and prepare the samples were of high grade to ensure a minimum amount of such impurities. The following chemicals were used:

- 40 % Hydrofluoric acid (Sigma-Aldrich, #30103)

- Mercury (Fisher Scientific, #AC19348-2500)

- 95% Nitric acid (Sigma-Aldrich, #438073)

- 98% Sulfuric acid (Sigma-Aldrich, #320501)

- Silicone oil (Fisher Scientific, #S159-500)

- Toluene 99.9% (Sigma-Aldrich, #650579)

- Poly(methyl methacrylate); PMMA (Sigma-Aldrich, #182230)

- Acetone 99.5% (Alfa Aesar, #43053)

- Methanol 99.9% (Sigma-Aldrich, #154903)

- Isopropyl alcohol 99.5% (VWR, #BDH1133)

4.2 Cleaning Procedure for Glass Substrates

Square glass cover slips (25mm x 25mm, No. $1^{1/2}$) with a standard thickness of 0.16 to 0.19mm (VWR, #48366-249) were used as substrates to hold the specimen under examination. Before use, it is important that the cover slips are clean of dirt and residues which may cause unwanted outcomes during the experiments. The cleaning procedure is as follows:

1. Cover slips are loaded into a custom-made Teflon holder (Figure 4.1).
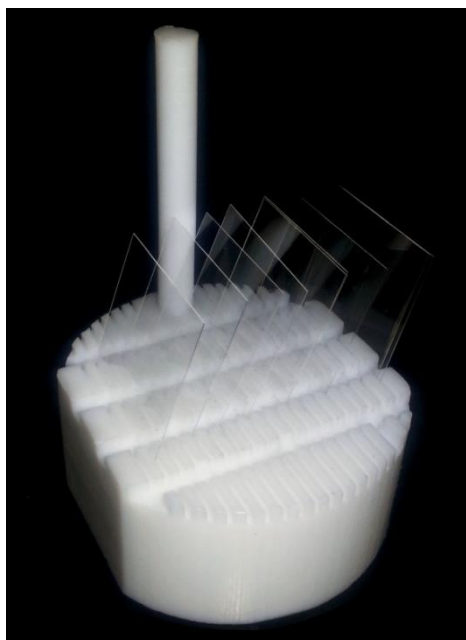
Figure 4.1 - *Glass cover slips loaded in the Teflon holder*

2. The holder is submerged in a 100 ml beaker half-filled with acetone.

3. Ultrasonic cleaner (Branson 1510) is filled with water and temperature is set to 35°C (Figure 4.2).

Figure 4.2 – *Branson 1510 ultrasonic cleaner*

4. The beaker containing the holder is submerged in the ultrasonic cleaner and sonicated at 35°C for 15 minutes.

5. The holder is then submerged in a 100 ml beaker half-filled with methanol and sonicated at 35°C for 15 minutes.

6. The holder is lastly submerged in a 100 ml beaker half-filled with Isopropyl alcohol and sonicated at 35°C for 15 minutes.

7. The cover slips are thoroughly blow dried with nitrogen gas.

8. The cover slips are then placed in a home-built ozonator, a device composed of a sealed box equipped with a UV lamp and a constant flow of oxygen gas (Figure 4.3). For about 5 minutes, the in-situ generated ozone molecules oxidize any remaining contaminants and make the surface hydrophilic. A good wetted surface is necessary when coating the coverslips with aqueous or polar solutions, as it helps

with spreading the solution evenly over the surface without the formation of droplets.
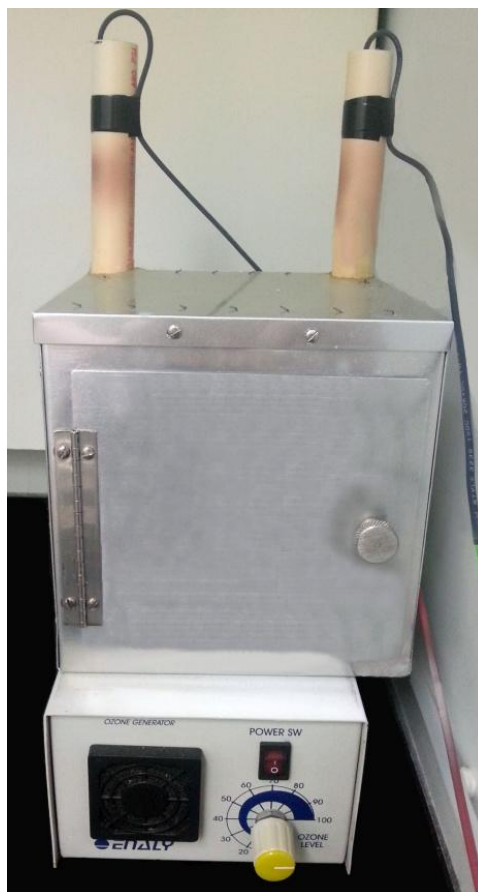
Figure 4.3 – *Home-built ozonator used in the final step of cover slip cleaning*

9. The cover slips are now ready for use or storage. Each cover slip is individually kept in a sealed black plastic box (ElectronicsUSA, #MK-51) which is wrapped with Parafilm for more sealing against moisture and air contamination.

4.3 Coating the Glass Substrates

PMMA (Figure 4.4) is known for its ability to produce uniform and transparent thin films on flat substrates. It also provides a better adhesion of the specimen

nanospheres to the glass cover slips. Therefore, it was used as the host

substrate to coat the glass cover slips prior to sample deposition.
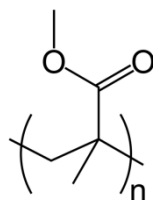
Figure 4.4 - *Schematic Structure of PMMA polymer*

PMMA (average Mw ~120,000 g/mol) is dissolved in toluene at room temperature

to form a clear solution of 4% (w/v) concentration. 50 µL of the PMMA solution is

dispensed onto a substrate cover slip loaded in a spin coater (Laurell, model WS-

400B-6NPP) (Figure 4.5). The spin coater is configured to acceleration of 5000

rpm/s, speed of 7000 rpm and duration of 120 seconds. These parameters are

found to produce PMMA layer thickness of about 20 nm[37].
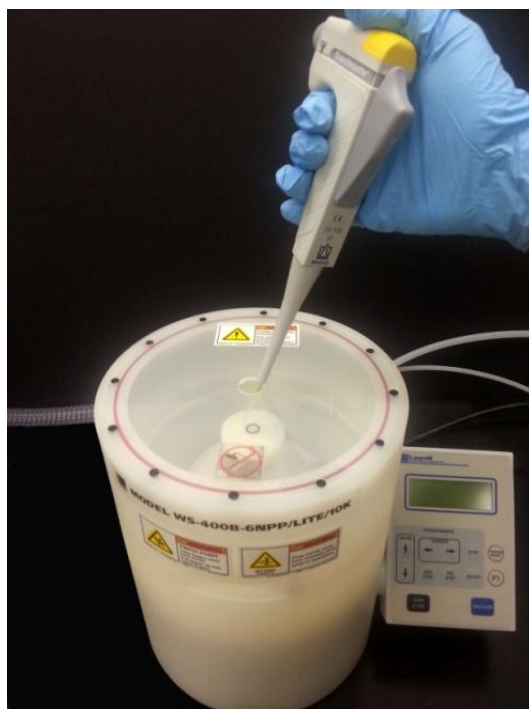
Figure 4.5 -*Dispensing PMMA solution onto the cover slip loaded in the spin coater*

4.4 Preparation of Samples

Fluorescent nanobeads (2% solids) were purchased from Invitrogen (catalog number F-8888). 10 µL of the stock nanobead (nanosphere) suspension is diluted with ultrapure water (1:10^6 v/v), then sonicated at room temperature for 20 minutes. 0.50 ml of the diluted suspension is placed on a PMMA-coated cover slip, and then placed in the refrigerator to dry out overnight.

Sample substrates of 5 nm gold nanoparticles (PELCO® Tannic NanoXact™ Gold Colloid, Tedpella # 82150-5) were prepared by diluting 5 µL of the nanogold colloid in ultrapure water (1:40,000 v/v). 0.5 ml of the diluted suspension is deposited on a cleaned glass substrate and left in the refrigerator overnight to air dry.

4.5 Fabrication of Fiber Probes

A sealed-tube chemical etching method is employed for probe fabrication. We start by cutting an optical fiber (Nufern, # S405-HP) into six 70 mm segments (Figure 4.6).
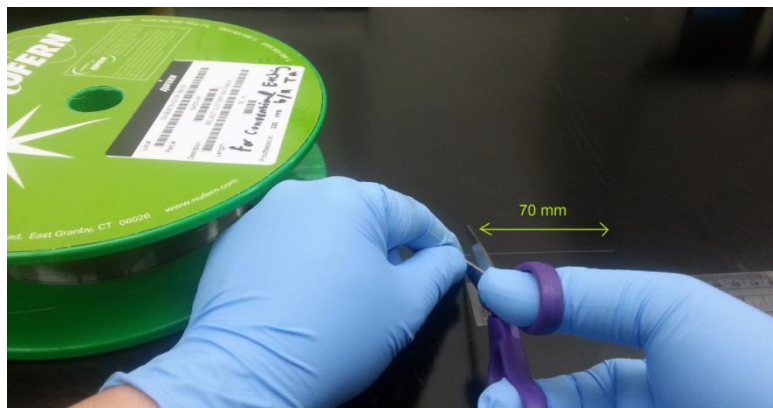
Figure 4.6 – *Cutting the fiber into segments.*

The segments are then loaded into a custom-made Teflon holder and secured in place by tightening the rectangular plates with the screws against the body of the holder. Each fiber extrudes about 45 mm out of the holder (Figure 4.7).
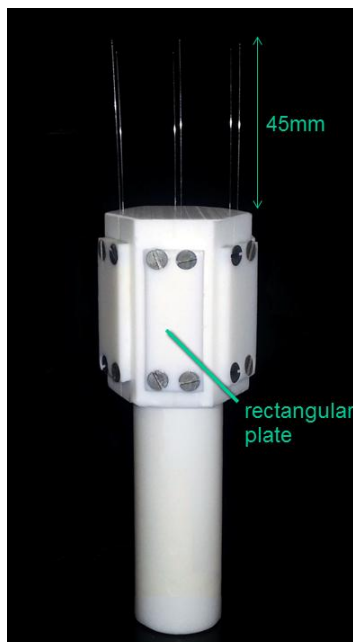
Figure 4.7 – *Fiber segments loaded into the custom-made Teflon holder.*

Next, the Teflon holder is mounted upside down into our *xy* translation stage (Arrick Robotics, Tyler, TX) (Figure 4.8). This is followed by lowering the holder into the hydrofluoric acid Teflon beaker which also contains a lower "sealing" layer of mercury and an overlayer of silicon oil to help minimize the corrosive acid vapor (Figure 4.9).
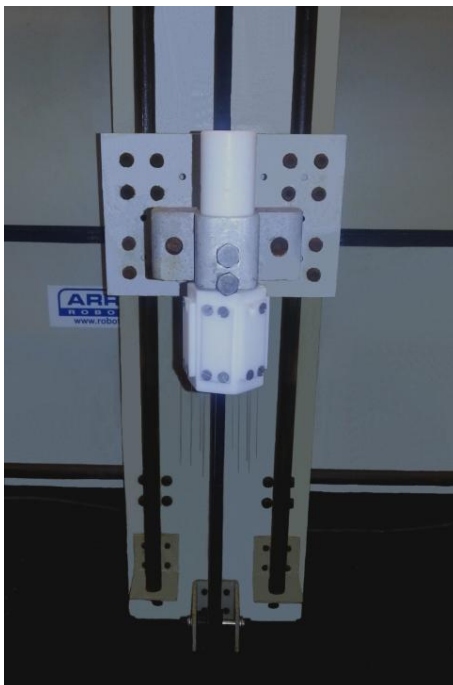
Figure 4.8 – *Teflon Fiber holder loaded into the xy translation stage.*

After three hours of etching, the fiber holder is raised from the HF beaker. As illustrated in Figure 4.10 the tips are still enclosed with the polymer coating.
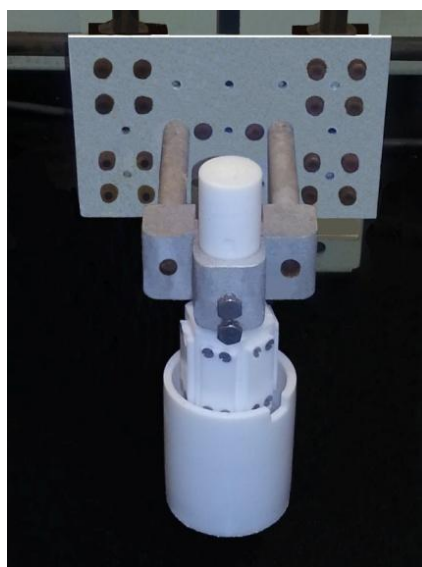
Figure 4.9 – *Teflon Fiber holder lowered into the HF beaker.*

Figure 4.10 – *Optical fibers after etching process is finished (3 hours).*

The next step involves the removal of the polymer coating by placing the etched

fibers into an acid solution (95 ml 98% H_2SO_4 and 5 ml 95% HNO_3) for two hours

at 200°C (Figure 4.11).
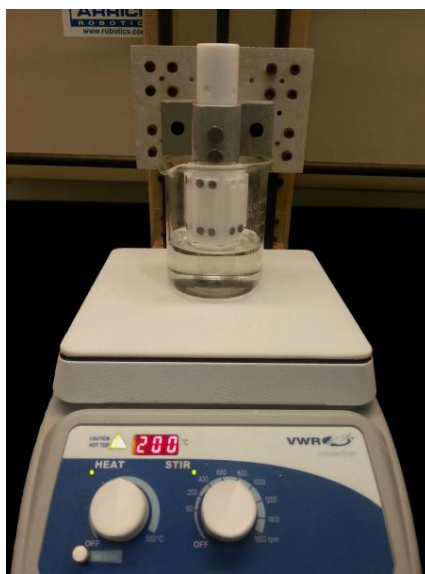
Figure 4.11 – *Removal of the polymer coating by hot acid treatment (95 ml 98% H_2SO_4 and 5 ml 95% HNO_3) for 2 hours.*

Finally, the tips are dipped in ultrapure water to quench the etching reaction and dilute any acid remaining on the fibers. The extruded fibers are shortened to approximately 15 mm after the etching process is complete (Figure 4.12).
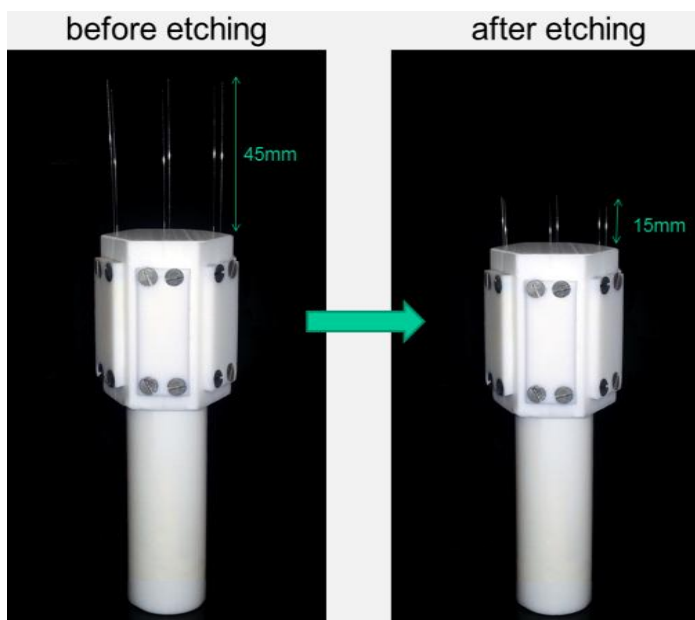
Figure 4.12 – *The extruded fibers are shortened to approximately 15 mm after the etching process is complete*

Probe characterization

Initial verification of tip formation for newly etched fibers can be conveniently performed using a stereomicroscope (Fig 4.13a). Further optical characterization with a 40x objective (XLI camera) demonstrates the sharpness of the tapered fibers (Figure 4.13b). Additionally, SEM imaging technique confirms these results and reveals tip size of < 50 nm (Figure 4.14)
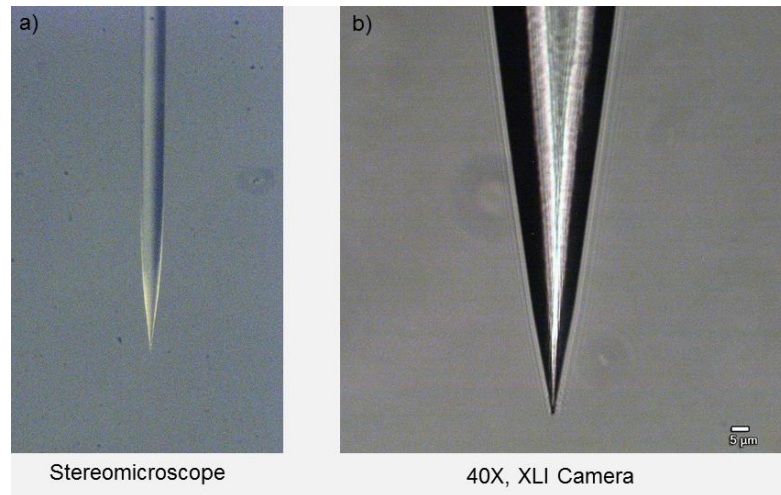
Figure 4.13 - *a) Stereomicroscope image of a fiber probe. b) Optical image of a fiber probe taken with a 40x objective (XLI camera)*
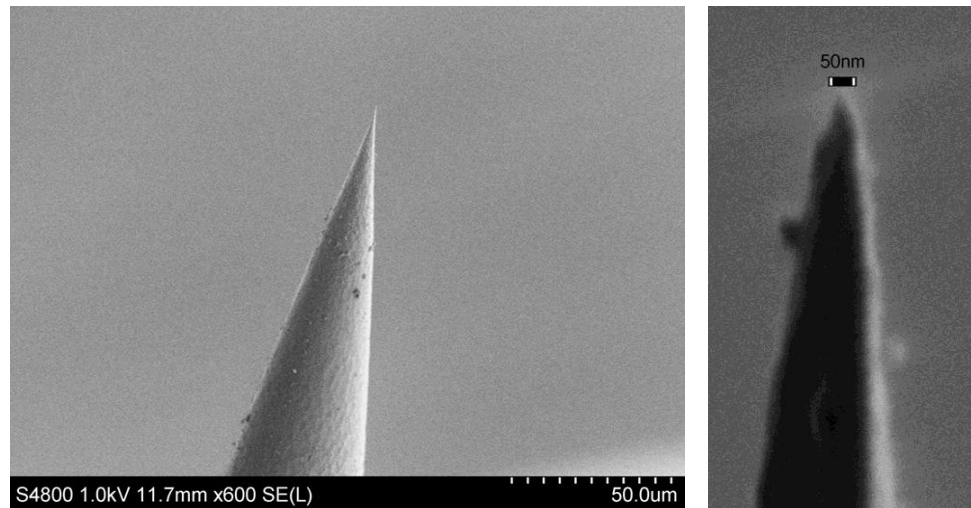
Figure 4.14 -(*Left*) *SEM image of a chemically etched optical fiber. (Right) Close up of the tip showing tip size of less than 50 nm.*

Chapter 5

Experimental Results

Out test samples can be grouped into four main categories:

1. Plane-ruled reflection gratings

2. Calibration standards

3. Nanobeads

4. Gold nanoparticles

5.1 Plane Ruled Reflection Gratings

Our first test sample is a plane-ruled reflection grating (Newport, Oriel 77300), with a $30 \times 30 \mathrm{~mm}^2$ effective area and a 300 l/mm (300 grooves/mm) line density, which equates to 3.33 µm groove spacing. These gratings are composed of grooves with sawtooth profile (blazed gratings) that exhibit 90% peak diffraction efficiency at the 2000 nm blaze wavelength (Figure 5.1). The height of the grooves is not given directly by the manufacturer, but can be determined as follows. Under Littrow configuration (incidence angle α = diffraction angle β = blaze angle θ_B), we can calculate the blaze angle θ_B for a diffraction order $m = 1$ as follows:

$$\theta_B = \sin^{-1} \frac{m\lambda}{2d}$$

where d is the line spacing (3.33 µm) and λ is the blaze wavelength (2000 nm). This leads to

$$\theta_B = \sin^{-1} \frac{1(2000 \times 10^{-9} \mathrm{~m})}{2(3.3 \times 10^{-6} \mathrm{~m})} = 17.45°$$

To determine the groove height h, we use the tangent of the blaze angle

$$\tan\theta_{B} = \frac{h}{d}$$

$$\Downarrow$$

$$\tan 17.45 = \frac{h}{3.33 \times 10^{-6} \text{ m}}$$

$$\Downarrow$$

$$0.314 = \frac{h}{3.33 \times 10^{-6} \text{ m}}$$

$$\Downarrow$$

$$h = 1.01 \text{ } \mu m$$
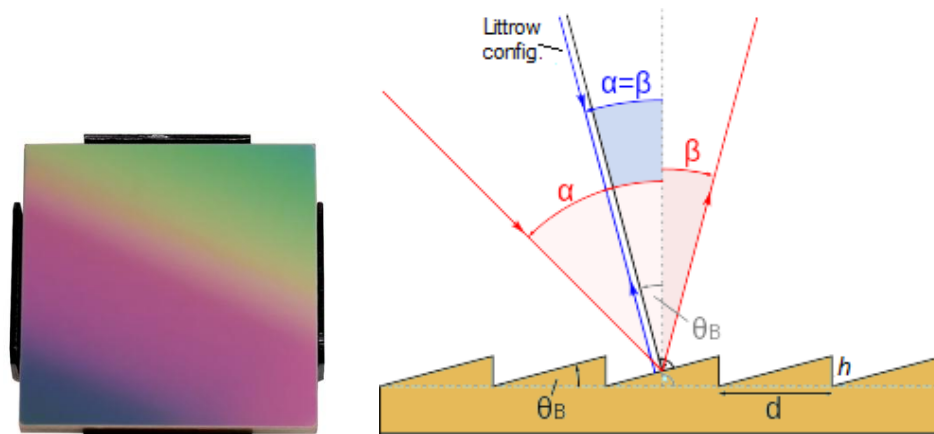
Figure 5.1 - (*Left*) *Plane-ruled reflection gratings (Newport, Oriel 77300). (Right) Diffraction at a blazed grating under the Littrow configuration.*

Figure 5.2a shows a 12×12 μm topographic image of the ruled grating acquired by raster scanning at 0.50 µm/s speed and 256 ppl (256x256 pixels). From the image line profile (Fig. 5.2b), we have determined the mean height and spacing of the gratings to 1.015 µm and 3.28 µm, respectively. These findings are

consistent with the specified and calculated dimensions of the gratings. Although these gratings are not used for *xyz* calibration purposes but rather as test structures, the results indicate that the NSOM module can be consistently used to resolve features of the same order. Additionally, to obtain high resolution images, we use the test sample to optimize the instrument operation such as the feedback loop settings for the gain and time constant and other scan parameters.
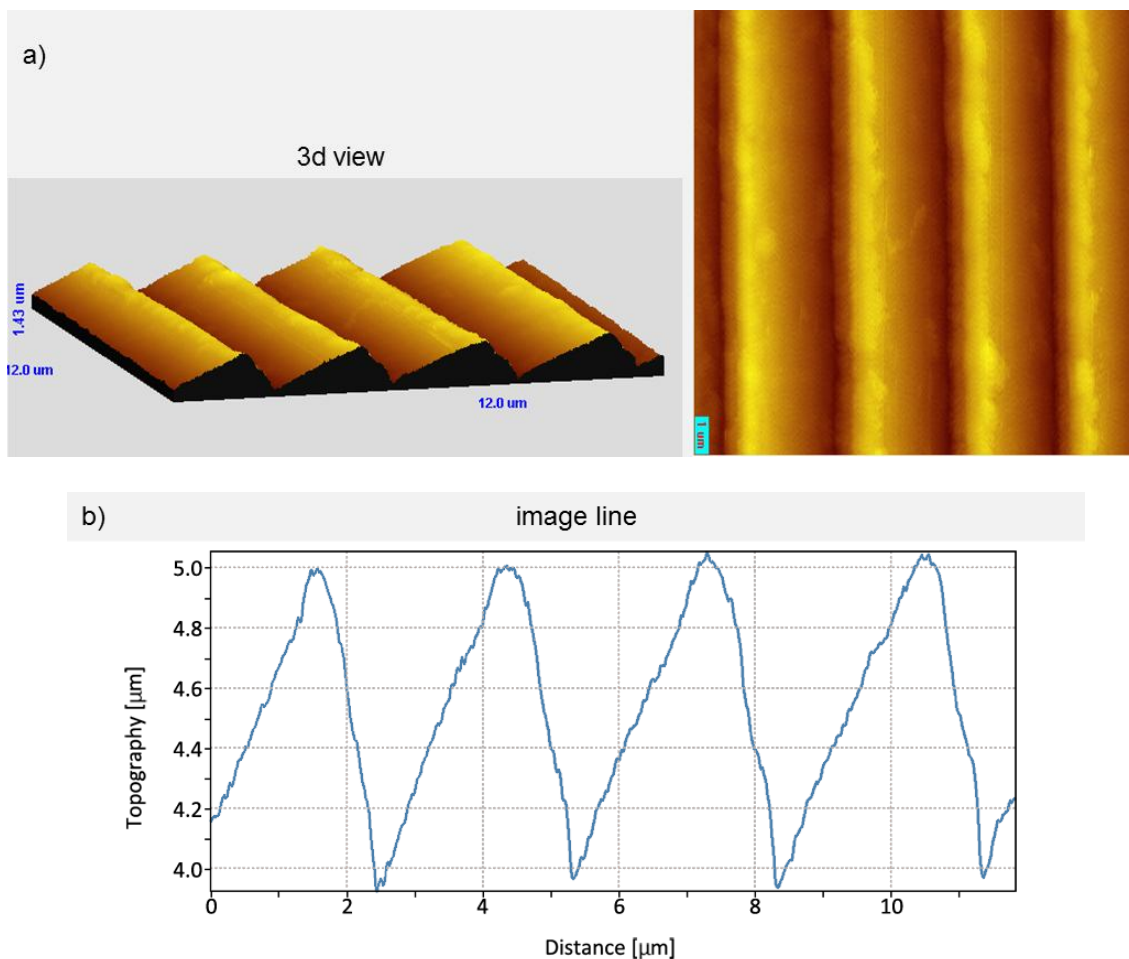
Figure 5.2 -*a) Topographic image of 300 l/mm ruled gratings acquired by raster scanning at 0.50 µm/s speed and 256 ppl. b) Image line profile of the topographic image shown in a).*

To further assess and optimize the experimental setup, we sought to perform topographic imaging of more dense gratings at 1200 l/mm (0.83 µm/groove) and

80 nm height (Newport, # 05RG1200-200-1). These plane ruled reflection

gratings cover 12.5×12.5 mm of sample area and have characteristic blaze

wavelength of 200 nm and 7.0° blaze angle. Figure 5.3a shows a topographic

image (6×6 µm, 1 µm/s) of this sample, clearly revealing the blazed gratings.

Quantification measurements of the average groove height and line spacing from

the profile of the cross-sections are found to be 80.6 nm and 0.84 µm,

respectively (Figure 5.3b). These results are noticeably comparable to the

reported specifications of the gratings, indicating that the NSOM module

topographic imaging has been conducted successfully and opening the door for

further nanostructure investigation of other samples and materials.
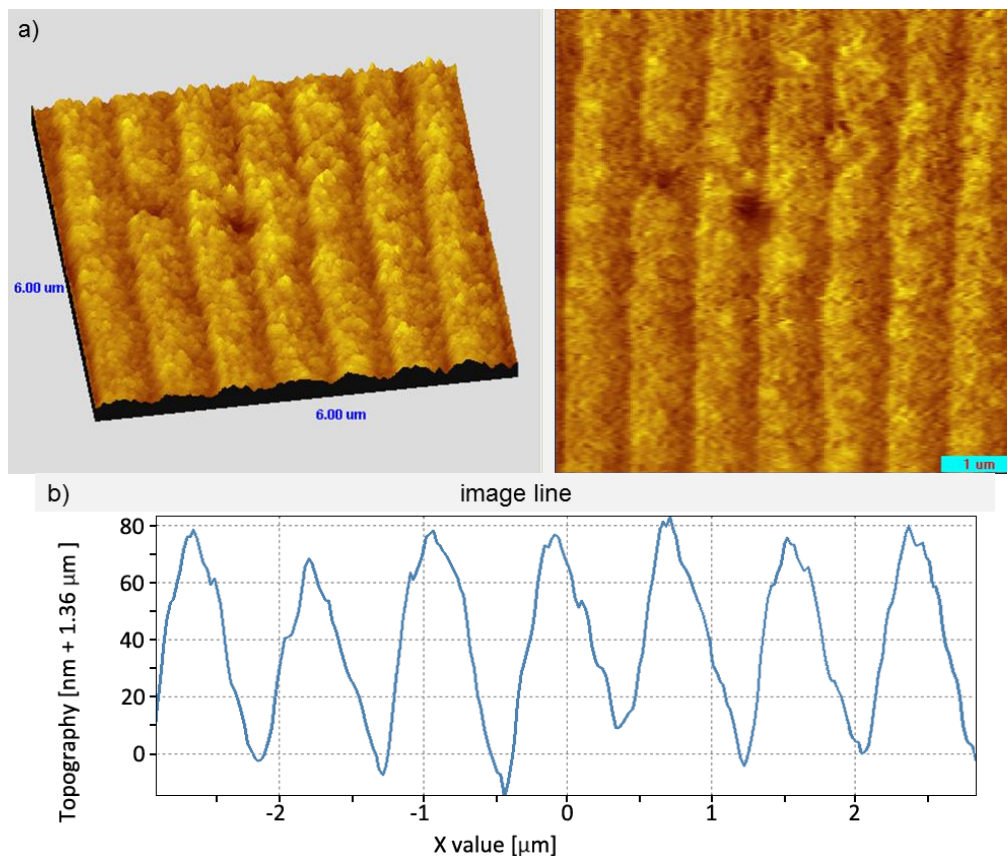
Figure 5.3 -*a) Topographic image of 1200 l/m ruled gratings b) Height profile of cross sections of the ruled reflection grating shown in a).*

5.2 Calibration Standards

Silicon is widely used as a substrate for calibrating specimens to be examined in scanning probe microscopy. Calibration standards are used as test structures for lateral (XY) and verical (Z) calibration of SPM scanners and assessment of tip sharpness.

XY-Lateral Standards

We utilized etched silicon xyz gratings (5×5 mm) purchased from Nanoscience (# 32400), which allow for lateral calibration of the piezo-nanopositioning stage (Physik Instrumente, P-733.2cl). These SPM calibration grids feature a chessboard-like structure consisting of a 2 µm square pattern with a 4 µm period, with step height in the range of 25 nm (Figure 5.4).
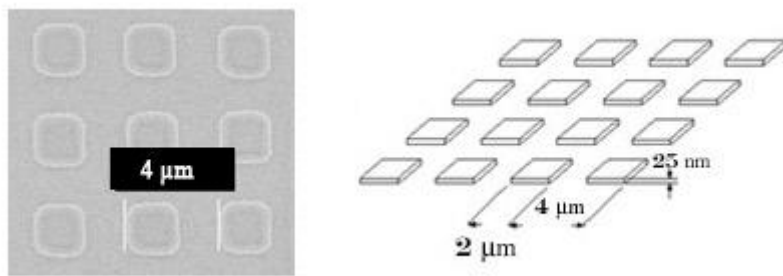
Figure 5.4 – *Silicon xyz calibration gratings (Nanoscience, # 32400) with 4 µm pitch and 2 µm mesas)*[38].

Raster scanning of a 20×20 µm sample area was conducted at 200 mV setpoint (43% of the TF peak amplitude), 1 µm/s scan rate and 512 ppl. These parameters are suitable for high resolution topographic imaging. On the other hand, image acquisition time is relatively long ($\sim$ 12 hours) for large fields of view (20×20 µm) at slow scan rates (1 µm/s). Consequently, there is always a trade-off between

image resolution and acquisition time. Figure 5.5a shows a topographic image of the *xy* calibration grid and quantitative measurements of the average pitch along each series. As shown in Figure 5.5a, the overall length of the four periods in the first series is 15.9548 µm, which equates to an average pitch of 3.9887 µm. Similarly, the average pitch for the remaining series is determined and an overall average pitch of 4.0113 µm is obtained, which is consistent with the reported specification of the grid. This result confirms the calibration of the *xy* piezo-nanopositioning stage. The average mesas' height profile of the *xyz* calibration grid is shown in Figure 5.5b

Figure 5.5 -*a) Topographic image of the silicon xy calibration grids (Nanoscience, # 32400). b) Height profile of the calibration grid shown in a).*

Although the step height (~25 nm) is not intended for vertical calibration purposes, the ability to resolve features in this height range is a promising result that drives us towards exploring further scanning capabilities of the NSOM module.
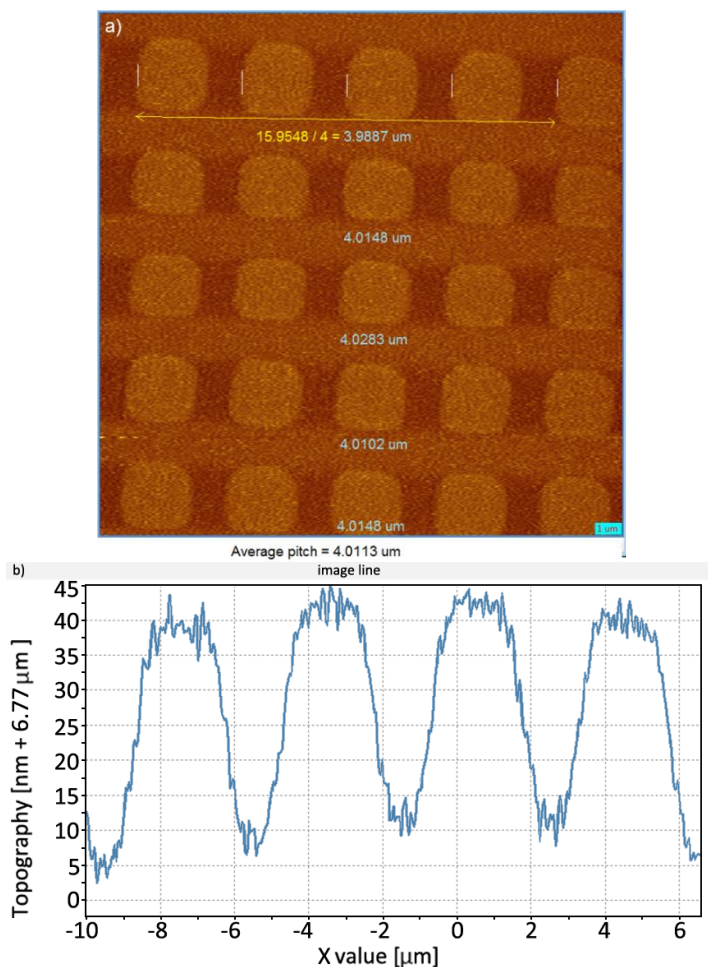
Additional verification of the *xy* scanner's precision positioning capability is carried out employing silicon gratings (Agar Scientific, # TGX01) which comprise a chessboard-like array of square pillars with sharp undercut edges. The grating has an active area of 3×3 mm and a calibrated period of 3 μm at ± 5 nm pitch accuracy (Figure 5.6).
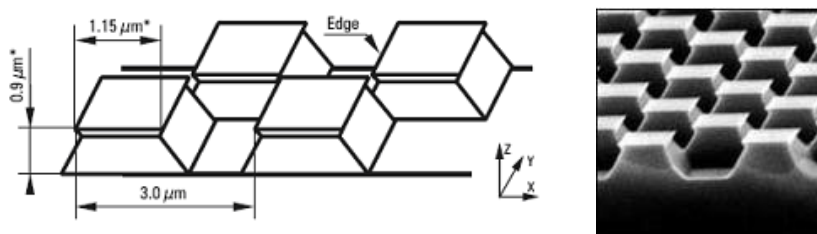
Figure 5.6 – *Silicon calibration gratings (Agar Scientific, # TGX01) with 3 μm (± 5 nm) calibrated pitch*[39]. (*The dimensions marked * are given for information only, not for calibration purposes*).

High-resolution topographic imaging was performed under these parameters: 0.5 μm/s scan speed, 43% setpoint, 10×10 μm scan area and 512 ppl. The result is shown in Figure 5.7. Examination of the image line reveals an overall width of 6.00897 μm over two periods, which equates to an average pitch of 3.00449 μm. This result is a further confirmation of the consistency of the scanning system in general, and the calibration of the *xy* piezo-nanopositioning stage in particular. Subsequently, our next action involves the calibration of the *z*-piezo scanner.
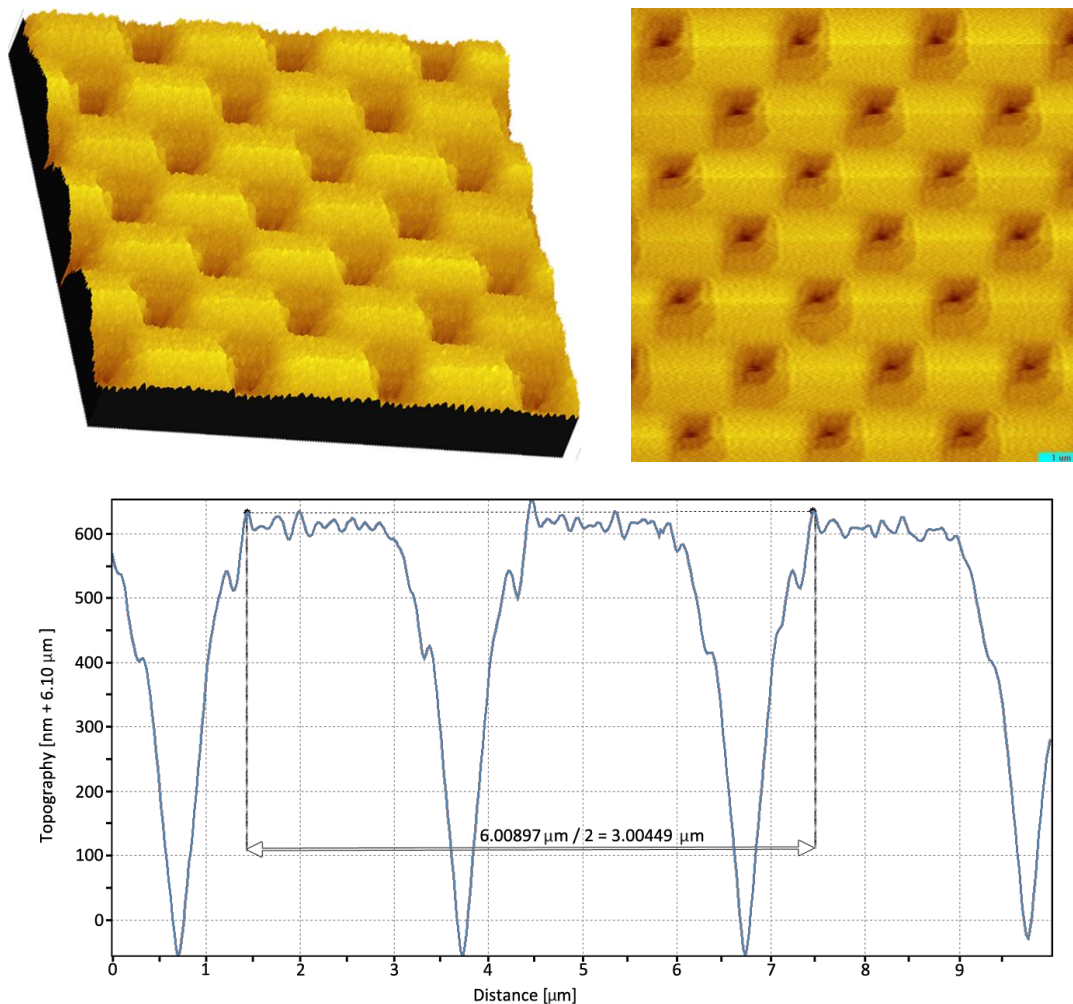
Figure 5.7 – *(Top) 10x10 µm topographic image of the silicon TGX01 calibration gratings (Agar Scientific). (Bottom) Image line of the calibration gratings shown in a).*

Z-Vertical Standard

For calibration purposes of our *z*-piezo scanner, we employed a silicon gratings substrate purchased from Agar Scientific (# TGZ11). These silicon gratings comprise a one-dimensional array of rectangular SiO_2 steps on a silicon wafer with an active area of 3×3 mm, 10 µm pitch and a calibrated height value of 1350±30 nm (Figure 5.8).
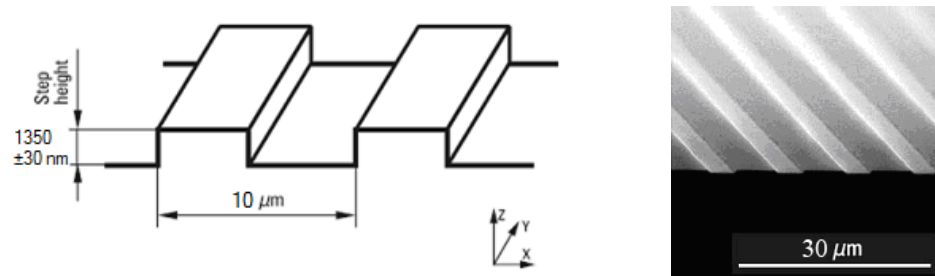
Figure 5.8 – *Silicon calibration gratings (Agar Scientific, # TGZ11) with 10 µm pitch and 1350±30 nm step height)*[40].

Image acquisition of a 50×50 µm sample at 1 µm/s speed and 512 ppl results in the topographic image displayed in Figure 5.9a. Focusing on the area indicated by the square inset yields the image shown in Figure 5.9b. Upon optimization of the z linear motion per piezo volt, the height profile of the grating steps is calibrated to an average value of 1350 nm (Figure 5.9b-left).

These height-calibrated gratings could also be utilized to determine the attainable scan resolution by assessing the noise level of the scanning system. This is conducted by scanning a flat area on the top surface of a rectangular mesa (Figure 5.10-right). The image line (Figure 5.10-left) suggests a noise level of < 3 nm, which could be attributed to undamped mechanical vibrations and to external electrical interferences (for example by electromagnetic radiation) that could cause fluctuations in the electrical signals.
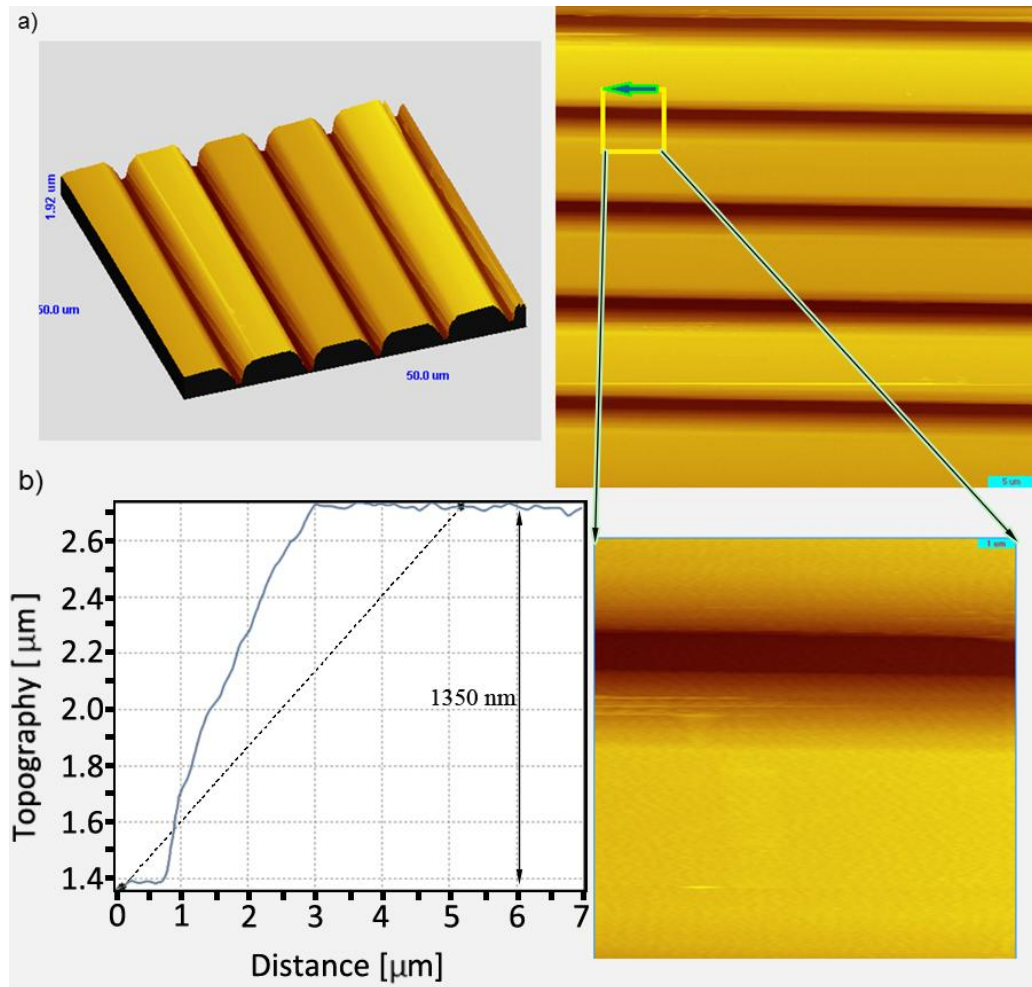
Figure 5.9 - a) Topographic image (50x50 µm) of the silicon z calibration gratings (Agar Scientific # TGZ11). b) Height profile of the calibration gratings shown in a).
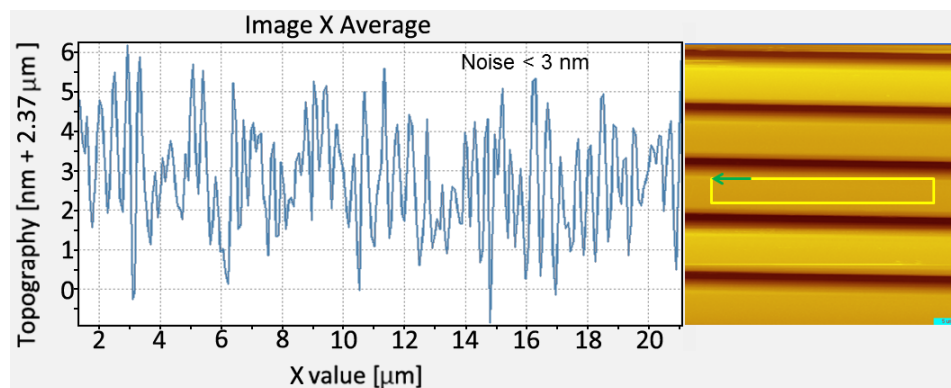
Figure 5.10 -(Right) Scanning the flat area shown on the top surface of a rectangular mesa. (Left) The resulting image line suggests noise level of < 3 nm.

5.3 Nanobeads

In this section, we'll discuss the experimental results obtained from imaging nanobeads immobilized on PMMA-coated glass substrates. PMMA is used to achieve a better adhesion of the nanospheres to the glass cover slips.

<u>1 μm Nanobeads</u>

Prior to first use, the PMMA-coated substrates with deposited nanobeads are observed under a SEM. This is performed to verify an even spreading of the transparent PMMA layer over the surface of glass cover slip (Figure 5.11).
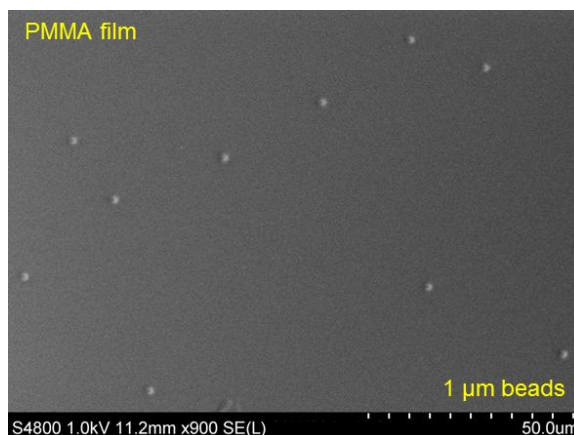
Figure 5.11 – *SEM image of 1 μm beads deposited on a PMMA layer*

Next, the nanobead substrate is loaded into the NSOM module (specifically the *xy* piezo stage) atop of our inverted microscope, and viewed under the normal imaging modes such as wide-field microscopy (Figure 5.12). This is performed to observe and locate a target area in the sample for conducting the tip-sample approach and subsequent scanning experiments.
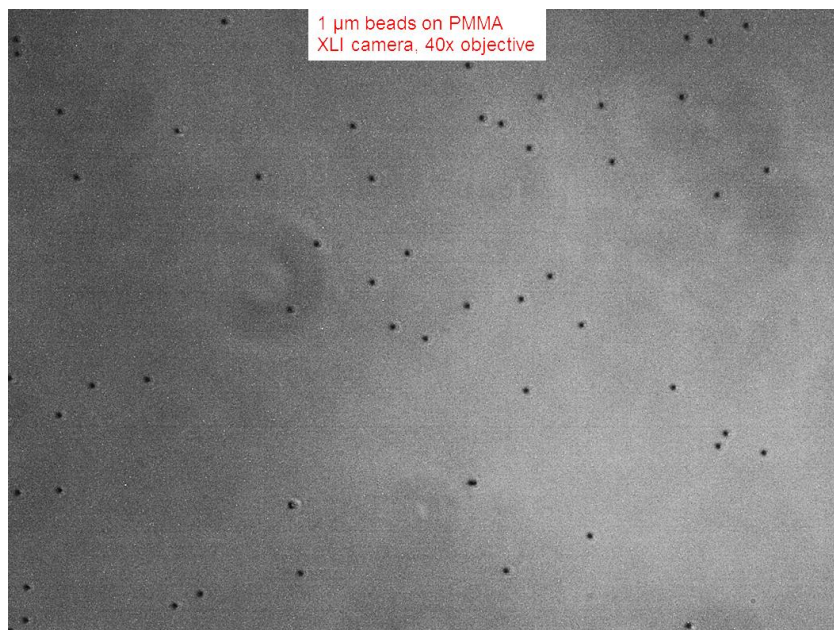
Figure 5.12 – *Typical wide-field microscopy of 1 µm beads deposited on a PMMA layer (40x, XLI camera).*

Following a successful tip-sample approach, raster scanning at 1 µm/s rate and

256 ppl is carried out to generate the topographic image displayed in Figure

5.13a. We can also take advantage of the positioning of the NSOM module on

top of an inverted microscope by recording a wide-field optical image in real time

and comparing it side-by-side to the topographic image (Figure 5.13b). It is clear

from the comparison that all the nanobeads scanned by the NSOM module can

be accounted for in the corresponding optical image. Analysis of the image line

shown in Figure 5.13c reveals that the height is in the range of 1 µm whereas the

width is in the 3 µm range. This could be explained by the soft nature of the

PMMA polymer which could cause some material to be picked up by the tip

during the scan, enlarging the tip size and thus lowering the lateral resolution.

a)

b)

c)
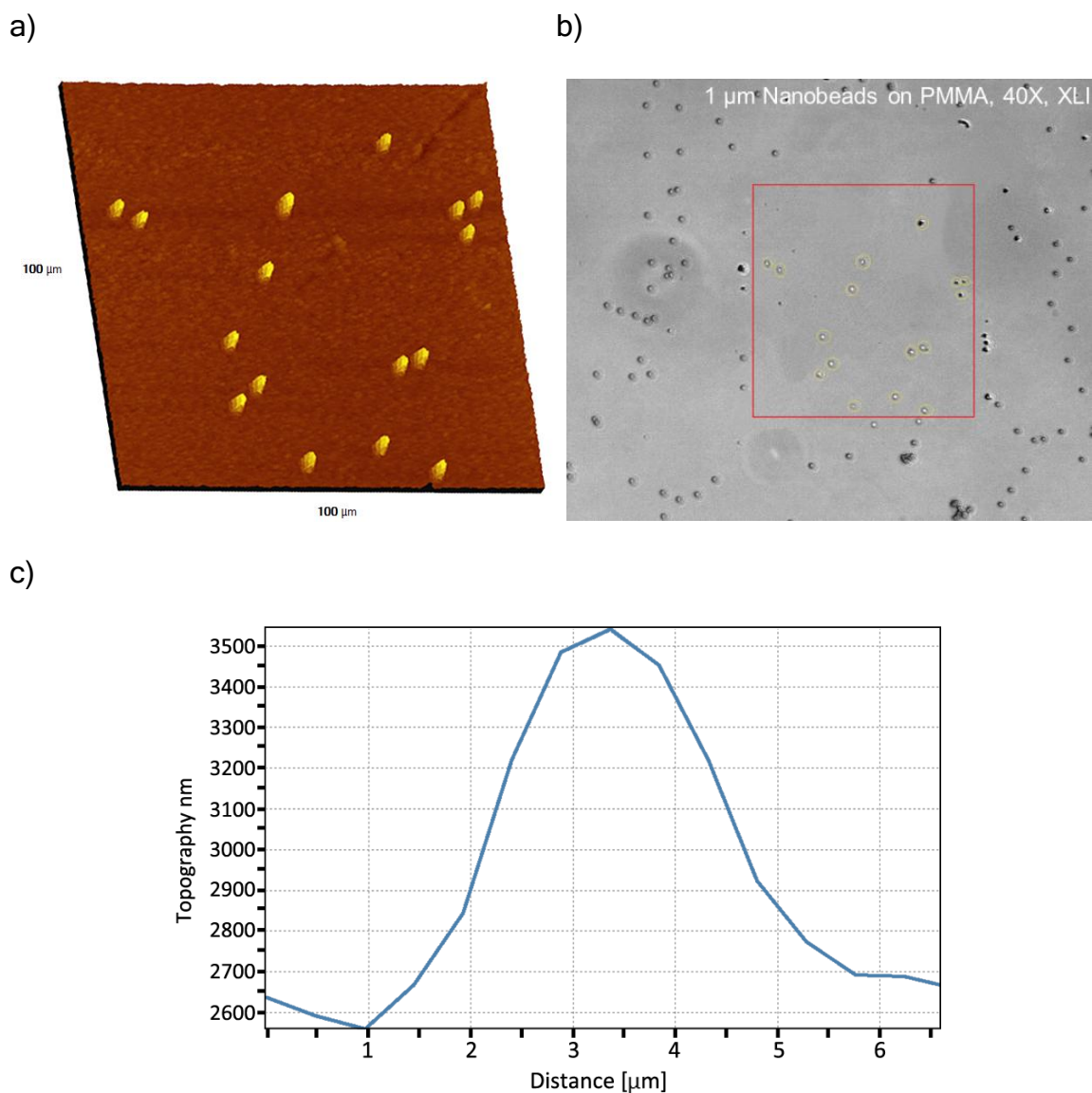
Figure 5.13 - *a) Topographic image (100x100 µm) of 1 µm nanobeads deposited on PMMA-coated glass cover slip. b) Wide-field optical image showing the raster scan area (the red square) and the imaged nanobeads. c) Typical image line of a 1 µm bead shown in part a.*

20 nm Nanobeads

After imaging relatively large nanobeads at 1 µm, we elected our next sample to be of the smallest sizes available at 20 nm. In doing so, we eliminate the need to image all the intermediate nanobead sizes such as 500 nm and 200 nm.

In a similar manner to the 1 µm experiment, we concurrently obtained both optical image of the target area and the corresponding topographic image (Figure 5.14a, b). Upon focusing on the area containing the five nanobeads, and acquiring image under 1 µm/s speed, 22% setpoint and 512 ppl, a high-resolution topographic image is obtained (Figure 5.14c). Typical cross section of a 20 nm bead is shown in Figure 5.14d.
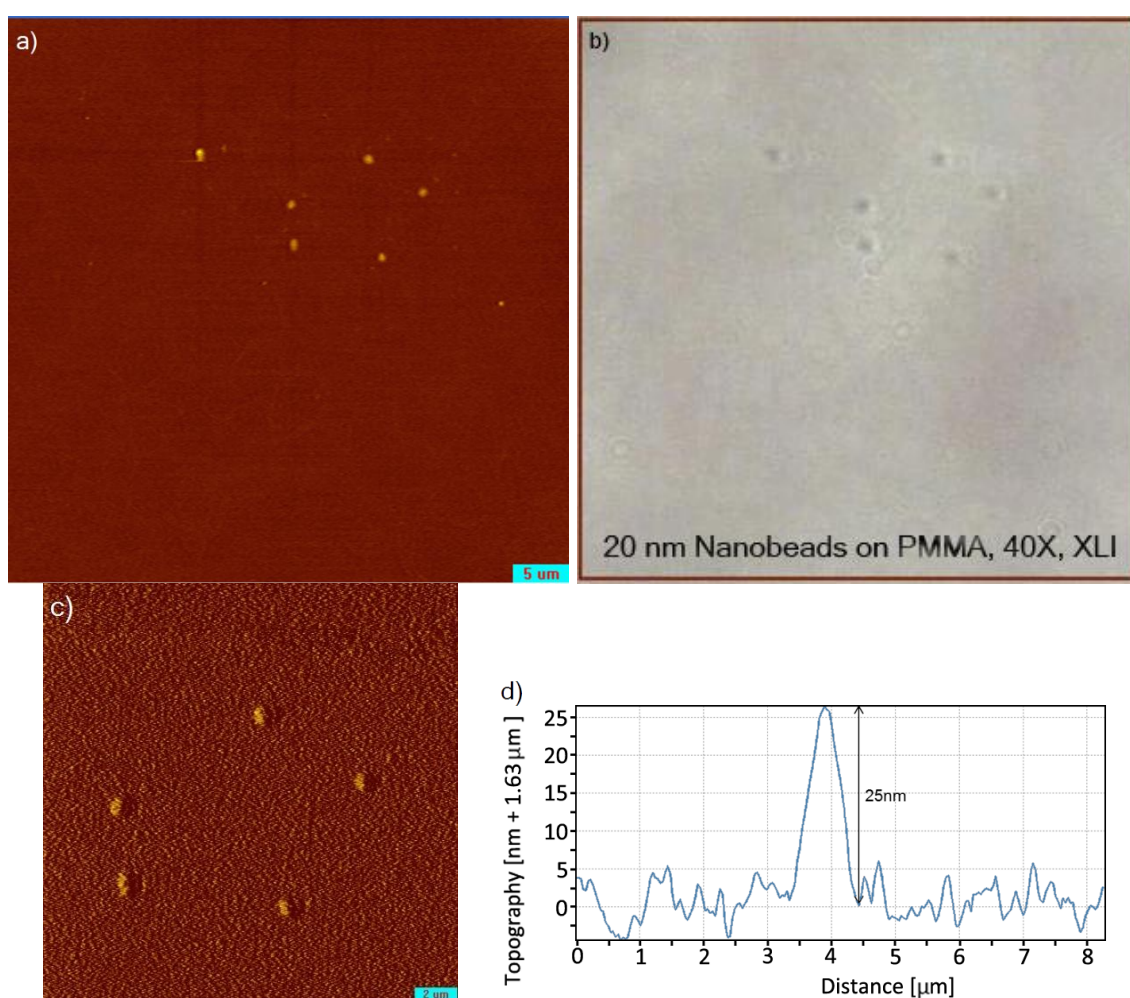
Figure 5.14 – a) Topographic image (50x50 µm) of 20 nm nanobeads deposited on PMMA-coated glass cover slip. b) Wide-field optical image showing the raster scan area and the corresponding imaged nanobeads.
c) Topographic image (20x20 µm) of 20 nm nanobeads. d) Typical image line of a 20 nm bead.

Simultaneous Fluorescence-Topographic Imaging

In this experiment, we demonstrate the NSOM module's capability of simultaneous measurements of force and optical signal by the acquisition of topographic and fluorescence images of 20 nm nanobeads. At first, we use the normal modes of the inverted microscope to locate one or two beads by wide-field optical imaging (Figure 5.15-left), followed by wide-field fluorescence imaging (Figure 5.15-right). This is done to verify the fluorescence activity of the nanobeads prior to operating the NSOM module. Following a successful tip-sample approach, laser light (514 nm) is coupled into the scanning probe (a tapered optical fiber), and a topographic image of a 20 nm bead is acquired (Figure 5.16a). Simultaneously, the optical signal (fluorescence) is recorded by a Cascade camera when the tip is in close range to the nanobead in the xy plane. This provides a direct correlation between the topographic image and the optical properties of the specimen. Subsequently, the illumination radius of the light spot is determined to be 1.8 µm by comparing the lateral position of the bead at the initial detected fluorescence signal to the position at the final detected signal (Figure 5.16b) as the tip is scanned over the nanobead.

Wide Field Microscopy

Fluorescence Microscopy

20 nm beads, XLI, 40X, HAL

20 nm beads, Cascade, 40X, Ar⁺
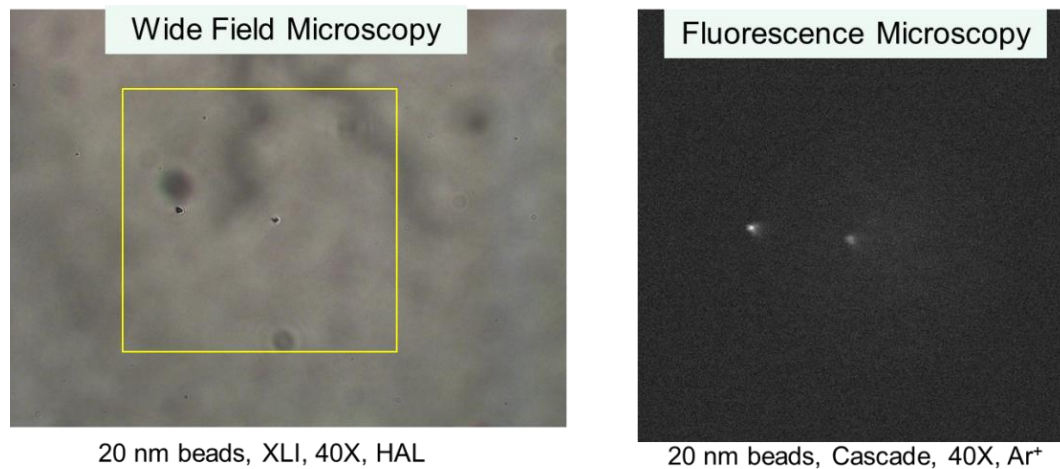
Figure 5.15 – *(Left) Wide-field optical microscopy image of 20 nm beads deposited on a PMMA layer (40x, XLI camera). (Right) Wide-field fluorescence image of the nanobeads shown on the left.*

a)
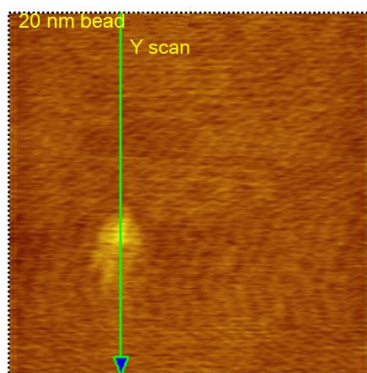
b)
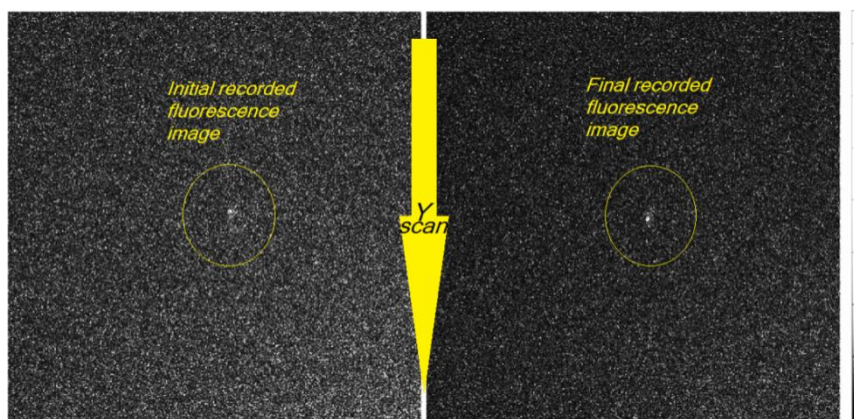
Figure 5.16 – *a) Topographic image of a 20 nm nanobead deposited on PMMA-coated glass cover slip. (b, left) Initial recorded fluorescence image of the nanobead. (b, right) Final recorded fluorescence image of the nanobead.*

5.4 Gold Nanoparticles

In this experiment we push the resolution limit of the NOSM module by attempting topographic imaging of 5 nm gold nanoparticles (Tedpella, # 82150-5). Figure 5.17 shows a TEM image of the NPs and their size distribution.
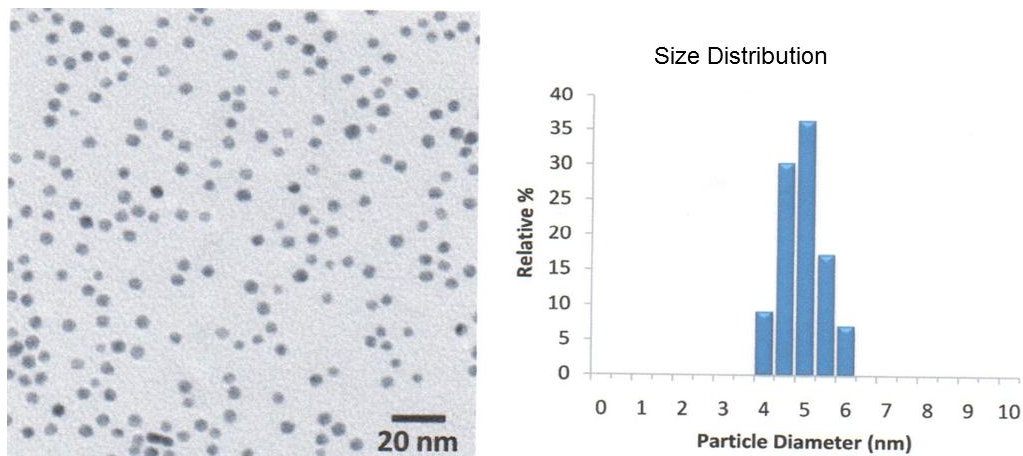
Figure 5.17 – *(Left) TEM image of 5 nm gold nanoparticles (Tedpella # 82150-5). (Right) Size distribution of the gold nanoparticles*[41]

Raster scanning was conducted at 1 µm/s rate, 42% setpoint and 512 ppl. In order to verify detected nano-features, both forward and reserve topographic data were recorded. Figure 5.18a displays the topographic image resulted from the revere scan (left) and the corresponding output from the forward scan (right). It is clear that we are able to utilize the NOSM module to resolve 5 nm gold nanoparticles. This is confirmed from the analysis of the image line which reveals a height range of 5-5.4 nm (Figure 5.18b).

a)
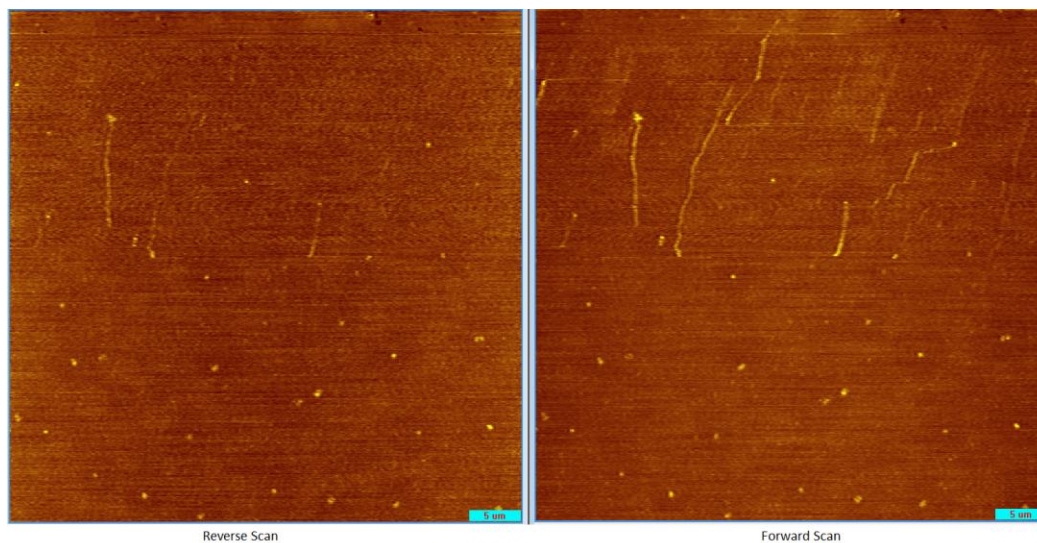
b)
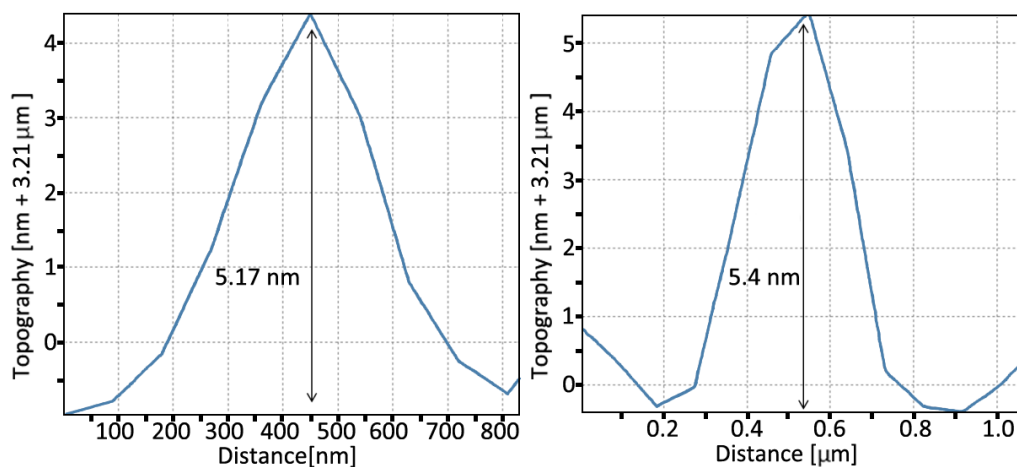
Figure 5.18 - *a) Topographic image resulted from the revere scan (left) and the corresponding output from the forward scan (right).*
b) Typical Image line profile of 5 nm gold nanoparticles.

Noise Level

The noise level of the scanning system was determined by scanning a flat area of the PMMA polymer substrate. The image line (Figure 5.19) suggests a noise level of < 2 nm.
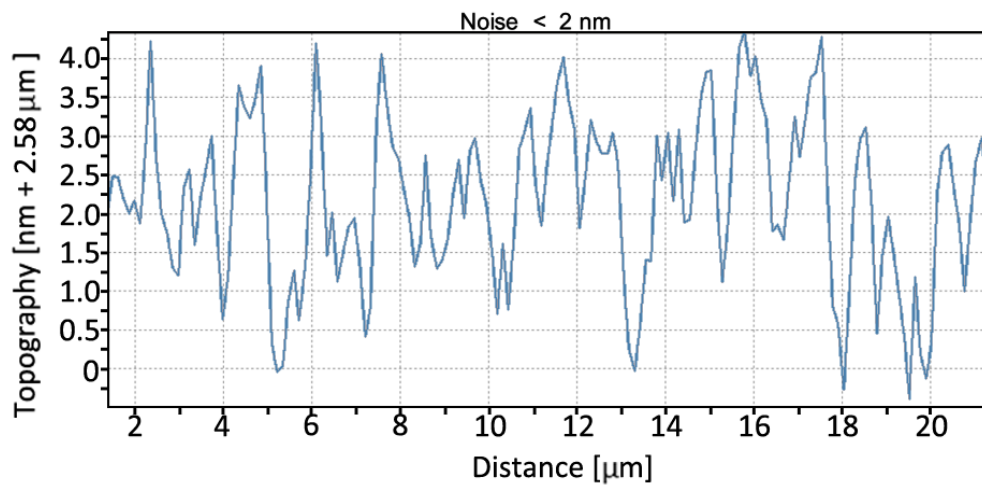
Figure 5.19 –*The resulting image line suggests noise level of < 2 nm.*

5.5 Nanometer-Scale Surface Modification

The probe tip of a scanning probe microscope (SPM) can be utilized to perform mechanical modifications on a sample surface. Scratching for example is the process in which the probe tip is used to displace weakly adsorbed particles of a polymer layer substrate. By adjusting the feedback loop parameters to scan acquisitions that require high tip-sample interaction forces, we can deliberately drive the tip to physically interact with the sample surface and cause surface modifications. Figure 5.20 shows the outcome of the mechanical lithography in which *x* and *y* line scans were carried out repeatedly over a period of time (30-60 minutes). Analysis of the image line cross sections shows that the mechanically engraved grooves have a depth of 40-60 nm and a width of 300-350 nm. Confirmation of these grooves has been conducted by using SEM and wide-field optical microscopy. These results are shown in Figure 5.21.
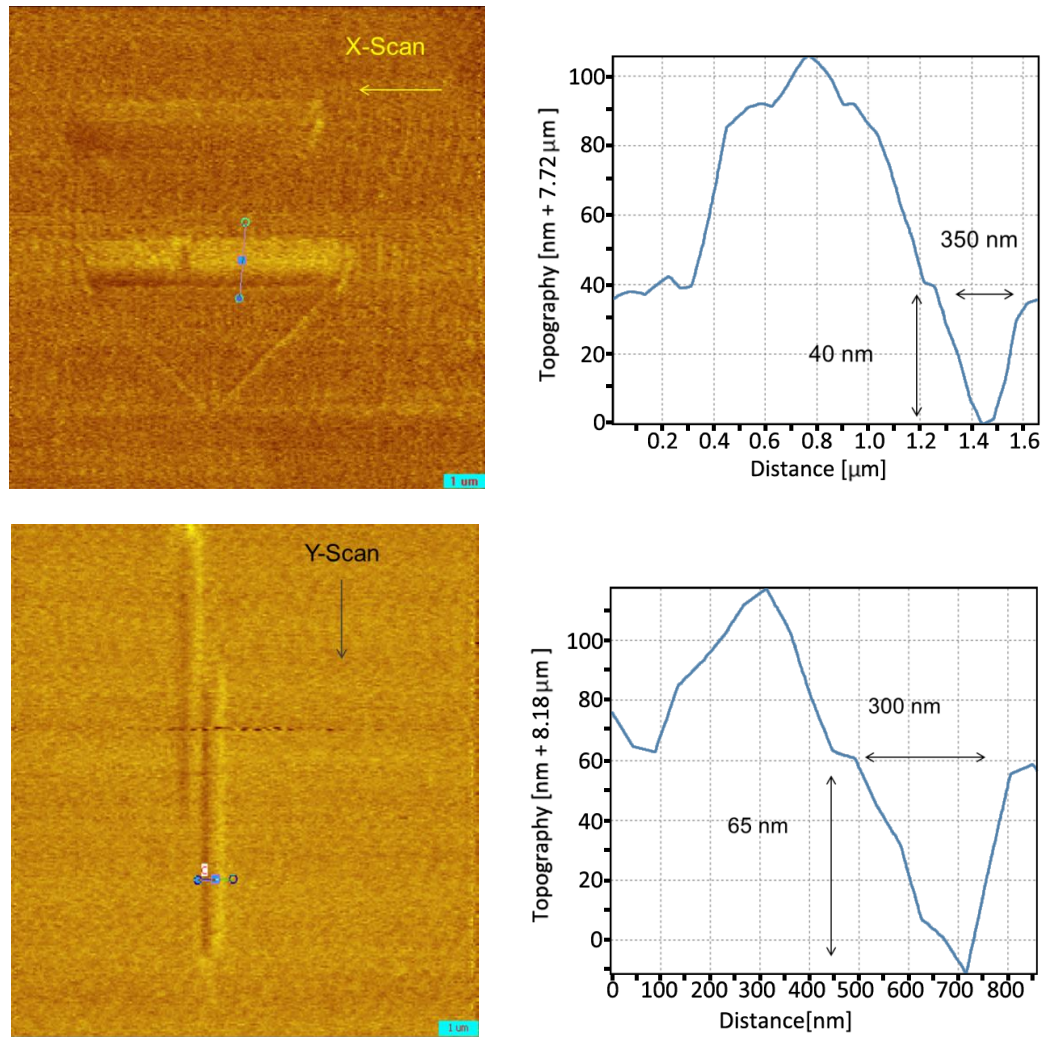
Figure 5.20 – *The outcome of the mechanical lithography in which x (top) and y (bottom) line scans were carried out repeatedly over a period of time (30-60 minutes).*
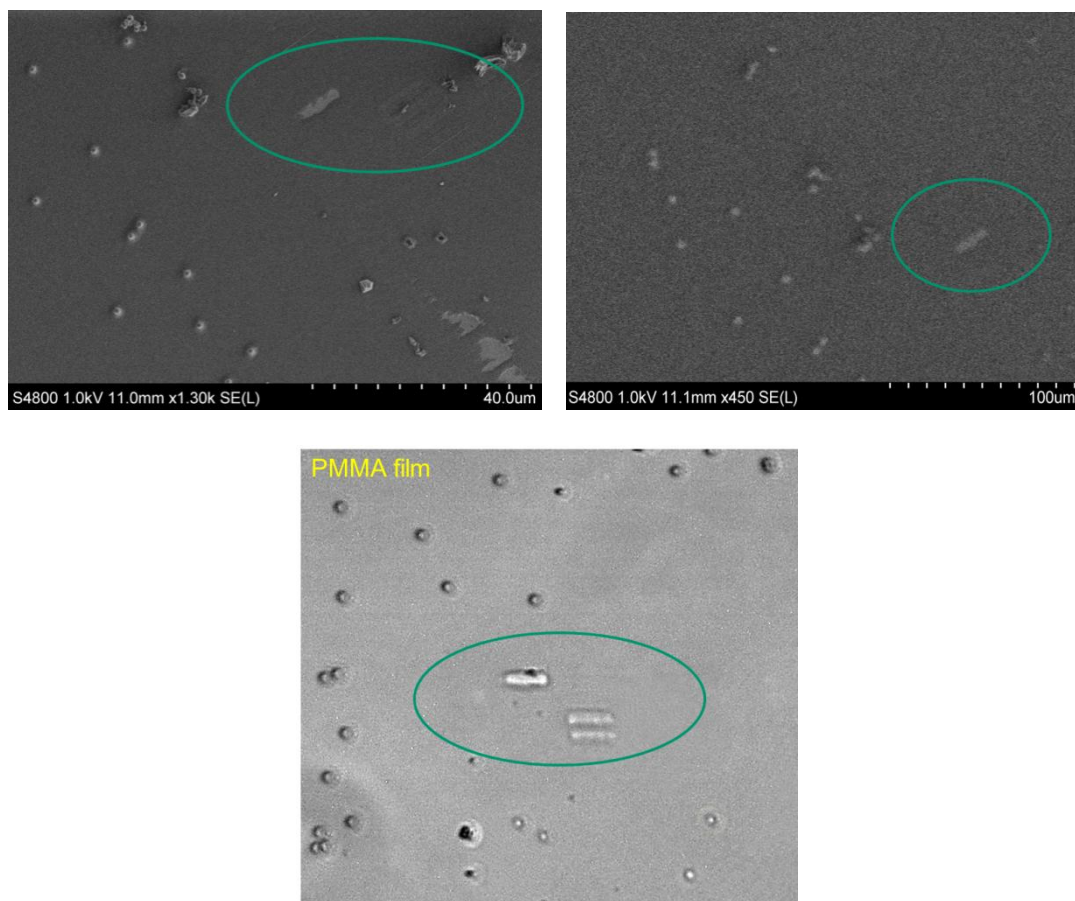
Figure 5.21 - *(Top) SEM images verify the mechanically engraved grooves on a PMMA coated cover slip. (Bottom) Wide-field optical image also confirms the mechanically engraved grooves.*

Chapter 6

Conclusions

- ➢ Near-field scanning optical microscope (NSOM) is a microscopy technique for nanostructure investigation. The principles of NSOM are very much in play within the research community. It has many different applications ranging from biological studies to nanofabrication and single molecule trapping and manipulation.

- ➢ The design and fabrication of a home-built NSOM module for conventional inverted microscopes has been described.

- ➢ We have assembled a NSOM module atop an inverted fluorescence microscope and used it as a near-field instrument for nanostructure investigation of various samples including gratings, calibration grids, nanospheres and gold nanoparticles

- ➢ We demonstrated the ability to achieve nanometer-scale surface modification of specific polymer films using this technique.

References

1. Abbe E. Beiträge zur Theorie des Mikroskops und der mikroskopischen Wahrnehmung. *Arch. für Mikroskopische Anat.* 1873;9(1):413-418. doi:10.1007/BF02956173.

2. Synge EH. A suggested method for extending microscopic resolution into the ultra-microscopic region. *Philos. Mag. Ser. 7* 1928;6(35):356-362. doi:10.1080/14786440808564615.

3. Dunn RC. Near-Field Scanning Optical Microscopy. *Chem. Rev.* 1999;99(10):2891-2928. doi:10.1021/cr980130e.

4. Synge EH. An Application of Piezo-electricity to Microscopy. *Phil. Mag* 1932;13:297.

5. McMullan D. The prehistory of scanned image microscopy Part 1: scanned optical microscopes. *Proc Roy Microsc Soc* 1990;25:127-131.

6. O'Keefe JA. Resolving power of visible light. *J. Opt. Soc. Am.* 1956;46:359.

7. Baez A V. Is resolving power independent of wavelength possible? An experiment with a sonic 'macroscope'. *J. Opt. Soc. Am.* 1956;46:901.

8. Ash EA, Nichols G. Super-resolution aperture scanning microscope. *Nature* 1972;237:510.

9. Pohl DW, Denk W, Lanz M. Optical stethoscopy: Image recording with resolution λ/20. *Appl. Phys. Lett.* 1984;44(7):651. doi:10.1063/1.94865.

10. Betzig E, Lewis A, Harootunian A, Isaacson M, Kratschmer E. Near Field Scanning Optical Microscopy (NSOM). *Biophys J.* 1986;49(1):269-279.

11. Harootunian A, Betzig E, Isaacson M, Lewis A. Super-resolution fluorecence near-field scanning optical microscopy. *Appl. Phys. Lett.* 1986;49:674-676.

12. Betzig E, Harootunian A, Lewis A, Isaacson M. Near-field diffraction by a slit: implications for superresolution microscopy. *Appl. Opt.* 1986;25(12):1890. doi:10.1364/AO.25.001890.

13. Yao N, Wang ZL, eds. *Handbook of Microscopy for Nanotechnology*. Boston: Kluwer Academic Publishers; 2005:29. doi:10.1007/1-4020-8006-9.

14. Betzig E, Trautman JK, Harris TD, Weiner JS, Kostelak RL. Breaking the diffraction barrier: optical microscopy on a nanometric scale. *Science* 1991;251(5000):1468-70. doi:10.1126/science.251.5000.1468.

15. Valaskovic GA, Holton M, Morrison GH. Parameter control, characterization, and optimization in the fabrication of optical fiber near-field probes. *Appl. Opt.* 1995;34(7):1215-28. doi:10.1364/AO.34.001215.

16. Turner DR. Etch Procedure for Optical Fibers. U.S. Patent 4469554. 1984.

17. Stöckle R, Fokas C, Deckert V, et al. High-quality near-field optical probes by tube etching. *Appl. Phys. Lett.* 1999;75(2):160. doi:10.1063/1.124305.

18. Carlson C. Development of the electrostatic corral for the trapping of single molecules in solution. Dissertation. 2010.

19. Hecht B, Sick B, Wild UP, et al. Scanning near-field optical microscopy with aperture probes: Fundamentals and applications. *J. Chem. Phys.* 2000;112(18):7761. doi:10.1063/1.481382.

20. Veerman JA, Otter AM, Kuipers L, van Hulst NF. High definition aperture probes for near-field optical microscopy fabricated by focused ion beam milling. *Appl. Phys. Lett.* 1998;72(24):3115. doi:10.1063/1.121564.

21. Shi J, Qin XR. Formation of glass fiber tips for scanning near-field optical microscopy by sealed- and open-tube etching. *Rev. Sci. Instrum.* 2005;76(1):013702. doi:10.1063/1.1823778.

22. Novotny L. *"The History of Near-Field Optics" Progress in Optics 50, E. Wolf (ed.), Chapter 5, p.137- 184 (Elsevier, Amsterdam, The Netherlands, 2007).*

23. Kühn S, Håkanson U, Rogobete L, Sandoghdar V. Enhancement of Single-Molecule Fluorescence Using a Gold Nanoparticle as an Optical Nanoantenna. *Phys. Rev. Lett.* 2006;97(1):017402. doi:10.1103/PhysRevLett.97.017402.

24. Paesler M, Moyer P, Jahncke C, et al. Analytical photon scanning tunneling microscopy. *Phys. Rev. B. Condens. Matter* 1990;42(10):6750-6753. Available at: http://www.ncbi.nlm.nih.gov/pubmed/9994776. Accessed September 13, 2014.

25. Meixner AJ, Bopp MA, Tarrach G. Direct measurement of standing evanescent waves with a photon-scanning tunneling microscope. *Appl. Opt.* 1994;33(34):7995-8000. doi:10.1364/AO.33.007995.

26. Moyer PJ, Jahncke CL, Paesler MA, Reddick RC, Warmack RJ. Spectroscopy in the evanescent field with an analytical photon scanning tunneling microscope. *Phys. Lett. A* 1990;145(6-7):343-347. doi:10.1016/0375-9601(90)90946-L.

27. Reddick RC, Warmack RJ, Chilcott DW, Sharp SL, Ferrell TL. Photon scanning tunneling microscopy. *Rev. Sci. Instrum.* 1990;61(12):3669. doi:10.1063/1.1141534.

28. Guerra JM. Photon tunneling microscopy. *Appl. Opt.* 1990;29(26):3741-52. doi:10.1364/AO.29.003741.

29. Binnig G, Rohrer H, Gerber C, Weibel E. Surface Studies by Scanning Tunneling Microscopy. *Phys. Rev. Lett.* 1982;49(1):57-61. doi:10.1103/PhysRevLett.49.57.

30. Binnig G, Quate CF. Atomic Force Microscope. *Phys. Rev. Lett.* 1986;56(9):930-933. doi:10.1103/PhysRevLett.56.930.

31. Betzig E, Finn PL, Weiner JS. Combined shear force and near-field scanning optical microscopy. *Appl. Phys. Lett.* 1992;60(20):2484. doi:10.1063/1.106940.

32. Toledo-Crow R, Yang PC, Chen Y, Vaez-Iravani M. Near-field differential scanning optical microscope with atomic force regulation. *Appl. Phys. Lett.* 1992;60(24):2957. doi:10.1063/1.106801.

33. Karrai K, Grober RD. Piezoelectric tip-sample distance control for near field optical microscopes. *Appl. Phys. Lett.* 1995;66(14):1842. doi:10.1063/1.113340.

34. Cady WG. The piezoelectric resonator. *Phys. Rev. Lett. A.* 1921;17:531-533.

35. Kahan A. Cut Angles for Quartz Crystal Resonators, U. S. Patent 4499395. 1985.

36. Newport. Available at: http://search.newport.com/?x2=sku&q2=9062-XYZ.

37. Nasse MJ. Development of a Confocal and Near-field Scanning Optical Microscope for Polarization-resolved Temporal Studies of Single Nano-objects. Dissertation. 2004.

38. Nanoscience. Available at: http://store.nanoscience.com/store/pc/viewPrd.asp?idproduct=2049.

39.   Agar Scientific. Available at: http://www.agarscientific.com/grating-type-tgx.html.

40.   Agar Scientific. Available at: http://www.agarscientific.com/grating-type-tgz.html.

41.   Tedpella. Available at: http://www.tedpella.com/gold_html/nanoxact-gold.htm.

CURRICULUM VITAE

Taher Ababneh

Education
Doctor of Philosophy, Physical Chemistry, University of Wisconsin-Milwaukee (UWM), Milwaukee, WI 2006-2014
- Dissertation: "Design and Implementation of a Near-field Scanning Optical Module for Inverted Microscopes".
- George Keulks Award for Graduate Research April 2013.
- McFarland Award for the Best Graduate Research Poster Presentations May 2011.
- Chancellor's Graduate Student Award 2006-2011.

Master of Science, Chemistry, Yarmouk University, Irbid, Jordan 2001-2004
- Thesis: "Temporal Distribution of Heavy Metals in the Mussel Modiolus Auriculatus at an Industrial Site on the Jordanian Coast of the Gulf of Aqaba; Indicator of the Seawater Environmental Quality"
- Research assistantship awarded from the Marine Science Station, The University of Jordan.
- Academic honors/distinctions: Ranked 1st among graduating class with accumulative average of 88.7%.

Bachelor of Science, Chemistry, Yarmouk University, Irbid, Jordan 1997-2001
- Academic honors/ distinctions: Placed on Dean's Honor List twice during academic years of 1997/1998 and 1998/1999. Ranked 1st among graduating class of fifty seven (57) students with accumulative average of 83.4%

Teaching Experience

- General chemistry, Department of Chemistry, University of Wisconsin-Milwaukee, Milwaukee, WI 2006-2014
- General chemistry, Department of Chemistry, Memorial University of Newfoundland, St. John's, NL Canada 2005
- Physical Chemistry Lab and General chemistry, Department of Chemistry, Yarmouk University, Irbid, Jordan 2001-2002

Scientific Meetings:

- Chemistry and Biochemistry Research Symposium, April 20,2013. UWM "Nano-scale Topographical Imaging with NSOM".
- The 40th Great Lakes Regional meeting (GLRM) June 5 – 8, 2013. La Crosse, WI. "Design and Implementation of a Near-field Scanning Optical Microscope".
- SciX, Kansas City, MO. September 30 – October 5 2012. "A Near-field Scanning Optical Module for Inverted Microscopes"
- UWM Awards Day –May 10th. 2011. "Design and Optimization of Near-field Scanning Optical Microscope"
- Milwaukee ACS Younger Chemists Committee Poster Mixer October 22, 2010. "Construction of a Near-field Optical Module for a Confocal Microscope"

- 2010 Physical Electronics Conference June 15, UWM.
- UWM Awards Day –May 7th. 2010. "Optical Imaging Beyond The Diffraction Limit"
- Laboratory for Surface Studies Student Summer Symposium August 21, 2009. T. S. Ababneh and J. C. Woehl, " Viewing the World through Nanometer Eyes: Near-field Optical Microscope for Ultra-high Resolution Imaging". Poster presented at the 2009, University of Wisconsin-Milwaukee, Milwaukee, WI, 2009
- The 38th Great Lakes Regional meeting (GLRM) May 13 - 16, 2009 at the Lincolnshire Marriott in Lincolnshire, IL. "Development of a near-Field Optical Microscope for Fluorescence Imaging at Ultra High Optical Resolution"
- UWM Awards Day – 2009. "Development of a Near-Field Optical Microscope for Fluorescence Imaging at Ultra High Optical Resolution".
- Laboratory for Surface Studies Student Summer Symposium T. S. Ababneh and J. C. Woehl, "Toward fluorescence imaging at ultra-high optical resolution". Poster presented at the 2007, University of Wisconsin-Milwaukee, Milwaukee, WI, 2007
- UWM Awards Day – 2007. "Fluorescence Imaging at Ultrahigh Optical Resolution: Instrument Design"
- UWM Awards Day– 2006. "Right-Angle Turns in Optical Setups Using Mirrors and Prisms". Taher S. Ababneh, Michael J. Nasse, and Jörg C. Woehl
- 37th Great Lake Regional Meering of the ACS, May 31-June 2, 2006 MKE WI
- 2005: Summer Organic Chemistry Conference on Everybody's Research Aug 11-12 St John's NL "Stereoselective Approaches to Functionalized Pyrrolidines"
- 11[th]International Symposium on Novel Aromatic Compounds (ISNAA) Aug 14-18 2005. NL Canada.

Acquired Skills:
- Flame Atomic Absorption Spectroscopy
- Absorption Spectroscopy
- Fluorescence Spectroscopy
- Scanning Electron Microscopy (SEM)
- Single Molecule Laser Spectroscopy
- Near-field Scanning Optical Microscopy (NSOM)
- Shear-force Microscopy (SFM)
- Focused Ion Beam (FIB)
- Fabrication of Optical Fiber Tips by Chemical Etching
- Submicron Mechanical Lithography of Polymer Substrates
- Sample Preparation with Spin Coating Technique
- **Software**: Solidwroks, National Instruments Labview, Mathworks Matlab, 3ds Max Autodesk.